HIghly advanced Probabilistic design and Enhanced Reliability methods for high-value, cost-efficient offshore WIND

Title: Aero-servo-hydroelastic model uncertainty
Deliverable no: D3.3

Delivery date: 31.03.2022
Lead beneficiary: EDF
Dissemination level: Public

Author(s) information (alphabetical):		
Name	**Organisation**	**Email**
C. Peyrard	EDF	christophe.peyrard@edf.fr
F. Robaux	EDF	fabien.robaux@enpc.fr
A. Borras-Nadal	IFPEN	adria.borras-nadal@ifpen.fr
P-A. Joulin	IFPEN	pierre-antoine.joulin@ifpen.fr
L. Mayol	IFPEN	maria-laura.mayol@ifpen.fr
S. Eldevik	DNV	simen.eldevik@dnv.com
M. Guiton	IFPEN	martin.guiton@ifpen.fr
A. Cousin	IFPEN	alexis.cousin@ifpen.fr
M. Benoit	EDF	michel.benoit@edf.fr
N. Dimitrov	DTU	nkdi@dtu.dk
A. Lovera	EDF	anais.lovera@edf.fr
C .Fereira	DNV	carla.ferreira@dnv.com

Document information:					
Version	**Date**	**Description**	**Prepared by**	**Reviewed by**	**Approved by**
0	31-03-2022	First official version	Authors listed above	F. Blondel, W.Benguigui, P.Bousseau	Nikolay Dimitrov

Definitions:	

Contents

List of Abbreviations

OWT	Offshore Wind Turbine
BEM	Blade Element Momentum
ASHE	Aero-Servo-Hydro-Elastic
DLW	DeepLines Wind™
DOE	Design of Experiments
MCF	MacCamy & Fuchs correction
LTF	Linear Transfer Function
QTF	Quadratic Transfer Function
DEL	Damage Equivalent Load
BoEM	Boundary Element Method
NWT	Numerical Wave Tank
VoF	Volume of Fluid
TP	Transition Piece
HAWT	Horizontal Axis Wind Turbine
AEP	Annual Energy Production
LCOE	Levelized Cost of Energy
CPU	Central Processing Unit
DLW	Deeplines Wind^{TM}
ETM	Extreme Turbulence Model
ESS	Extreme Sea State
MCF	Mac Camy & Fuchs
GP	Gaussian Process
FVW	Free Vortex Wake
GPU	Graphics Processing Unit
CUDA	Compute Unified Device Architecture
LHS	Latin Hypercube Sampling
DEL	Damage Equivalent Load
WP	Work Package
SCADA	Supervisory Control And Data Acquisition
CV	Cross-Validation
RMSE	Root-mean-squared-error
CI	Confidence Interval
ANEMOC	Atlas Numérique d'Etats de Mer Océaniques et Côtiers - Digital Atlas of Ocean and Coastal Sea States

1. Executive Summary

This report presents the work related to Deliverable 3.3. It is dedicated to the estimation of Aero-Servo-Hydro-Elastic (ASHE) model uncertainty for what concerns the hydrodynamic loading (section 4) and the aerodynamic loading (section 5). Indeed, the models which are commonly used to predict the loads on the main components of an Offshore Wind Turbine (OWT), given some conditions of wind and waves, simplify the physics to keep the computation time affordable. Note that the influence of submarine current is not considered in this report for the sake of simplification. These "engineering" models are thus introducing

epistemic (i.e. which could be reduced by increasing knowledge) model uncertainties on their resulting outputs which are estimated here through comparisons with the results of higher fidelity models.

The results are documented for the two offshore case studies of HIPERWIND: the 2.3 MW turbine on a monopile within the Teesside (United Kingdom) wind farm, and the IEA15MW wind turbine on UMaine semi-submersible floater in South Brittany site (France). The latest is a modified version of the original design which was proposed by NREL and UMaine [1.][2.]. The changes are mainly on the tower to avoid a risk of resonance with natural frequencies too close to the 3P frequency [3.]. In this report, we also present an additional modification with clump weights on the mooring lines to adapt their dynamics to the extreme 50-year returning period waves of South Brittany.

Summary of hydrodynamic loading uncertainty:

The hydrodynamic loadings have been investigated on both floating and bottom fixed foundations:

- On the bottom fixed side, the focus was made on the damage induced by the hydrodynamic loads on two monopiles at the Teesside location: the original 2.3MW monopile and a larger one, designed within HIPERWIND based on the DTU 10MW reference turbine. A comparison has been made between a base case engineering hydrodynamic method (based on the EDF R&D DIEGO solver and the MacCamy & Fuchs correction) and more reliable hydrodynamic load estimation methods, based on Potential Flow solvers. An extensive set of sea conditions have been used to perform the comparisons, covering the full Teesside *Hs-Tp* scatter diagram. The conclusions suggested that variations of +/- 10% of the hydrodynamic Damage Equivalent Load (DEL) can be obtained due to simplification made by the application of the MacCamy-Fuchs correction. In addition, a tendency of the engineering model to overestimate by 5 to 10% the DEL due to the high-frequency loads has been found, in a large range of wave periods. For high and long waves however, the engineering model underestimates quite significantly the DEL (-10% to -50%). We have also noted that these levels of discrepancies between engineering models and more accurate method is in the same order as the uncertainty obtained when using different stretching models. Recommendations on the hydrodynamic DEL uncertainty level have been made.
- On the floating side, the focus was made on the level of damping applied on the floating foundations and in particular on the drag loads. The University of Maine 15MW floater has been used and several uncertainty sources have been investigated using CFD:
    - solver: OpenFoam and neptune_cfd have been used by IFPEN and EDF R&D respectively,solver: OpenFOAM® and neptune_cfd have been used by IFPEN and EDF R&D respectively,
    - kinematic conditions: fixed body in waves and motion of the body in still water,
    - extraction of the drag coefficients: 2 methods have been applied, the first one based on least square and the order one on harmonics identification.

    Five zones on the floater have been selected for drag coefficient estimation: the side column, the central column, the pontoons, and the base of the columns. For each zone, the drag coefficients are obtained for a large range of Keulegan-Carpenter numbers, allowing to characterize the damping for a large range of conditions. Recommendations are made for the drag coefficient choice and their expected variations.

Summary of aerodynamic loading uncertainty:

An exhaustive comparison between the usual Blade Element Momentum (BEM) approach and a more accurate Vortex-based model has been conducted for both the Teesside fixed, and the South Brittany floating OWT. The BEM approach is provided for 3 different software: Deeplines Wind^{TM} (DLW, IFPEN), Diego (EDF) and HAWC2 (DTU). The input space is 3D for the fixed case with mean speed, turbulence intensity and yaw misalignment. For the floating case, the input space is 6D. It is composed of 3 parameters for wind: wind speed, the absolute wind direction and turbulence intensity; and 3 parameters for waves: wave height, wave period and wave direction (6D). The outputs concern the production, Damage Equivalent Loads (DEL) at the blade root, forces along the blades and forces integrated over the rotor. From an initial space-filling Design of Experiments (DoE), an iterative procedure has been chosen to define the points at which costly Vortex simulations are done, in order to reduce the uncertainty on the difference between BEM and Vortex for both production and design outputs. It is exploiting the characteristics of Gaussian Processes computed for each output. The first contribution to the model uncertainty is estimated from the differences between the 3 BEM models. Then it is found that outside of a domain of both high turbulence and high wind speed, which is rarely encountered, the differences between BEM and Vortex remain small, particularly for the fixed OWT. Another contribution to the model uncertainty is that the BEM vs Vortex differences are higher for the floating wind turbine. Even though, the 6D input space for the South Brittany case is sparsely explored due to the high computational cost, differences between the two approaches can be noticed, specifically for the large floating OWT case. A major part of these differences may however be due to the use of controller setting chosen for BEM, which is thus non optimal for the Vortex model. Due to this controller influence, the estimated model uncertainty is an upper bound of the true uncertainty, which is more sensitive to the wind parameters than to the wave parameters.

Research Significance:

The results presented in this report provide a comprehensive estimate of the ASHE model uncertainty for both the aerodynamic loads and the hydrodynamic fluid-structure interaction. They are provided for both a fixed and a floating case, and by considering their distribution in the input parameters representing the environmental conditions. This information is useful for the designer to interpret the results of the ASHE simulations keeping in mind the usual "engineering" model limits. From a more quantitative point of view, the uncertainty can also be used to replace pure a priori distributions in uncertainty reduction study, for example to compute reliable design, with the limit of the extrapolation to other case studies. This will be for instance the case in the next work of HIPERWIND which will test and develop different approaches for both Ultimate and Fatigue Limit State Analysis.

References of the Executive Summary

[1.] Allen, C., Viscelli, A., Dagher, H., Goupee, A., Gaertner, E., Abbas, N., ... & Barter, G. (2020). *Definition of the UMaine VolturnUS-S reference platform developed for the IEA Wind 15-megawatt offshore reference wind turbine* (No. NREL/TP-5000-76773). National Renewable Energy Lab. (NREL), Golden, CO (United States).

[2.] Evan Gaertner, Rinker, J., Sethuraman, L., Zahle, F., Anderson, B., Barter, G., Abbas, N., Meng, F., Bortolloti, P., Skrzypinski, W., Scott, G., Feil, R., Bredmose, H., Dykes, K., Sheilds, M., Allen, & C., Viselli, A. (2020). *Definition of the IEA wind 15-megawatt offshore reference wind turbine Tech. Rep.* NREL/TP-5000-75698 National Renewable Energy Laboratory Golden, CO.

[3.] Capaldo, M., Guiton, M., Huwart, G., Julan, E., Kramisirov Dimitrov, N., Kim, T., Lovera, A., & Peyrard, C. (2021). *Design brief of HIPERWIND offshore wind turbine cases: bottom fixed 10MW and floating 15MW*. https://www.hiperwind.eu/publications.

2. Introduction

The main objective of the HIPERWIND project is to reduce the Levelized Cost Of Energy (LCOE) by reducing the uncertainty in the complete chain of modeling OWTs in a wind farm. The modeling aims at predicting the electricity production and the loading on OWTs components. A first distinction should be done between aleatoric intrinsic uncertainty of wind, waves, and current loading and the epistemic model uncertainties due to lack of knowledge. If consequent research literature improves OWTs design by including uncertainty in a reliability computation of several limit states (see [7.] for a general framework and [1.] for a detailed review), it usually considers only input parameters uncertainty of a given model and not the global (ASHE) model uncertainty (see e.g. [10.][4.]). Some papers are however documenting ASHE model uncertainty, which combines the controller behavior, aerodynamic model, hydrodynamic model including input drag damping, structural model, and load post-treatment like RainFlow counting and S-N law for fatigue (see[1.][8.][11.]). They however only use a coefficient of variation (i.e. standard variation over mean) for standard distribution like normal or log-normal to quantify the model uncertainty, or deal with only one part of the ASHE model like the foundation [20.] or the turbine [19.]. Anyway, with the development of new increased size OWT interacting with the atmospheric boundary layer, there is a need to provide more details on the ASHE model uncertainty for keeping an accurate reliable design [1.].

This deliverable report deals with the ASHE model uncertainty of complex simulators which are used for designing OWT according to standards rules (e.g.[13.][14.]). For illustration purposes and far from being complete, one can think about the HAWC2, DeepLines Wind^{TM,} and Diego codes which are used by HIPERWIND partners (see [16.] for details) but also the open-source OpenFast code of NREL (see Table 1 of [6.] for a more complete list). While some of these codes may be considered of the research domain, we will qualify them as "engineering" codes to underline their differences with high fidelity software implying a much larger computational cost.

Several ASHE "engineering" simulators have been developed for the design of OWT, with common physical hypothesis for wind and wave loading. A description of the state-of-the-art numerical methods and their limitations can be found in [3.]. The aerodynamic is generally represented by the Blade Element Momentum (BEM) approach which assumes, among other hypotheses, stationary flow conditions, combining the momentum theory and the blade element theory. Hydrodynamic strategies depend on whether the OWT foundation is fixed or floating. For the case of floating foundations, hydrodynamic loading are generally represented by a combination of potential flow theory for large bodies (e.g. a semi-submersible floater) and Morison theory for small bodies (e.g. braces or pontoons). For the case of monopile fixed foundations, wave loadings are generally represented using the strip theory, with the well known Morison equation or the MacCamy & Fuchs (MCF) correction to better estimate the diffraction effect.

These methods of "engineering" ASHE have been validated against experimental data in wind tunnels for aerodynamics and basins for hydrodynamics. BEM can provide a good representation if accurate sectional airfoil lift and drag coefficients are available [18.]. It however requires empirical corrections for non-stationary effects like dynamic inflow and other complex phenomena such as tip-losses and hub-losses [19.]. On the hydrodynamic side, linear theories are generally used due to their straightforward

implementation. As a trade-off between accuracy and simplicity, some nonlinearities like high order Fourier series for the wave elevations or second-order wave loads for the floating system have been integrated, to overcome some lacks due to the linear hypothesis like slow-drift or asymmetric wave shape during extreme events. The potential flow being the governing hypothesis of any wave-body engineering model, drag loads are added using Morison-like methods and empirical drag coefficients, or with a damping matrix on the six degrees of freedom of a rigid floater, or by using additional elements on the thin components of the immersed structure. As an example, in [16.], a HAWC2 floating model uses a damping matrix while Deeplines Wind^{TM} and Diego floating models use Morison elements. Used mostly for monopiles, the MCF correction assumes a constant radius which does not account for the change between the monopile and the transition piece. It is also based on both linear waves and linear diffraction theories. The choice of these methods as a consensus for designing OWT was the result of a compromise between accuracy and affordable computational times in the context of industrial projects.

From the complexity of these Multiphysics "engineering" simulators, a way to complete their validation is also to compare them through benchmark exercises. This has been the topic of IEA Offshore Code Comparison projects of IEA Wind task 23 and Offshore Code Comparison Collaboration Continuation of IEA Wind task 30[5.][6.]. Despite the benchmark specification and iterations in code-to-code comparisons, noticeable differences are obtained in the output load time series under turbulent wind and irregular waves that may be related to the considerable possible options in the numerical setting. These options include the coupling strategy between aerodynamics, hydrodynamics, elasticity, and also with the controller generally provided as a library. One can also consider differences in the spatial discretization either with a complete meshing or with a reduction strategy with blade and tower modes as degrees of freedom (e.g. NREL FAST based on ElastoDyn). Another source of differences between the codes can also come from the time integration scheme and numerical damping, and complex loading like the dynamic contact at the touch-down point of catenary mooring lines.

The differences between "engineering codes" identified in a benchmark, to which may be added some differences of interpretation on the loading in the context of industrial projects provide the first source of model uncertainty which should be considered in a reliability design obtained generally with one ASHE simulator. The second source of uncertainty comes from the BEM, MCF, and Potential/Morison approximations. This report investigates both uncertainties for what concerns the aerodynamics and hydrodynamics loading with the following strategy: simulations were conducted on the Teesside monopile case study and the IEA15MW mounted on the UMaine semi-submersible which was modified for the South Brittany site (see [16.] and [17.]). The second source of uncertainty which is related to "engineering" model approximation is investigated by comparing it to higher fidelity simulations. The aerodynamics and hydrodynamics loading were studied in two different tasks, using high fidelity models on the wind or wave loading only, the other part being represented by the "engineering" approaches. This choice presents the advantage to enable a better understanding of different sources when interpreting the results. However, its main drawback is that we do not compare engineering model simulations with high fidelity simulations taking into account the aerodynamics and hydrodynamics coupling. Despite recent attempts that have been proposed in the literature (e.g.[9.][2.]), their validation is not judged enough established yet for corresponding to the TRL target of HIPERWIND.

The structure of the report is as follows.

Section 3 briefly presents the modification of the floating case study for the IEA15MW OWT on UMaine semi-submersible. To ensure the design is admissible for the extreme waves of the South Brittany site, 60t masses representing clump weights are added to each mooring line.

Section 4 is devoted to the hydrodynamic loading uncertainty. It begins with a fixed OWT case, focusing on MCF correction error for varying monopile radius. The influence of non-linear wave loading is not included in this report as HIPERWIND WP2 will provide the High-Order Spectral wave models only later. Note that the measured uncertainty for this fixed case is on the ASHE output for fatigue.

The second part of section 4 is devoted to the floating OWT case, focusing on the drag coefficient uncertainty for the semi-submersible floater. Note that the corresponding measured uncertainty is this time on input data of the ASHE simulation which is fitted using two different high fidelity CFD models.

Then section 5 is devoted to the aerodynamic loading uncertainty, focusing on BEM compared to higher fidelity vortex-based simulations. Note that the measured uncertainty is on the ASHE output. The vortex model, CASTOR, used is a free-wake vortex filament solver, based on the generalized Prandtl lifting-line theory.

Last section concludes with a synthesis of the he key results of this report and open perspectives for future improvement in other projects. It also underlines how the results will be used in the next stages of HIPERWIND.

The last section summarizes the key results of this report and open perspectives for future improvement in other projects.

For being used in WP4 reliable design computations on OWT main components (blade, tower and monopile or mooring lines for foundations), the uncertainty results need to be estimated for the input environmental parameters. In OWT design, based on time scale separation in the wind speed and wave elevation spectra one can distinguish short-term stationary processes (the usual convention for the short-term duration in standards is set to 10min for wind and 3 to 6h for waves) and long term pluriannual service life. Note that the simulation guidelines of IEC standard [12.] recommend generating the short-term loading time series either with successive stochastic 10min time series or with one longer time series.

The short-term processes can be represented by long-term varying parameters which in this report may be composed of the time-averaged wind speed at hub height, the standard deviation of the wind speed, the wave significant height and peak period plus the wind and wave mean directions. Let us denote X_{env} the vector of uncertain long term parameters, X_{drag} the vector of uncertainty on drag coefficient for the semi-submersible floater, ε_{MCF} the vector of uncertainty on hydrodynamic forces for monopile and ε_{aero} the vector of uncertainty on aerodynamic forces. Note that X_{env} dependencies of model uncertainties are obtained as Gaussian processes which can be written as

$$\varepsilon|\,X_{env} \sim \sigma(X_{env})\mathcal{N}(0,1) + \mu(X_{env}).$$

From a time series $y_{simu}(x_{env}, x_{drag})$ the output of the ASHE simulator, one can write a modified function to account for the uncertainties as :

$$\text{y}(x) = f_{error}(y_{simu}(x_{env}, x_{drag}), \varepsilon_{monopile}, \varepsilon_{aero}).$$

References of the Introduction

[1.] Jiang, Z., Hu, W., Dong, W., Gao, Z., & Ren, Z. (2017). Structural reliability analysis of wind turbines: A review. *Energies*, *10*(12), 2099

[2.] Liu, Y., Xiao, Q., Incecik, A., & Peyrard, C. (2019). Aeroelastic analysis of a floating offshore wind turbine in platform-induced surge motion using a fully coupled CFD-MBD method. *Wind Energy*, *22*(1), 1-20.

[3.] Matha, D., Schlipf, M., Pereira, R., & Jonkman, J. (2011). Challenges in simulation of aerodynamics, hydrodynamics, and mooring-line dynamics of floating offshore wind turbines. In *The Twenty-first International Offshore and Polar Engineering Conference*. OnePetro.

[4.] Nispel, A., Ekwaro-Osire, S., Dias, J. P., & Cunha, A. (2021). Uncertainty quantification for fatigue life of offshore wind turbine structure. *ASCE-ASME J Risk and Uncert in Engrg Sys Part B Mech Engrg*, *7*(4).

[5.] Passon, P., Kühn, M., Butterfield, S., Jonkman, J., Camp, T., & Larsen, T. J. (2007). OC3— Benchmark exercise of aero-elastic offshore wind turbine codes. In *Journal of Physics: Conference Series* (Vol. 75, No. 1, p. 012071). IOP Publishing.

[6.] Robertson, A., Jonkman, J., Vorpahl, F., Popko, W., Qvist, J., Frøyd, L., ... & Guérinel, M. (2014). Offshore code comparison collaboration continuation within IEA wind task 30: Phase II results regarding a floating semisubmersible wind system. In *International Conference on Offshore Mechanics and Arctic Engineering* (Vol. 45547, p. V09BT09A012). American Society of Mechanical Engineers.

[7.] Sørensen, J. D. (2015). Reliability assessment of wind turbines. In *Proceedings of the 12th International Conference on Applications of Statistics and Probability in Civil Engineering (ICASP12), Vancouver, Canada, July 12-15*. University of British Columbia.

[8.] Tarp-Johansen, N. (2003). Examples of Fatigue Lifetime and Reliability Evaluation of Larger Wind Turbine Components, Risø-R-1418.

[9.] Tran, T. T., & Kim, D. H. (2016). Fully coupled aero-hydrodynamic analysis of a semi-submersible FOWT using a dynamic fluid body interaction approach. *Renewable energy*, *92*, 244-261.

[10.] Velarde, J., Vanem, E., Kramhøft, C., & Sørensen, J. D. (2019). Probabilistic analysis of offshore wind turbines under extreme resonant response: Application of environmental contour method. *Applied Ocean Research*, *93*, 101947.

[11.] Veldkamp, D. (2006). Chances in wind energy–a probabilistic approach to wind turbine fatigue design [Ph. D thesis]. *Delft University of Technology*.

[12.] International Electrotechnical Commission. (2019). IEC 61400-1: 2019: Wind energy generation systems-Part 1: Design requirements.

[13.] International Electrotechnical Commission. (2019). IEC 61400-3-1: 2019 Wind energy generation systems–Part 3-1: Design requirements for fixed offshore wind turbines.

[14.] Det Norske Veritas AS. (2018). *Design of Floating Wind Turbine Structures*. DNV-OS-J103, July 2018.

[15.] Kim, T., Natarajan, A., Lovera, A., Julan, E., Peyrard, C., Capaldo, M, Huwart, G., Bozonnet, P., & Guiton, M. (2022). A comprehensive code-to-code comparison study with the modified IEA15MW-UMaine Floating Wind Turbine for H2020 HIPERWIND project, submitted to Torque 2022 conference.

[16.] Capaldo M., Guiton, M., Huwart, G., Julan, E., Kramisirov Dimitrov, N., Kim, T., Lovera, A., & Peyrard, C. (2021). *Design brief of HIPERWIND offshore wind turbine cases: bottom fixed 10MW and floating 15MW*. https://www.hiperwind.eu/publications, June 2021.

[17.] Glauert, H. (1935). Airplane propellers. In *Aerodynamic theory* (pp. 169-360). Springer, Berlin, Heidelberg.

[18.] Burton, T., Jenkins, N., Sharpe, D., & Bossanyi, E. (2011). *Wind energy handbook*. John Wiley & Sons.

[19.] Robertson A.N., Shaler K.Sethuraman L. and Jonkman J. (2019). *Sensitivity analysis of the effect of wind characteristics and turbine properties on wind turbine loads*. Wind Energy Science 4, 479-513.

[20.] Robertson A. (2017). *Uncertainty Analysis of OC5-DeepCwind Floating Semisubmersible Offshore Wind Test Campaign*. NREL report CP-5000-68035.

3. New design for the IEA15 MW OWT on UMaine semi-submersible floater in South Brittany

Figure 1 shows the distribution of the two JONSWAP spectrum parameters wave height H_s and peak period T_p which are provided by numerical simulations covering the period from 1979 to 2010 of ANEMOC data [1.]. Each point represents a 30 min recording sea state. One can note the occurrence of extreme storm events for which H_s reaches more than 14m. It can thus be expected to encounter very high H_s of about 15m when considering 50 years return period wave.
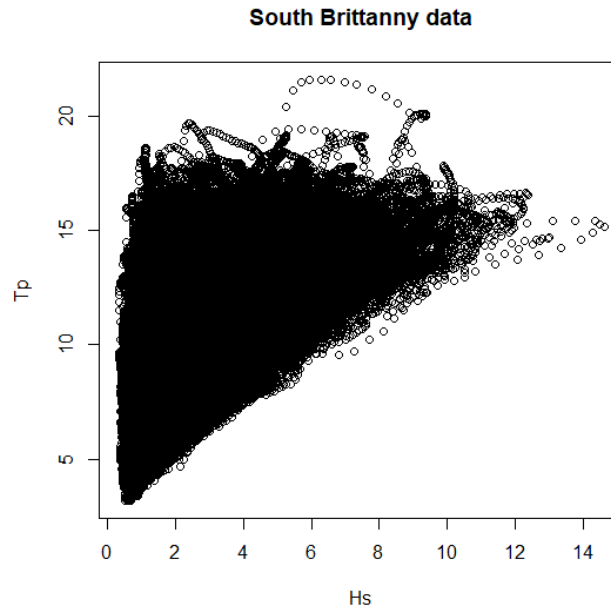
South Brittanny data

Figure 1 : wave parameters scatter plot from South Brittany site in ANEMOC data [1.]. T_p in s vs H_s in m.

Previous work of HIPERWIND was considering a floating OWT with a modified version, namely with tower changes [5.], of IEA15MW on UMaine semi-submersible floater from the original design of [3.][4.]. A code to code comparison between DLW, Diego, and HAWC2 implementations of this model is documented in [6.]. While the comparison concludes with a general good agreement between the 3 models, it also shows that the model is not well designed against the 50 years extreme wave that can be encountered in South Brittany. Indeed, the mooring lines are not kept in high tension enough because of dynamic slack, particularly for the line which is aligned with the wave direction. To avoid such a problem, we have redesigned the mooring lines of this model by adding a mass of 60t at 100m length from the top of the line (i.e. from the fairlead). This mass (submerged in water) is representing additional clump weights as it was for instance chosen for the OO-STAR design of LifeS50+ project for similar reasons. To keep the draft unchanged, the total added mass of 180t was subtracted from the mass of the floater and the center of gravity of the floater was recomputed.

The resulting design was checked against the Extreme Turbulence Model (ETM) and an Extreme Sea State (ESS) as defined in IEC design basis [7.][8.] for DLC 61 (aligned wind and waves) and DLC62 (misaligned wind of ±30°). The ESS was chosen to be with H_s set to 16.5m and T_p set to 16s for South Brittany site. It

was also verified that the maximum tension along the mooring line was not exceeding MBL/SF= 17.832 MN, with MBL the Maximum Breaking Load and SF being the safety factor of 1.25 given by for those DLC in [7.][8.].

The authors thanks the University of Maine for sharing their floater design and discussions about the design methodology.

References of Section 3

[1.] ANEMOC. (Atlas Numérique d'Etats de Mer Océaniques et Côtiers - Digital Atlas of Ocean and Coastal Sea States). http://anemoc.cetmef.developpement-durable.gouv.fr/

[2.] Müller, K., Lemmer, F., & Yu, W. (2018). Public definition of the two lifes50+ 10mw floater concepts. *Public report D*, *4*.

[3.] Allen, C., Viscelli, A., Dagher, H., Goupee, A., Gaertner, E., Abbas, N., ... & Barter, G. (2020). *Definition of the UMaine VolturnUS-S reference platform developed for the IEA Wind 15-megawatt offshore reference wind turbine* (No. NREL/TP-5000-76773). National Renewable Energy Lab. (NREL), Golden, CO (United States).

[4.] Evan Gaertner, Rinker, J., Sethuraman, L., Zahle, F., Anderson, B., Barter, G., Abbas, N., Meng, F., Bortolloti, P., Skrzypinski, W., Scott, G., Feil, R., Bredmose, H., Dykes, K., Sheilds, M., Allen, & C., Viselli, A. (2020). *Definition of the IEA wind 15-megawatt offshore reference wind turbine Tech. Rep*. NREL/TP-5000-75698 National Renewable Energy Laboratory Golden, CO.

[5.] Capaldo, M., Guiton, M., Huwart, G., Julan, E., Kramisirov Dimitrov, N., Kim, T., Lovera, A., & Peyrard, C. (2021). *Design brief of HIPERWIND offshore wind turbine cases: bottom fixed 10MW and floating 15MW*. https://www.hiperwind.eu/publications.

[6.] Kim, T., Natarajan, A., Lovera, A., Julan, E., Peyrard, C., Capaldo, M, Huwart, G., Bozonnet, P., & Guiton, M. (2022). A comprehensive code-to-code comparison study with the modified IEA15MW-UMaine Floating Wind Turbine for H2020 HIPERWIND project, submitted to Torque 2022 conference.

[7.] International Electrotechnical Commission. (2019). IEC 61400-3-1: 2019 Wind energy generation systems–Part 3-1: Design requirements for fixed offshore wind turbines.

[8.] International Electrotechnical Commission. (2019). IEC 61400-1: 2019 Wind energy generation systems–Part 1: Design requirements.

4. Hydrodynamic loading uncertainty

4.1. Fixed offshore wind turbine

4.1.1. Context and objectives

4.1.1.1. Objectives

The present section is dedicated to the bottom fixed foundations, specifically on monopiles which represent more than 80% of the installed offshore wind foundations [1]. Even though the turbines are becoming bigger and the water depth higher, this solution is expected to be a preferred option for many future projects. The full design of a monopile integrates many design load cases for ultimate and fatigue verification, screening various scenarios of the OWT life such as normal operation, shut-down, start-up, fault or storms. A leading factor in offshore wind turbine structures design is the suitability concerning mechanical fatigue. Both aerodynamic and hydrodynamic loads contribute significantly to mechanical fatigue, and the damage estimation is also sensitive to soil-structure interactions and fluid-structure coupling [2]. Notably, hydrodynamic loads can play a crucial role in fixed OWT fatigue considering:

- The operation in idling mode: for low or high wind speeds out of operating range, the turbine is not operating, and the aerodynamic damping is strongly reduced. The overall damping being at its minimum, the dynamic amplification factor is at its peak, so that wave excitation produces significant vibration amplitude and associated fatigue, despite low aerodynamic loads;
- The nonlinear nature of fatigue phenomena: fatigue is highly nonlinear with a consumption of fatigue life on steel structures generally proportional to the vibration amplitude at the power of 3 to 5. In this context, wave-induced vibration amplitudes, combined with aero-induced vibrations amplitudes, can significantly increase the fatigue damage.

Therefore, a way to optimize the monopile design is to provide a better estimation of the hydrodynamic load amplitude applied to the foundation. For fatigue analysis, a way to characterize the severity of cycling loadings is to extract a Damage Equivalent Load (DEL) from a load time series. The DEL is the sinusoidal load producing the same damage level as the time series (the DEL will be defined more accurately in the next sections).

The offshore wind industry has already started to work on this point, replacing progressively the well-known « Morison Equation » [3.] with the so-called « MacCamy-Fuchs correction » [4.]. The first one is a very popular wave load model, simple to implement and based on semi-empirical coefficients. However it is regarded as accurate only for small diameter piles and produce strong overestimation when the pile diameter exceeds 20% of the wavelength [5.]. The second is an analytical solution of the diffracted wave field and allows to get a more accurate load estimation for large diameter piles. Thus, it is not really a correction of the Morison inertia term, but mostly a generalization of the Morison inertia coefficient in the specific case of a vertical cylinder: instead of using a constant inertia coefficient $C_M=2$, this coefficient is given by:

$$C_M = \frac{4}{\pi} \frac{1}{|H'(kR)|} \frac{1}{(kR)^2}$$

with H' the first order Hankel function derivative, R the cylinder radius and k the wave number. A phase shift of the load wrt the Morison prediction is also associated with the inertia coefficient modification, although not systematically accounted for [6.].

For offshore wind monopiles, it was found that the MacCamy-Fuchs (MCF) correction was a way to reduce the fatigue loads as compared to the Morison equation (see [13.] for instance), because most of the sea states considered for fatigue are usually associated to small wave periods. Today the common engineering

design tools, like « Bladed » from DNV-GL, use the MCF correction as a standard option [6.]. The larger the monopiles will become in the future, the more this MCF correction will become important in the design.

The objective of the present section is to investigate uncertainty reduction by improving the modelling techniques, focusing on 2 aspects:

- First-order loads: these are usually the dominant loads, deriving from linear incident waves and linear diffraction. A study will be made on the geometry of the monopiles, given that the transition piece (TP) usually modifies the apparent diameter in the vicinity of the free surface. In engineering models like [6.], this geometry variation is not well accounted for when applying the MCF correction. Therefore, this « standard » MCF method will be compared to the results of a linear diffraction solver.
- Second-order loads: these loads are generated by nonlinearities in the wave field and/or in the loading model. The time-domain solvers inherently integrate second-order wave loads by computing the hydrodynamic force up to the instantaneous free surface, generating high frequencies in the force signal: the so-called « sum-frequency loads ». These sum-frequency loads will be compared to a more accurate solution of the second-order diffraction problem, in order to understand the level of conservatism expected from engineering time-domain models and its influence on the DEL.

Originally, a third point was to be investigated: the influence of the wave field nonlinearities. It will not be accounted for, we will simply use Airy waves associated with JONSWAP spectra. Wave nonlinearities are of course worth investigating but would require outputs from HIPERWIND WP2 that are not available yet. However, the influence of these nonlinearities will be verified later in the project.

4.1.1.2. Site characteristics and foundations used

Even though the work presented below will try to draw general conclusions, it is applied to the HIPERWIND project needs and is based on the following project choices:

- The water depth and wave characteristics are taken from the Teesside wind farm condition (site report [7.]). Given the axisymmetry of monopiles, the omnidirectional Hs/Tp scatter diagram has been considered to extract load cases representative of 20 years Teesside wave climate. More than 170 [Hs ;Tp] couples are systematically investigated, to draw DEL distribution over any wave conditions in the scatter diagram.

Table 1: Teesside Hs/Tp diagram high level data [7.] High occurrence cases in yellow to red and zero occurrence case in green

Hs(m)/Tp (s)	1	2	3	4	5	6	7	8	9	10	11	12	13	14	15	16	17	18	19	20	21	22	23
0,25																							
0,75																							
1,25																							
1,75																							
2,25																							
2,75																							
3,25																							
3,75																							
4,25																							
4,75																							
5,25																							
5,75																							
6,25																							
6,75																							
7,25																							
7,75																							
8,25																							

- The foundations are inspired from the Teesside 2.3MW system and the HIPERWIND 10MW generic system. The important parameters for this study are:
    o   the diameters of the piles,
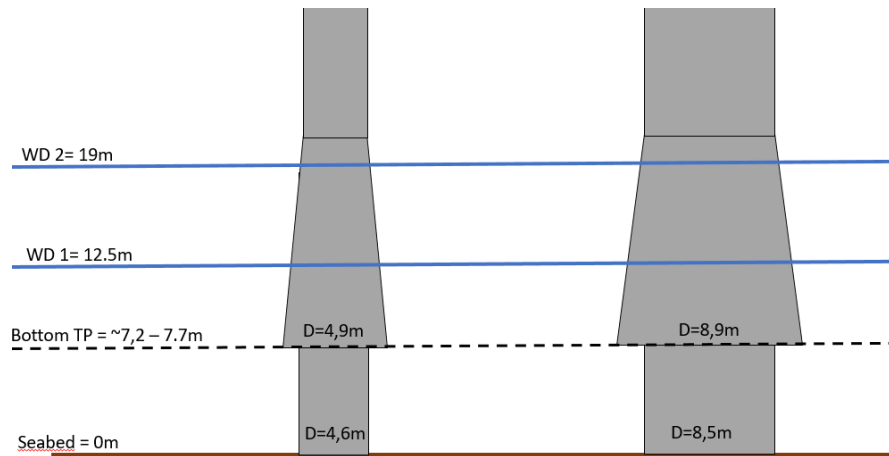   o   the diameters of the TP,
    o   the water depth.

WD 2= 19m
WD 1= 12.5m
Bottom TP = ~7,2 – 7.7m   D=4,9m   D=8,9m
Seabed = 0m   D=4,6m   D=8,5m

Figure 2: Geometries of the 2 monopile foundations (TP diameters are magnified).

4.1.1.3. Methodology

The methodology used in the present work aims at verifying the level of error due to the geometry of the monopiles when applying the MCF correction. Indeed, in an engineering design software, it is convenient to use the MCF correction in the frame of the Strip theory : kinematics are evaluated at each elevation of the pile (like it is done with the Morison equation) but the inertia coefficient C_M is computed using the MCF correction instead of using a user-defined value. In "Bladed", it was found more convenient to apply the MCF correction by modifying the wave energy itself rather than applying a frequency-dependent C_M [6.].

Therefore the MCF correction is used considering a constant diameter cylinder, which does not correspond exactly to the offshore wind turbine foundation geometry. To derive the MCF inertia coefficients, the reference diameter at the free surface location is chosen..

In the present work, the wave energy is not modified but each wave component is associated with an inertia coefficient applied to the acceleration components when computing the loads in a Morison-like framework. The inertia coefficient is based on the pile diameter at the free surface, thus the method is comparable to the Bladed one, even if not strictly equivalent.

Geometries :

To produce generic enough results, it has been decided to deal with a monopile geometry composed of 2 cylinders of different diameters D1 and D2. D2 is supposed to represent the TP diameter and D1 the pile diameter. To investigate the effect of having a larger or smaller diameter at the free surface level, 2 water depths are considered : a low water depth for which the large cylinder is crossing the free surface, and a high water depth for which the large cylinder is fully submerged, meaning the smaller diameter (D1) crosses the free surface. The water depths are based on the Teesside case, so as the diameters.
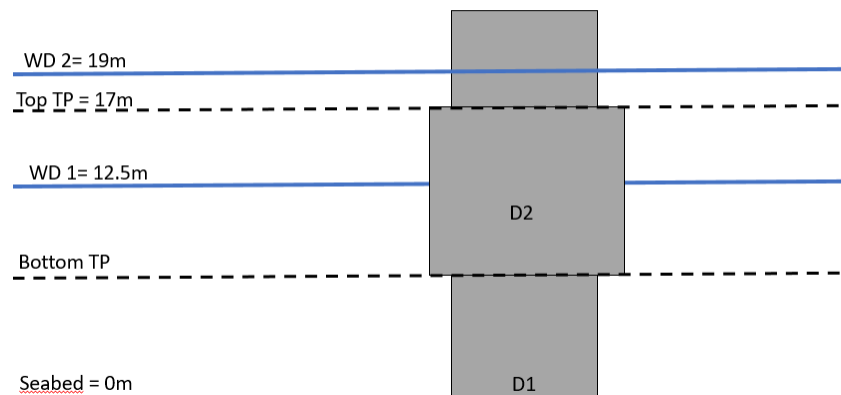

Figure 3: Geometry used for the first order study.

Two sets of foundation are analyzed:

- The first one is representative of the original **Teesside design**:
    - it uses D1=4.6m and two values of D2:
        - D2=4.9m which is the largest TP diameter,
        - D2=and 5.3m which is regarded as a variation to look at the tendency when increasing the TP diameter.
    - The bottom of the TP is located 7.5m above the seabed, the top 17m above the sea level.
- The second one is representative of the **DTU 10MW design** for Teesside:

- it uses D1=8.6m and two values of D2:
  - D2=9.0m which is the largest TP diameter,
  - D2=and 9.4m *which is regarded as a variation to look at the tendency when increasing the TP diameter.*
- The bottom of the TP is located 6.5m above the seabed, the top 17m above the sea level.

Site conditions:

The full *Hs*/*Tp* scatter diagram is investigated, except the wave periods lower than 3s and larger than 20s, to limit the computational burden in particular for the second order calculations. These conditions are not very significant for the fatigue analysis. The following figure provides the probability of occurrence of the *Hs*/*Tp* conditions. It is simply a plot of Table 1 but allows us get a more detailed view of the most probable conditions : low period waves with *Hs* lower than 2m.
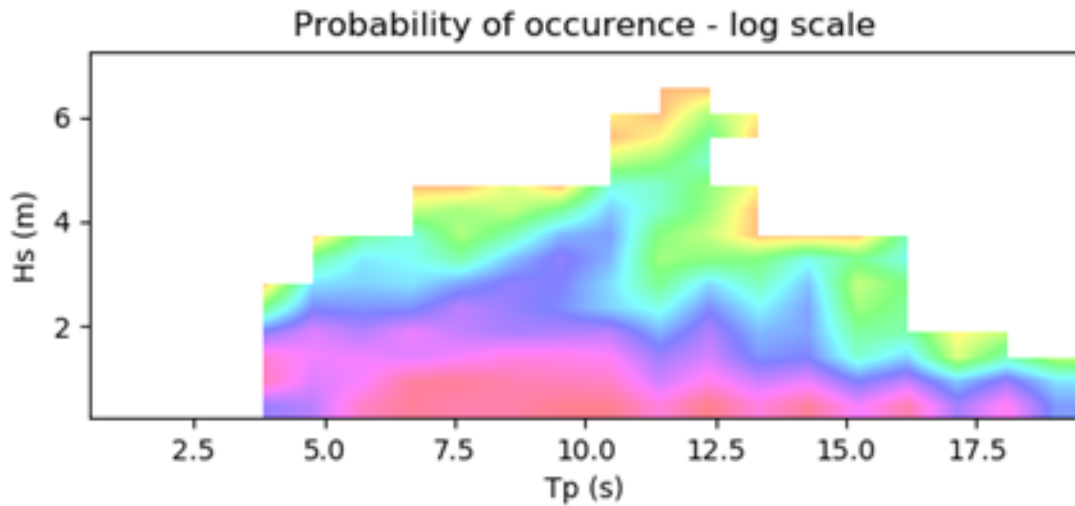
Figure 4: Probability of occurrence of [Hs,Tp] at Teeside, in log scale.

Foundation Geometry - First order comparison:

The influence of the geometry on the DEL is made by comparing two models:

- A "reference" model, called "Potential Flow", based on the linear diffraction solution obtained by the Boundary Element Method (BoEM). This model is regarded as a reference because it uses the exact geometry. The BoEM generates a hydrodynamic database used as an input of the time domain model.
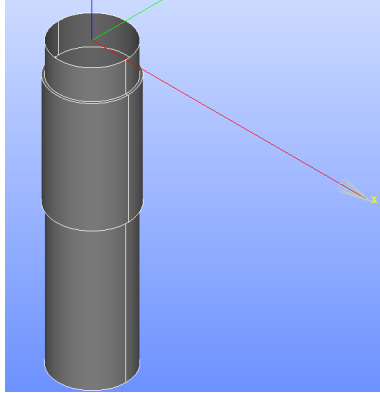
Figure.5: Geometry of the "reference model".

- The "engineering design" model, called MCF, based on the MCF solution and using the diameter at the waterline to apply the correction. This model runs in the time domain as well and any nonlinearity is removed by computing the loads on the initial wetted surface.

Both models are using irregular Airy waves as inputs.

Second order comparison:

The influence of the second-order wave loads on the DEL is made on purely circular cylindrical shape. Two models are compared:

- A "reference" model, called "Potential Flow", based on the resolution of first and second-order diffraction effects: linear and quadratic transfer functions (LTF and QTF). It is regarded as a reference because the nonlinear loads predicted integrate all the contribution of the diffracted wave field, including second-order diffracted waves.
- An "engineering design model", called "MCF", based on the MCF correction with an integration of the wave force until the instantaneous free surface level. This model is thus integrating second-order wave loads by the simple time-domain integration. This is representative of the current industry practice.

Both models use irregular Airy waves as input, but it is to be noticed that the "Potential Flow" model inherently integrates second-order waves deriving from the first order waves (full QTF model). Somehow, there is more energy in the "Potential Flow" wave field than in the "MCF" one. It would have been possible to integrate this additional energy in the MCF model, but it was chosen not to do so because it is far from the industry use and because the objective of this work is to quantify the difference between advanced models and the typical industry practice.

Outputs:

The outputs of these analyses are DEL maps, giving the DEL obtained for each [*Hs*;*Tp*] couple. To give more detail, for each [*Hs*;*Tp*] 3 simulations of 3h are launched on EDF clusters resulting in 3 DEL based on the overturning moment at the seabed. The mean value of this triplet is computed and reported on the DEL map. Using mean value make more robust the final figure, even if only small differences were observed between the runs. It is worth noting that the same sea state realizations were used for the different

models, limiting the dispersion of the results due to random phases selection. Thus, each analysis results in a figure as presented below:
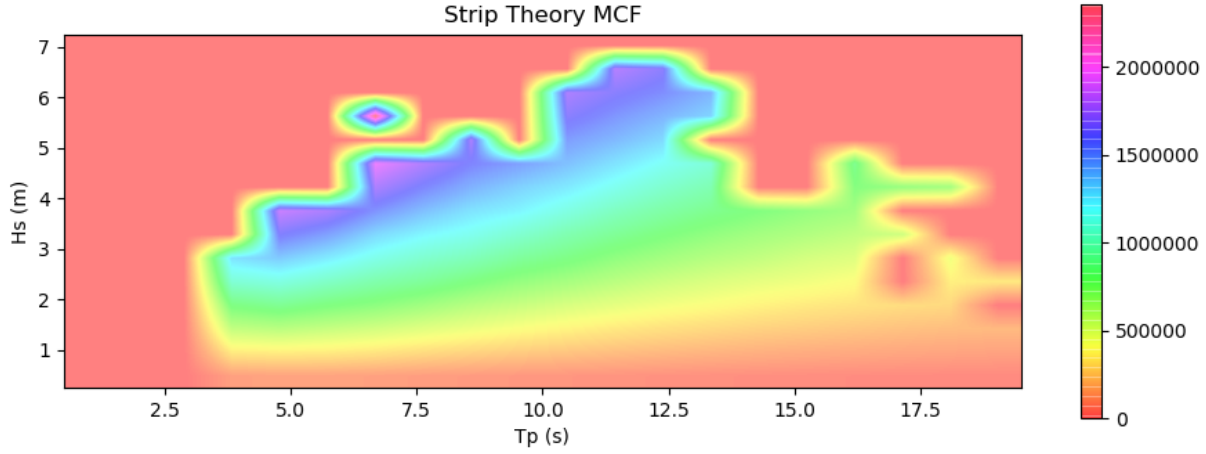

Figure 6: Exemple of « DEL map »: for each [Hs,Tp] couple the DEL value (in Nm) is plotted

The DEL follows the colormap and *Hs* and *Tp* give the axis values. Around the colored area, the red zone corresponds to simulations not launched because the [*Hs*;*Tp*] probability is zero.

The DEL proposed here is the overturning moment DEL, computed by the following method:

- Step 1: the hydrodynamic overturning moment applied at mudline is computed in the time domain
- Step 2: a rainflow counting is applied to the time series, to obtain a list of k cycles of amplitude ΔM_i and the number of occurrences n_i

ΔMy_1	n_1
…	…
ΔMy_k	n_k

- Step 3: the DEL is obtained

$$DEL = \sqrt[m]{\sum_{i=1}^{k} \frac{n_i}{N_{tot}} \Delta M_i{}^m}$$

With m=5 and N_{tot}=1e7, a typical value for steel S-N curves.

Damage calculation takes into account the Wöhler curve of the structure, that is often represented with a bilinear curve relating the number of cycles allowable to the corresponding alternative stress range. For the structural steel components, Wöhler exponent of 3 is used for the higher stresses, whereas exponent of 5 is used for the lower stresses. Usually most of the fatigue for wind turbine structures is generated in range of alternate stresses corresponding to lower stresses with an exponent 5. Damage Equivalent Load enables quick comparison and is a convenient concept for the present study and is a usual practice. However it assumes the use of a single slope Wöhler curve the exponent 5 has been chosen for the Wöhler curve of the monopiles.

Additionnally, it is possible to extract a global DEL accounting for the all set of simulations, weighting the results of each [Hs,Tp] conditions by the probability of occurrence of the conditions. This global DEL is then given by :

$$DEL_{global} = \sqrt[m]{\sum_{Hs,Tp} p(Hs,Tp) \sum_{i=1}^{k} \frac{n_i}{N_{tot}} \Delta M_i{}^m}$$

This allows to get a consolidated of the DEL and gives a high level view on the model comparison. However, one has to keep in mind we are discussing hydrodynamic DEL here, and no structural response is accounted for in the calculations. Thus, depending on the natural frequencies of the OWT, the DEL can be strongly affected.

4.1.1.4. Estimation of a potential bias:

As we will see later in this section, the difference in the DEL obtained from the models are usually in the range of [0-10%]. Thus, it looked important to check the difference one could obtained on the very same case computed in two different ways:

- the MCF model (strip theory directly integrated in the time domain),
- the Potential Flow model (importation of a hydrodynamic database into the time domain solver).

A vertical cylinder of 4.6m diameter in 12.5m water depth was chosen as test case, in that situation the MCF model is a strict analytical solution to the results provided by the Potential Flow model, thus no differences should be observed except due to the discretization and numerical resolution.

Indeed, the comparison leads to the figures presented below (Figure 7). One can see differences of less than 0.4% are obtained (in particular for the smaller periods), possibly due to the different discretization of the two models. A negative value means that the MCF model produces a lower DEL than the Potential Flow one. Therefore, differences of less than 1.0% will not be regarded as significant in the current study.
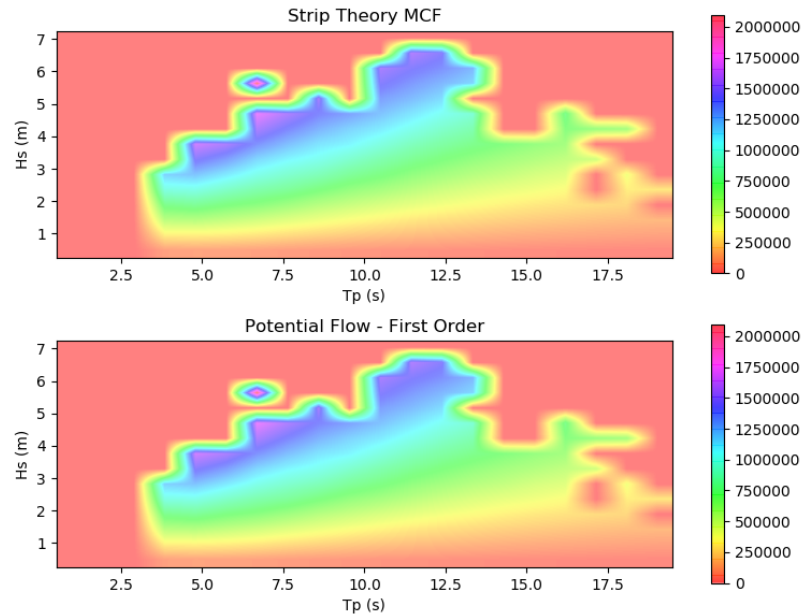
Figure 7: DEL map for a vertical cylinder using MCF (top) and the Potential flow theory (bottom) (unit: N.m)
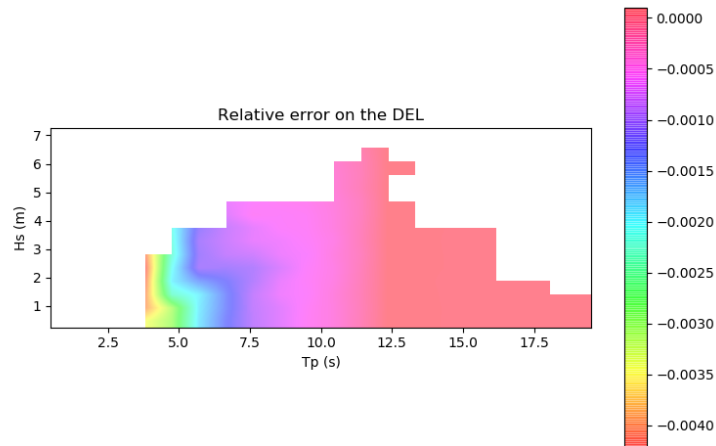

Figure 8: Relative error on the DEL: "MCF – Potential Flow" (Positive value indicates that MCF DEL is higher)

4.1.1.5. Software used

The tools used in this section are:

- DIEGO, the time domain solver of EDF R&D dedicated to OWT simulation. Here, DIEGO is used to generate waves and compute forces from the strip theory (MCF models) or hydrodynamic

databases (LTF and QTF models). It is distributed on EDF R&D clusters to get about 500 x 3h sea states computed in less than 30 minutes.

- NEMOH, the potential flow solver developed by ECN [8.]. NEMOH is used here to solve the first-order diffraction problem, it is distributed on EDFR&D clusters, to be able to get reliable results on 200 frequencies in less than 1h.
- Python modules to compute the first and second-order diffraction loads on vertical cylinders. These scripts were existing but were extended to be compliant with mass distributed calculation. Less than 1h was necessary to compute the second-order wave loads on 1800 wave couples.

4.1.2. First-order analysis: DEL uncertainty due to the monopile geometry

4.1.2.1. Geometries

As mentioned earlier, in this section we look at 8 configurations.

The first 4 ones correspond to the lowest water depth (12.5m), for which we consider the TP larger diameter is crossing the free surface. Teesside and DTU cases are considered (2 cases) with a « large diameter » variation for each of them (2 additional cases). In this section, the D2/D1 ratio will be used to characterize the case we are dealing with. One can note that the TP is proportionally larger in the Teesside case than in the DTU case, and that a factor 2 was applied on the (D2-D1) difference between the base cases and the « large » cases.

Table 2: Low water depth cases (12.5m)

	D1 (m)	D2 (m)	Cross Waterline diameter (m)	D2/D1
Teeside-like / Base	4,6	4,9	4,9	107%
Teeside-like / Large	4,6	5,3	5,3	115%
DTU-like / Base	8,6	9	9	105%
DTU-like / Large	8,6	9,4	9,4	109%

The last 4 cases correspond to the highest water depth (19m), for which we consider the TP lower diameter (taken equal to the pile diameter) is crossing the free surface. Teesside and DTU cases are considered (2 cases) with a « large diameter » variation for each of them (2 additional cases).

Table 3: High water depth cases (19m)

	D1 (m)	D2 (m)	Cross Waterline diameter (m)	D2/D1
Teeside-like / Base	4,6	4,9	4,6	107%
Teeside-like / Large	4,6	5,3	4,6	115%
DTU-like / Base	8,6	9	8,6	105%
DTU-like / Large	8,6	9,4	8,6	109%

4.1.2.2. Models

For the MCF model, the DIEGO simulation is run with the following parameters:

- no drag considered,
- wave forces integrated until the mean sea level (« FreeSurface=0 option »),
- vertical stretching.

For the Potential Flow model, the DIEGO simulation is run with the following parameters:

- no drag considered,
- wave forces taken from the NEMOH hydrodynamic database, relying on a meshing of the exact geometry (Figure 9).
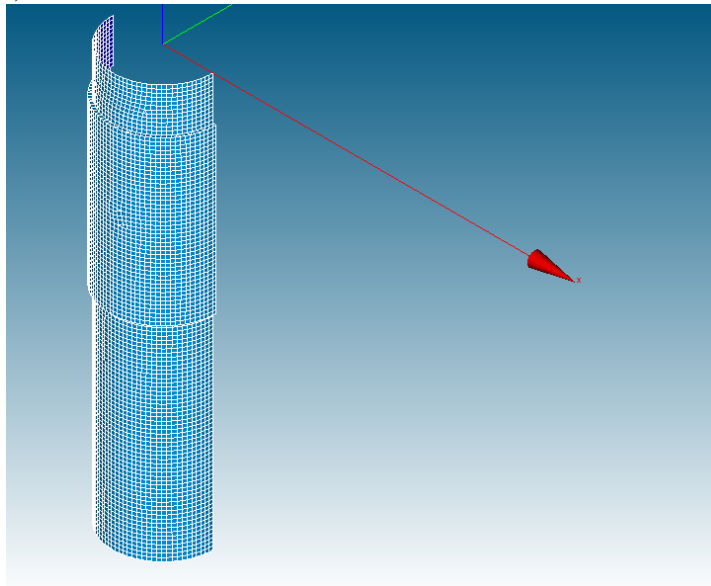

Figure 9: Example of hydrodynamic mesh computed with SALOME and used for NEMOH.

Given these assumptions, both models are expected to produce purely linear loads.

4.1.2.3. Low water depth: Results on the DEL

In this section the water depth is 12.5m and the larger diameter of the foundation crosses the waterline. This large diameter is taken into account when computing the MCF inertia coefficient.

Teesside case:

The Teesside base case (Figure 10) shows a global overestimation of the MCF model as compared to the Potential Flow one, regarded as more reliable. For the lowest periods, the difference is not significant but can reach 4% for the largest ones. We believe this is due to the deeper penetration of the kinematics in the water column for long waves. No significant difference is obtained when increasing the *Hs* at a given *Tp*, which was quite expected considering the linearity of the models. Computing a global DEL on the full

scatter diagram, accounting for the probability of occurrence of each [Hs;Tp] couple, results in a 2% overestimation of the DEL by the MCF model as compared to the Potential Flow.
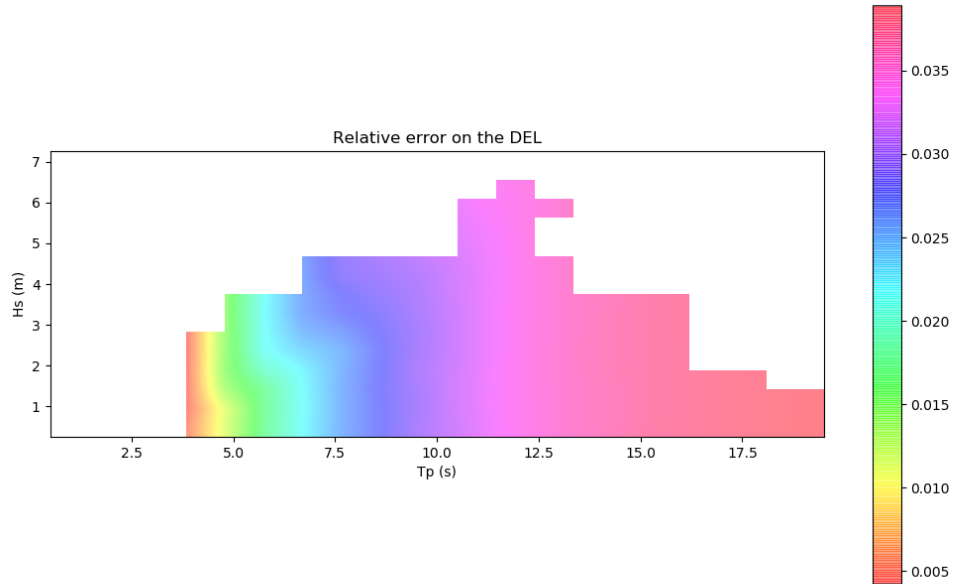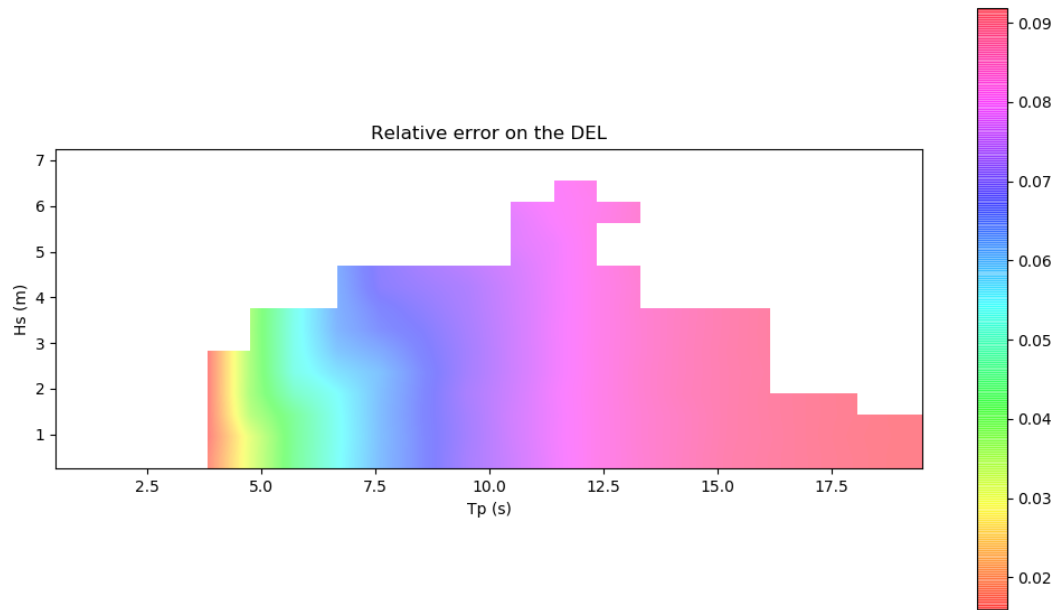

Figure 10: Water depth = 12.5m. Teesside D2/D1=107% case. Relative DEL error between MCF and the Potential Flow theory (positive value means MCF produces higher DEL).

Moving to the larger diameter case, with D2/D1=115%, we obtained the same tendency but with an increase in the DEL overestimation, up to 9% (Figure 11).

Figure 11: Water depth = 12.5m. Teesside D2/D1=115% case. Relative DEL error between MCF and the Potential Flow theory (positive value means MCF produces higher DEL).

DTU case :

For the DTU case, the tendency is the same, with an overestimation of the DEL by the MCF model and more differences observed on the larger periods (Figure 12). Quantitatively, the overestimation is lower, with less than 2%. This can be explained by the lower D2/D1 ratio: 104% here against 107% for Teesside. Computing a global DEL on the full scatter diagram, accounting for the probability of occurrence of each [Hs;Tp] couple, results in a 1% overestimation of the DEL by the MCF model as compared to the Potential Flow.
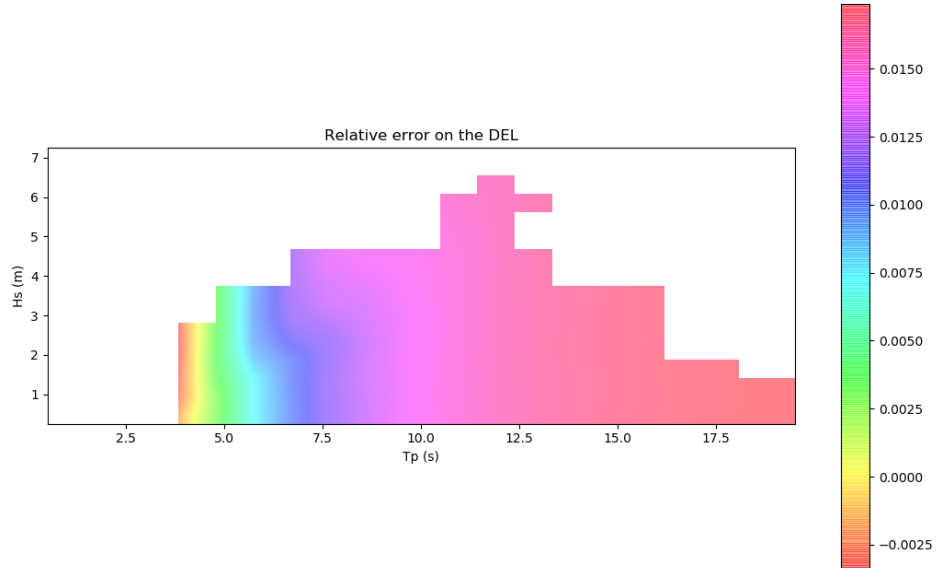
Figure 12: Water depth = 12.5m. DTU D2/D1=104% case. Relative DEL error between MCF and the Potential Flow theory (positive value means MCF produces higher DEL).

Moving to a larger TP (D2/D1=109%) mechanically increases the difference we observe (Figure 13), with a maximum difference of 3.5%, quite in line with the Teesside base case (D2/D1=107%).
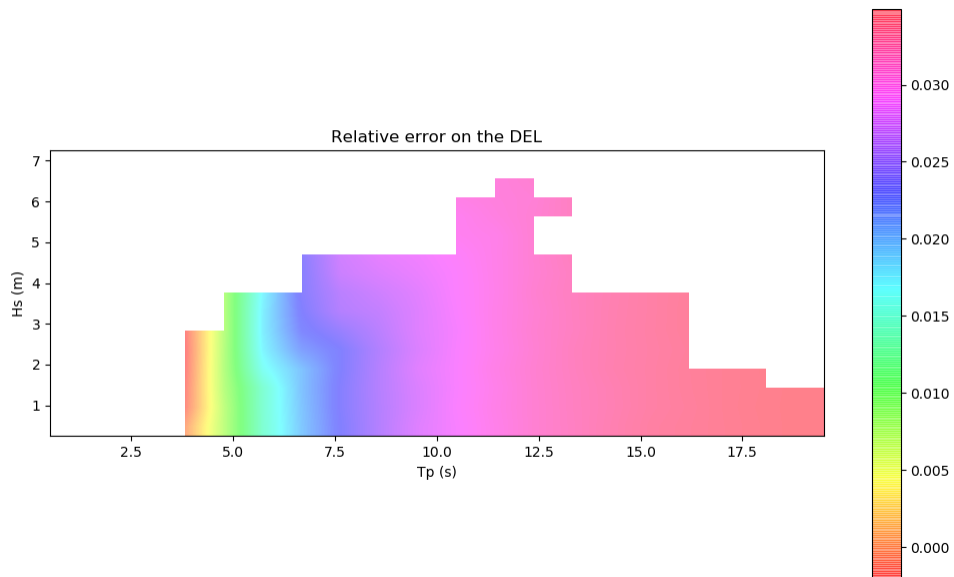

Figure 13: Water depth = 12.5m. DTU D2/D1=109% case. Relative DEL error between MCF and the Potential Flow theory (positive value means MCF produces higher DEL).

23

4.1.2.4. High water depth: Results on the DEL

The same comparison is made for the high water depth (19m), for which the small diameter crosses the waterline and is thus used to compute the MCF inertia coefficient. The difference with the 12.5m water depth case is not only the water depth, but also the diameter used to compute the MCF loads.

Teesside case:

The Teesside base case (Figure 14) now shows an underestimation of the DEL by the MCF models, in the range of -7% on a large range of wave peak periods. The lowest differences are obtained for the shortest periods, probably again because the kinematics of short waves does not affect all the water column. As already observed, there is little variation of the DEL against the wave height because the loading model is linear. Computing a global DEL on the full scatter diagram, accounting for the probability of occurrence of each [Hs;Tp] couple, results in a -7% underestimation of the DEL by the MCF model as compared to the Potential Flow.
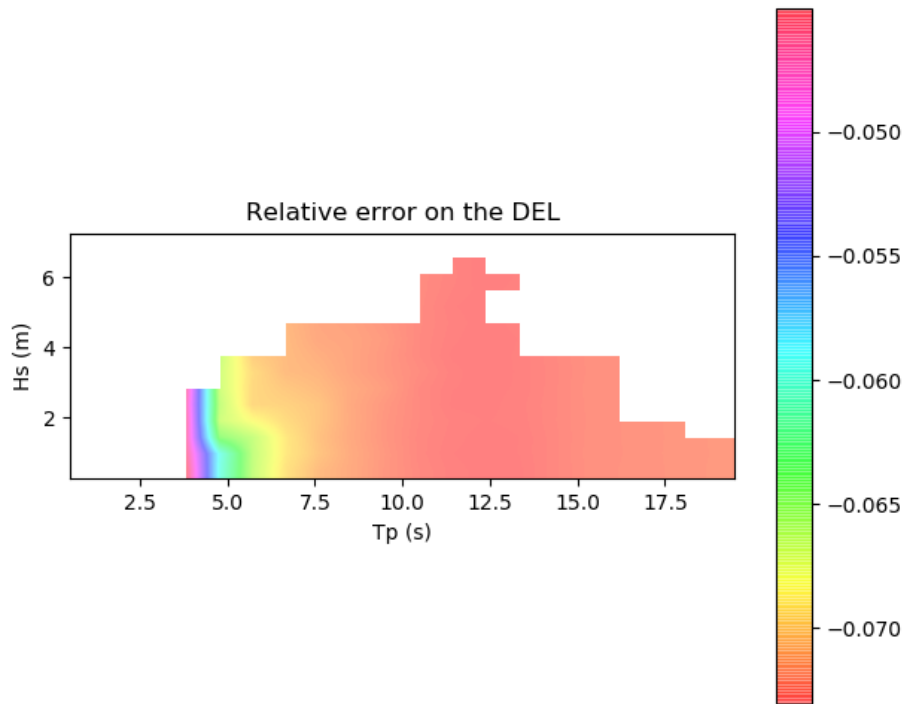

Figure 14: Water depth = 19m. Teesside D2/D1=107% case.
Relative DEL error between MCF and the Potential Flow theory (positive value means MCF produces higher DEL).

Increasing the TP diameter (D2/D1 ratio from 107% to 115%) almost double the differences observed (Figure 15), with an underestimation of 15% from the MCF model compared to the Potential Flow model.
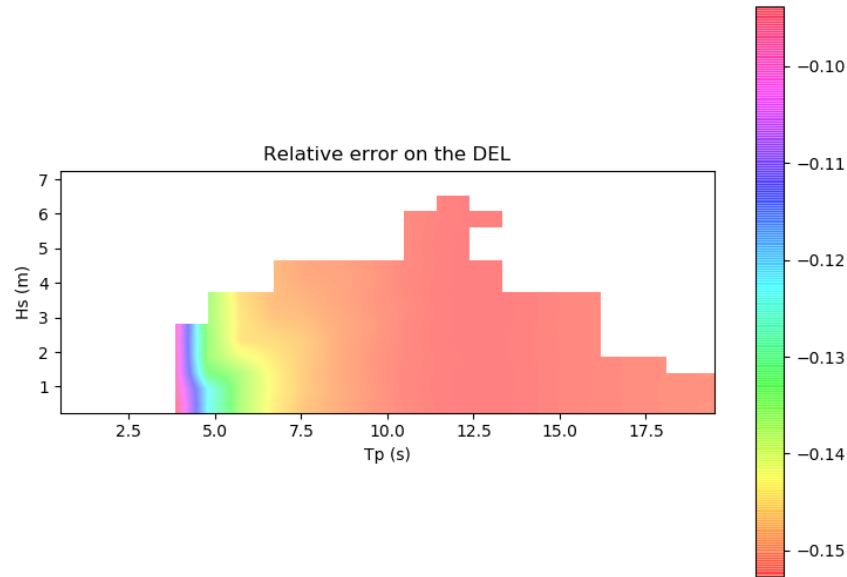
Figure 15: Water depth = 19m. Teesside D2/D1=115% case.
Relative DEL error between MCF and the Potential Flow theory (positive value means MCF produces higher DEL).

DTU 10MW case:

Moving to a larger foundation (Figure 16 and Figure 17) with the DTU 10MW – like system, the relative difference between MCF and the Potential Flow is reduced to 0 to -5%, MCF being here again less conservative, in particular for the wave peak periods above 7.5s. Computing a global DEL on the full scatter diagram, accounting for the probability of occurrence of each [Hs;Tp] couple, results in a -5% underestimation of the DEL by the MCF model as compared to the Potential Flow.
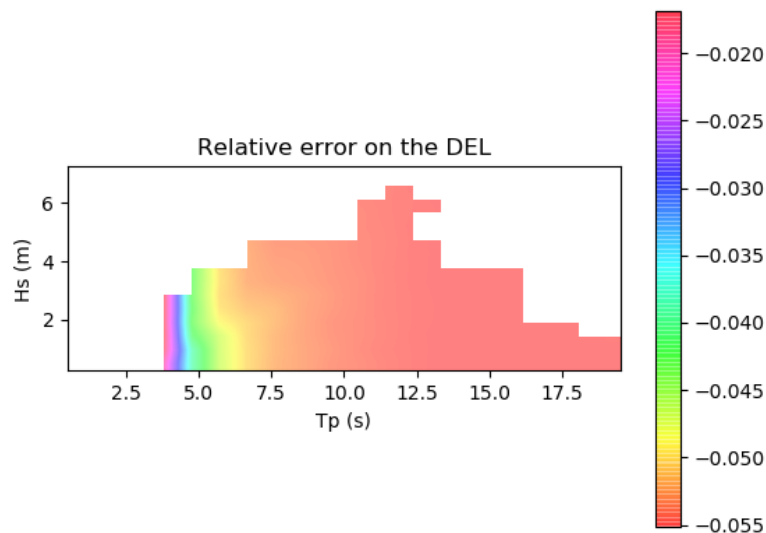

Figure 16: Water depth = 19m. DTU D2/D1=104% case.
Relative DEL error between MCF and the Potential Flow theory (positive value means MCF produces higher DEL).

As seen for the Teesside case, increasing the TP diameter increases the difference between the two models until -9%.
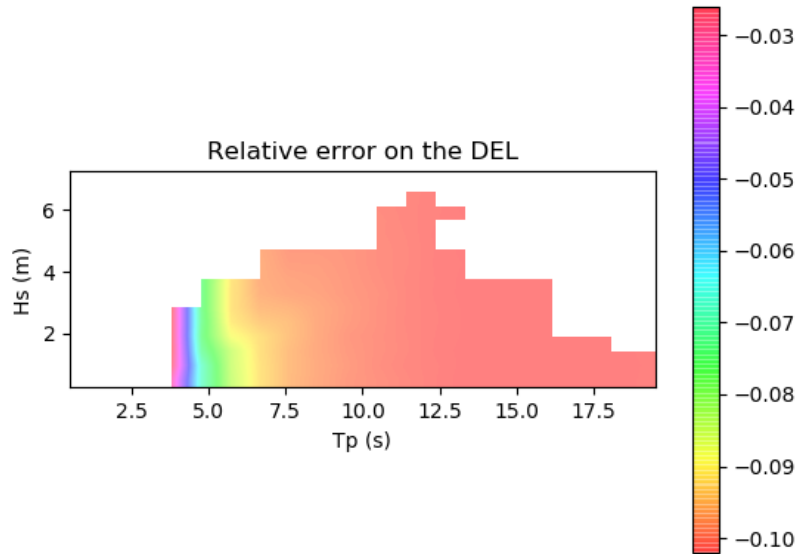

Figure 17: Water depth = 19m. DTU D2/D1=109% case.
Relative DEL error between MCF and the Potential Flow theory (positive value means MCF produces higher DEL).

4.1.3. Second order analysis: DEL uncertainty due to nonlinear wave loads

4.1.3.1. Geometries

Moving to nonlinear wave loads, we now come back to pure circular cylinders and focus on the effects of nonlinear loads on the DEL. As before, two water depths and two foundations diameters are studied here, to screen different conditions and to address both Teesside 2.3MW and a larger turbine case. As for the previous comparison, water depths of 12.5m and 19m are used.
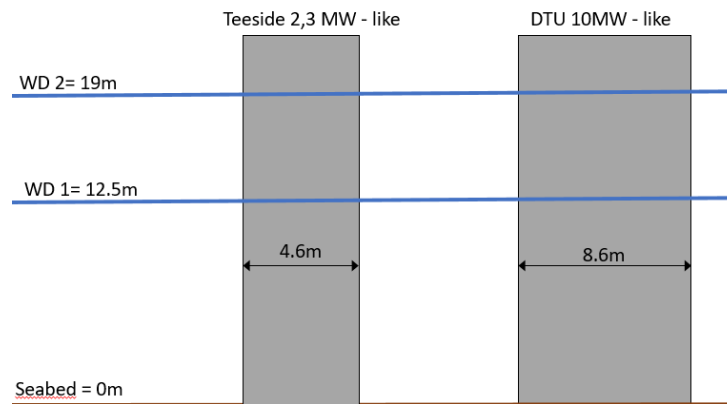
Figure 18: Geometries studied for the nonlinear wave loads

4.1.3.2. Models

On one side, we have the MCF model applied in the time domain accounting for the instantaneous position of the free surface, corresponding to the standard industry method. No specific validation has been performed for HIPERWIND, given the code has its own validation procedure.

On the other side, we compute the diffraction solution up to second order using a python module able to deal with axisymmetric bodies in waves, following MCF and Kim&Yue papers [4.][9.][10.]. The model is a potential flow model again and will be called « Potential Flow » as well. It includes this time the Linear Transfer Functions (LTF) of the wave loads as well as the Quadratic Transfer Functions (QTF) computed under the « full-QTF » assumptions: no second-order term is omitted. Given this model relies on a Python module and has been re-organized for this project purpose, elements of validation are provided below.

First-order validation:

The Python module is simply an implementation of the MCF solution and is validated against the NEMOH solution for a vertical cylinder. In this specific case, the diameter is set to 4.6m and the water depth to 12.5m. The agreement presented on Figure 19 is excellent.
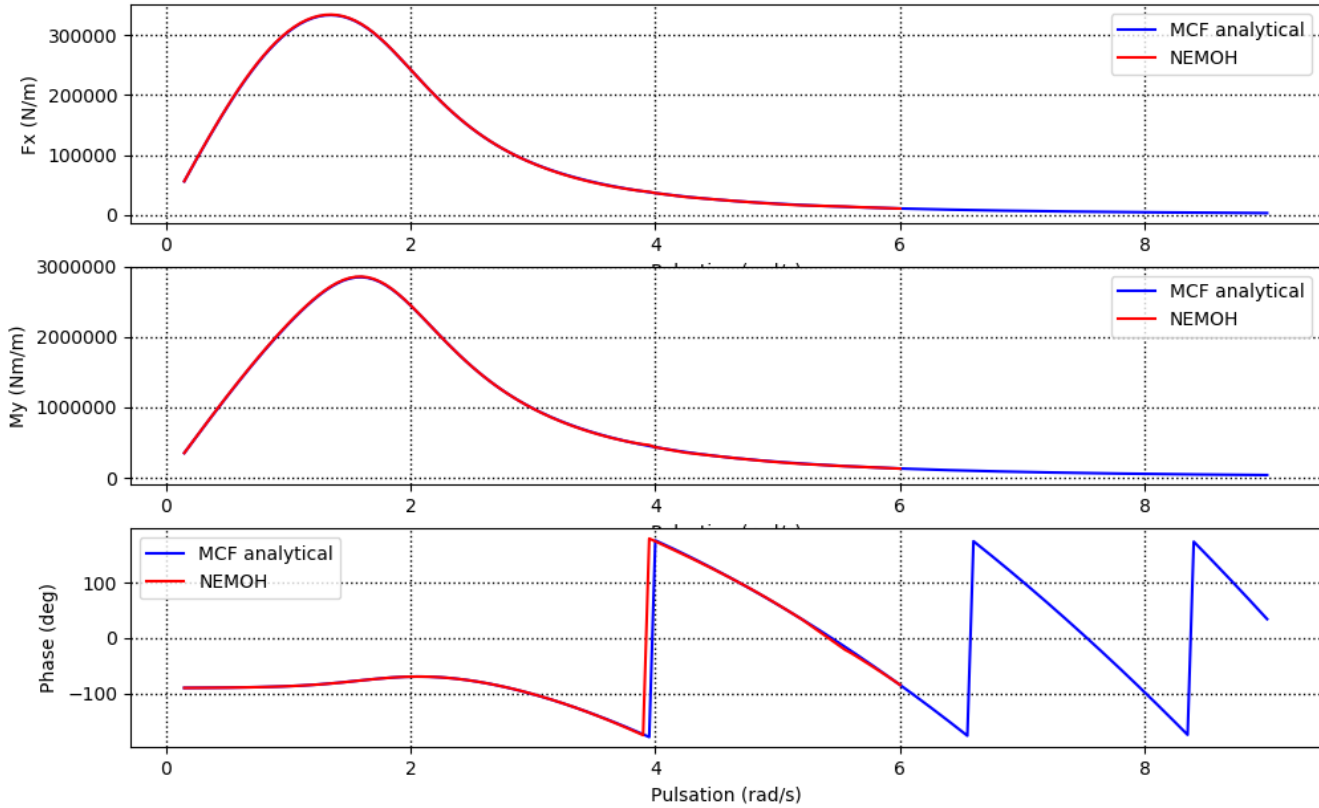
Figure 19: MCF Python implementation compared with NEMOH solution for a vertical cylinder of 4.6m diameter in 12.5m water depth. Horizontal force (top), Overturning moment at seabed (center) and phase relative to the free surface elevation (bottom). Abscissa are pulsations.

Second-order validation:

The validation is made on the Kim & Yue paper directly [10.], as their solution has been verified by several independent methods and several independent authors. The conditions studied in this section use a ratio *d/a*=4 (*d* being the water depth and *a* being the radius of the pile), in the Python module *d*=27m has been used.

Kim and Yue presented both horizontal forces and overturning moment. To keep a reasonably small validation section, we focused on the overturning moment only. It is presented normalized by ρ g a^2, ρ and g being respectively the water density and the gravity acceleration.

We note that in [10.] the *d/a*=1 case results are also presented. This case was also successfully verified by EDF R&D but not presented in this report, given it is a bit less representative of our Teesside and DTU cases. For Teesside and DTU, the *d/a* ratio varies between 1,45 and 4,1.

On the following figures (Figure 19 to Figure 21), the QTF of the overturning moment at seabed are presented in color against the reduced wave frequency $v\,a = \frac{\omega^2}{g}\,a$ of the 2 wave components generating the second order wave load. One can see the very nice agreement obtained against [10.]. The difference between EDF R&D and the reference result is plotted (Figure 21) and stays lower than 0.06 in absolute value, thus less than 1%.
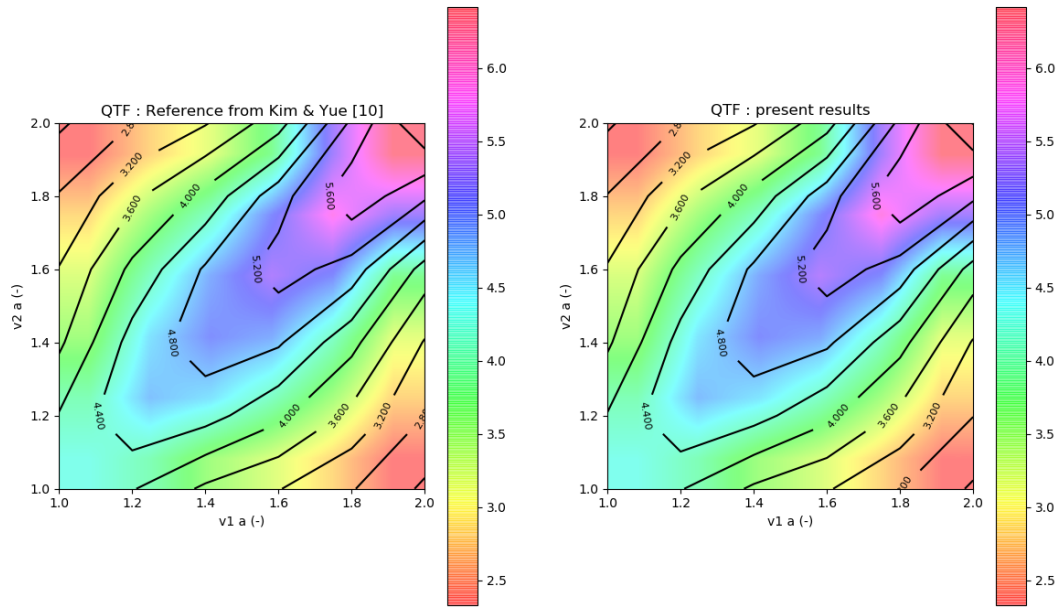

Figure 20: Overturning moment at seabed QTF. Kim & Yue reference results (left [10.]]) and EDF Python module (right). The two axes give are the wave reduced frequency.

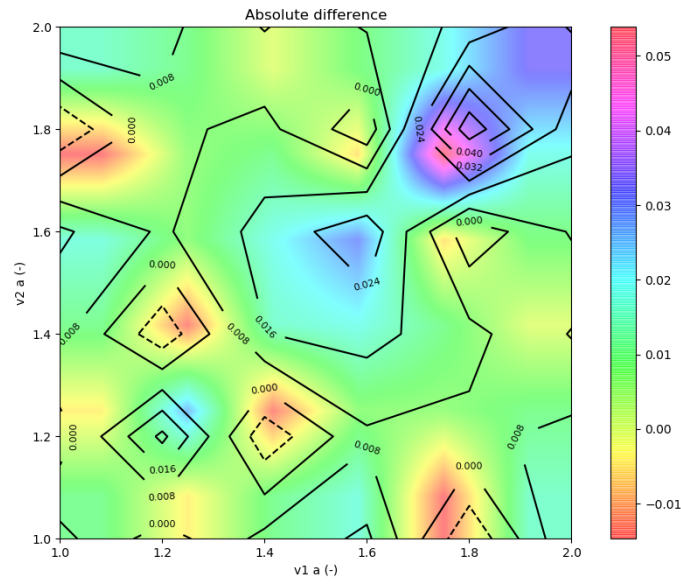*Figure 21: Error on the overturning moment at seabed QTF. Kim & Yue reference results - EDF Python module. Negative values indicate that EDF result is below the reference. The two axes give are the wave reduced frequency*
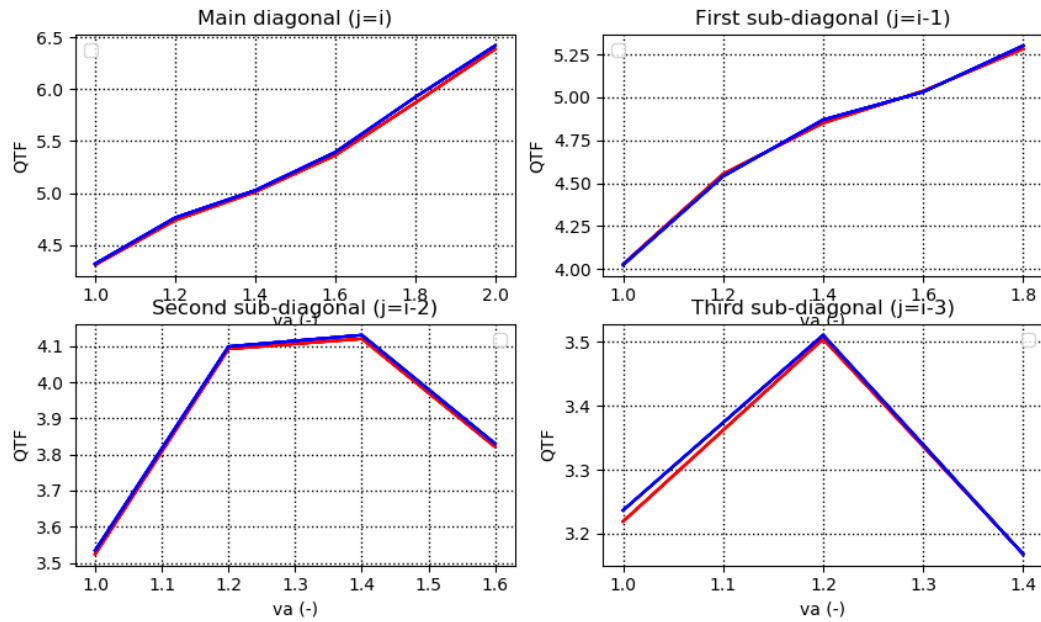

Figure 22: Overturning moment at seabed QTF matrix diagonal and sub-diagonal against reduced frequency. Reference results from [10] (red) compared to present result (blue).

4.1.3.3. QTF comparison

Before moving to the DEL maps, it seems useful to estimate the second-order loads predicted by both models. The first order loads have been somehow compared on the Teesside case when estimating the potential bias (Figure 8).

The second order wave loads coming from the Potential Flow solver can be obtained by the method presented above. For the MCF model, these loads can be estimated by the integration of wave loads in the crest of the wave, on the pile section that is sometimes below water (no wave loads) and sometimes in the water (wave loads). Following [11.] the second-order loads deriving from the strip theory are given by

$$F^{(2)} = \int_0^\eta F(z)dz \approx \eta \cdot F(z=0)$$

and the moment at seabed by

$$M^{(2)} = \int_0^\eta F(z) \cdot (d+z) \cdot dz \approx \eta \cdot F(z=0) \cdot d$$

with η and d respectively the free surface elevation (time-dependent) and the mean water depth.

In the case of bichromatic waves like those considered in [10.], one can write:

$$\eta = a_1 cos(k_1 x - \omega_1 t + \varphi_1) + a_2 cos(k_2 x - \omega_2 t + \varphi_2)$$

Following MCF loads formulation, we can write the horizontal force per unit length around z=0 like:

$$F(z=0) = C_1 a_1 cos(k_1 x - \omega_1 t + \varphi_1 + \psi_1) + C_2 a_2 cos(k_2 x - \omega_2 t + \varphi_2 + \psi_2)$$

C_i, ψ_i (i=1,2) being respectively the amplitude and phase of the MCF transfer functions, defined by:

$$C_i = \rho \pi R^2 g k_i \frac{4}{\pi} \frac{1}{|H'(k_i R)|} \frac{1}{(k_i R)^2}$$

and

$$\psi_i = -atan\left(\frac{Y_1'(k_i R)}{J_1'(k_i R)}\right)$$

With J_1', Y_1' and H' the derivative of the first order Bessel fist kind, Bessel second kind and Hankel functions respectively.

Thus, the second order overturning moment is:

$$M^{(2)} = M^{(2+)} + M^{(2-)}$$

with

$$M^{(2+)} = \frac{1}{2}a_1{}^2 C_1 \cos(2\tau_1 + \psi_1) + \frac{1}{2}a_2{}^2 C_2 \cos(2\tau_2 + \psi_2) + 2$$
$$\cdot \frac{1}{4}a_1 a_2 [C_1 \cos(\tau_1 + \tau_2 + \psi_1) + C_2 \cos(\tau_1 + \tau_2 + \psi_2)]$$

$$M^{(2-)} = \frac{1}{2}a_1{}^2 C_1 \cos(\psi_1) + \frac{1}{2}a_2{}^2 C_2 \cos(\psi_2) + 2$$
$$\cdot \frac{1}{4}a_1 a_2 [C_1 \cos(\tau_1 - \tau_2 + \psi_1) + C_2 \cos(\tau_2 - \tau_1 + \psi_2)]$$

with

$$\tau_i = k_i x - \omega_i t + \varphi_i$$

Our focus here is the sum-frequency moment, $M^{(2+)}$, associated to high frequency loads that generate many cycles.

From the expression of $M^{(2+)}$ it is possible to extract the amplitude and phase of the QTF matrix, as for each couple of frequencies 1-2 we have:

$$M_{12}{}^{(2+)} = a_1 a_2 \cdot q_{12} \cdot \cos(\tau_1 + \tau_2 + \alpha_{12})$$

$$with: \; q_{12} = \frac{1}{4}\{[C_1 \cos(\psi_1) + C_2 \cos(\psi_2)]^2 + [C_1 \sin(\psi_1) + C_2 \sin(\psi_2)]^2\}^{1/2}$$

$$and: \; \alpha_{12} = atan\left(\frac{[C_1 \sin(\psi_1) + C_2 \sin(\psi_2)]}{[C_1 \cos(\psi_1) + C_2 \cos(\psi_2)]}\right)$$

Thus, the real and imaginary parts of the second-order moment can be compared to the full QTF solution for any couple of frequencies. This comparison is presented in the figures below for *d=12.5m* and *D=2a=4.6m* (Figure 23 and Figure 24).
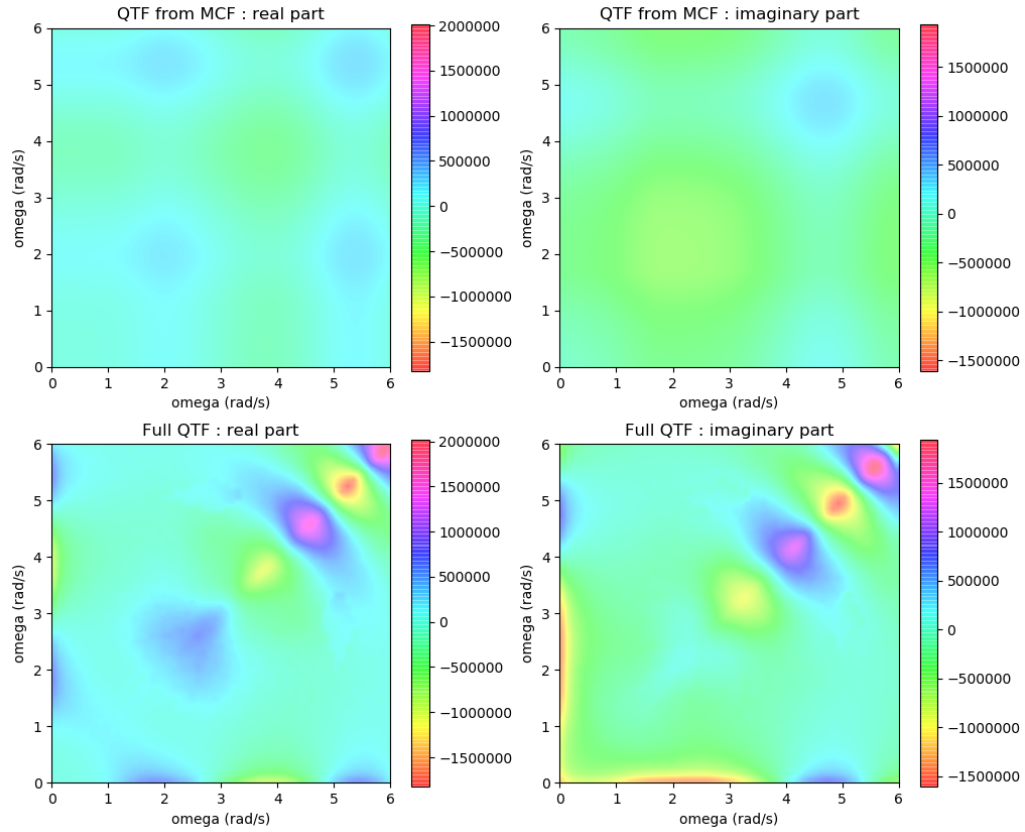
Figure 23: Overturning moment at seabed QTF matrices real (left) and imaginary (right) parts for MCF (top) and Potential Flow (bottom) methods. The two axes are pulsations.
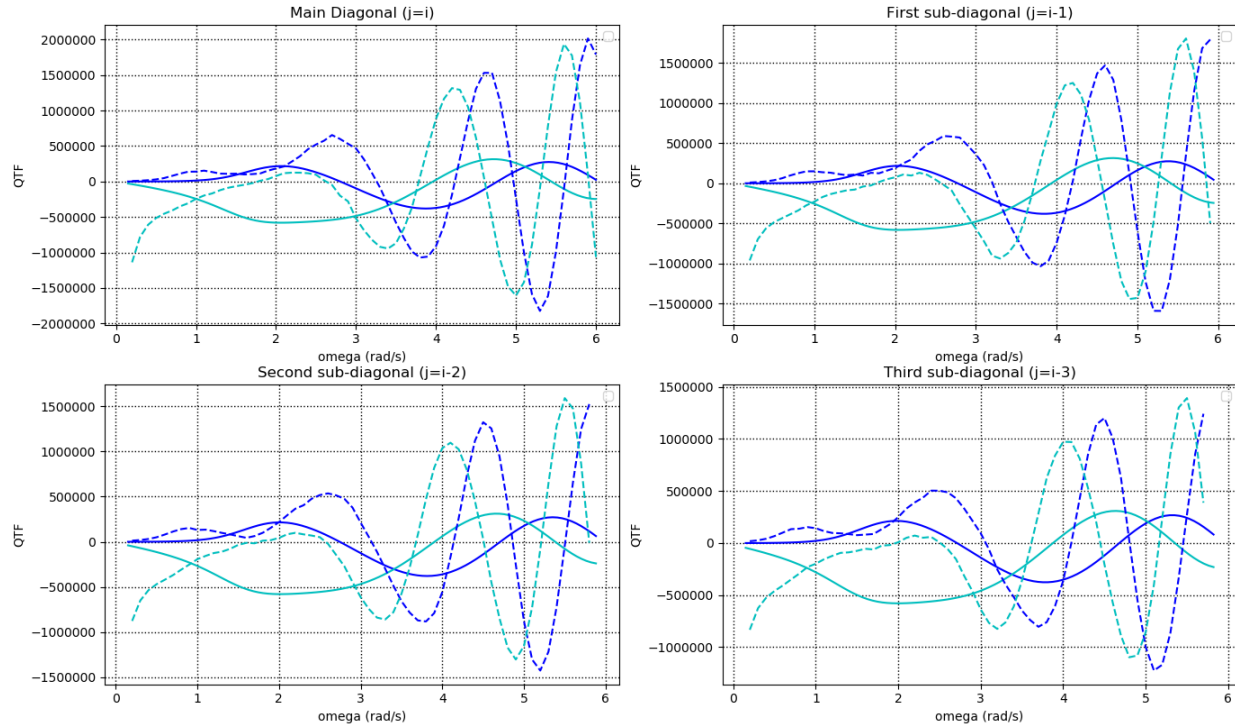
Figure 24: Overturning moment at seabed QTF matrix diagonal and sub-diagonal wrt pulsation.
Potential Flow (dot lines) and MCF (plain lines). Real (dark blue) and imaginary (light blue) parts.

On can see the very different behavior of the second-order wave loads. At high frequencies the Potential Flow ("full-QTF") exhibits large amplitude oscillations and the imaginary part is dominant at low frequencies. The MCF presents small loads at low frequency but produces a significant imaginary part for ω~2 rad/s, and almost no real contribution under $\omega<0.5$ rad/s.

4.1.3.4. Low water depth: Results on the DEL

As in the section devoted to monopile geometries, the DEL maps have been computed from the time domain model, the water depth considered in this section is 12.5m.

Teesside case:

On the figure below (Figure 25), the DEL computed by the MCF model is compared to the Potential Flow model. The relative difference is plotted: positive values means the MCF predictions are higher, and the difference is normalized by the Potential Flow value. Several points deserve to be underlined:

- First, the differences are only due to second -order loads, as it was found that the linear forces are strictly equivalent (less than 0.5% difference on the whole DEL map);
- The difference between the two models depends both on the wave peak period and the significant wave height, as the loads are nonlinear. For small waves, the difference is limited, because the DEL is fully driven by the linear forces;
- The MFC model seems to produce higher loads than the Potential Flow model at low periods, and lower loads at long periods. The reason is partly explained by the large QTF values of the Potential Flow at low frequencies and by the larger QTF values of the MCF model for pulsations between 1 and 3 rad/s;
- The effects of second-order wave loads can be quite significant, between -40% and +20% depending on the [Hs,Tp] couple, even though for the most probable sea conditions MCF seems to predict overestimations in the range of [0% => + 10%].
- In the end, computing a global DEL on the full scatter diagram, accounting for the probability of occurrence of each [Hs;Tp] couple, results in a -13% underestimation of the DEL by the MCF model as compared to the Potential Flow.

DTU 10MW case:

The same cases were studied with the larger DTU 10MW foundation. The same tendency as for Teesside is observed (Figure 26), with overestimations of the MCF model by about [0% => 10%] for the dominant wave conditions at Teesside, and differences of -40% to +15% depending on the [Hs,Tp] couple. MCF looks less conservative in the range of periods above 11s, for the larger sea states. Computing a global DEL on the full scatter diagram, accounting for the probability of occurrence of each [Hs;Tp] couple, results in a -14% underestimation of the DEL by the MCF model as compared to the Potential Flow.
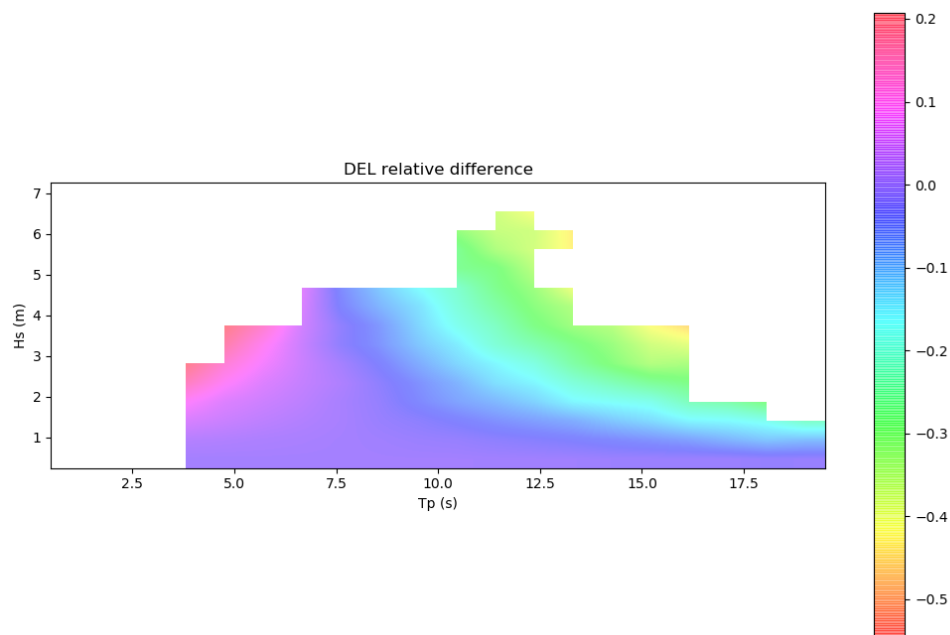

Figure 26: Water depth = 12.5m. DTU D=8.6m case.
Relative DEL error between MCF and the Potential Flow theory (positive value means MCF produces higher DEL).

4.1.3.5. High water depth: results in the DEL

Teesside case:

The difference in the DEL predicted by MCF and the Potential Flow is presented below as a relative difference again (Figure 27), the Potential Flow being considered as the reference value. The tendency is the same as the one observed in the 12.5m water depth, with an overprediction of the MCF model for short periods and an underprediction for the long periods. When waves are small enough to make the second order loads irrelevant, there is almost no impact on the DEL as one could expect. Computing a global DEL

on the full scatter diagram, accounting for the probability of occurrence of each [Hs;Tp] couple, results in a -1,2% underestimation of the DEL by the MCF model as compared to the Potential Flow.

Figure 27: Water depth = 19m. Teesside D=4.6m case.
Relative DEL error between MCF and the Potential Flow theory (positive value means MCF produces higher DEL).

DTU 10MW case:

The same observations are made for the larger monopile (Figure 28), with a slightly less important underestimation of the MCF DEL at a large period, but the global behavior is comparable to the small monopile case. Computing a global DEL on the full scatter diagram, accounting for the probability of occurrence of each [Hs;Tp] couple, results in a -1,2% underestimation of the DEL by the MCF model as compared to the Potential Flow.
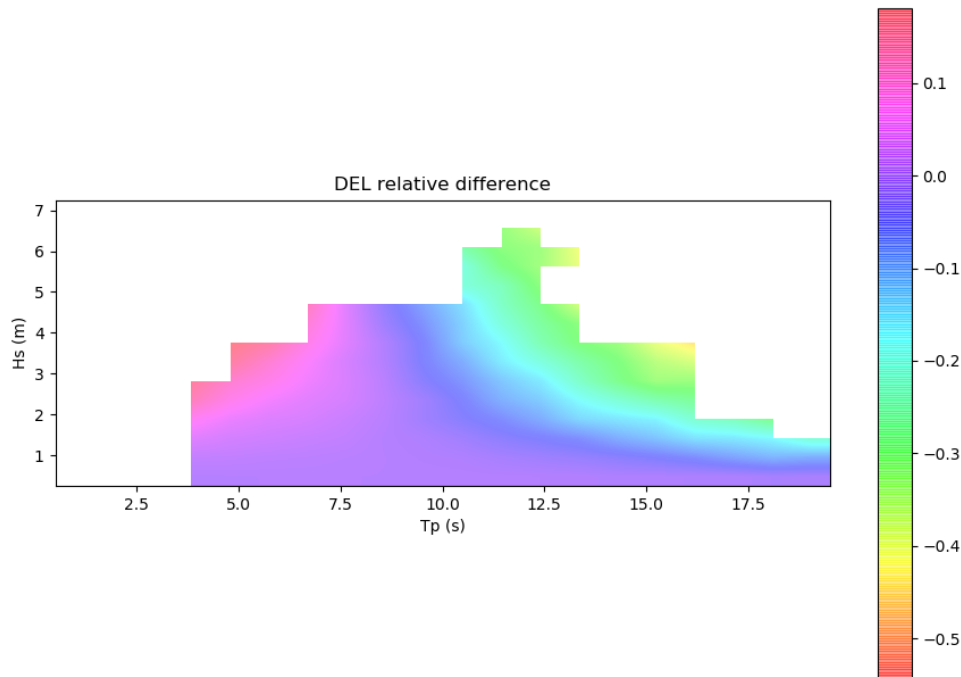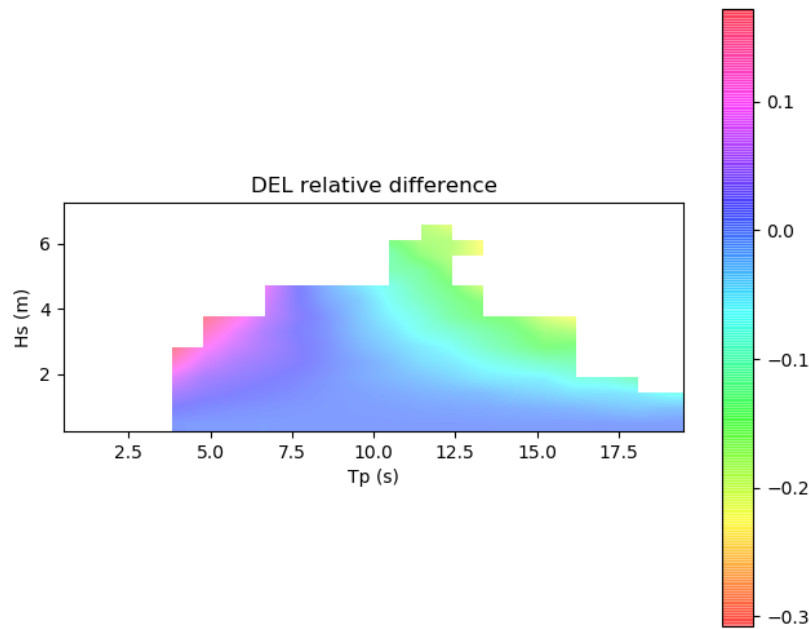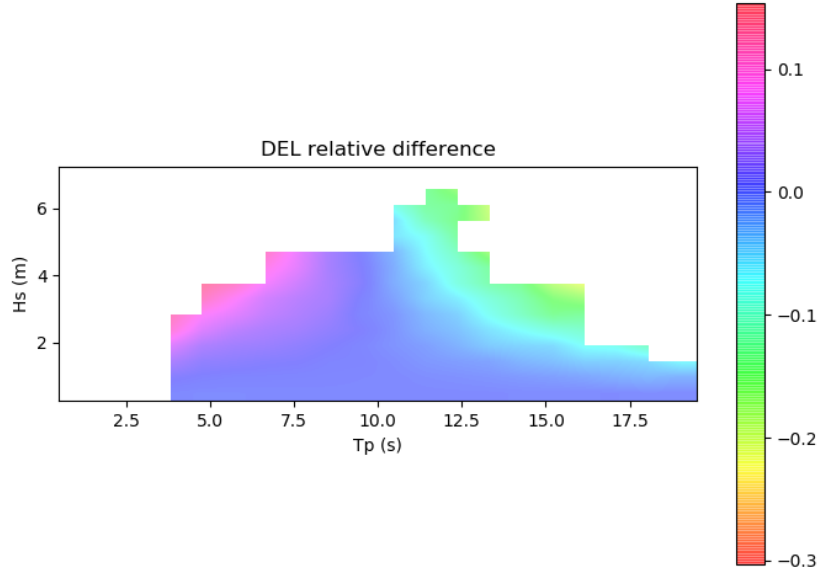
Figure 28: Water depth = 19m. DTU D=8.6m case.
Relative DEL error between MCF and the Potential Flow theory (positive value means MCF produces higher DEL).

4.1.4. Other sources of uncertainties

This section is devoted to the quantification of other sources of uncertainties. Only the stretching models have been identified at the time of writing the report.

4.1.4.1. Stretching models

The Airy wave model is known to produce too strong kinematics in the crests of irregular sea states, and a common strategy to control them is to use a stretching model [11.]. Many models have been proposed in the literature (see [12.] for instance), and none of them are consistent with all the potential hypothesis [11.]. All the work of the previous section has been made with the so-called « vertical stretching », consisting in applying the kinematics computed at the free surface on the whole wave crest:

$$V_x(z) = V_x(z = 0) = \sum \frac{a_i k_i g}{\omega} cos(k_i x - \omega_i t + \varphi_i) \ for \ z > 0$$

(note: only the horizontal velocity is given here, but the stretching applies to all kinematics).

Other popular stretching models are the « Wheeler Stretching » (used in Bladed for instance [6.]),

$$V_x(z) = \sum \frac{a_i k_i g}{\omega} \frac{ch\left(k_i d \frac{z+d}{\eta+d}\right)}{ch(k_i d)} cos(k_i x - \omega_i t + \varphi_i)$$

or the « Wheeler+ Stretching » used in Deeplines Wind™ [12.].

38

$$V_x(z) = \sum \frac{a_i k_i g}{\omega} \frac{ch\left(k_i(z+d)\frac{z+\eta_i}{d+\eta}\right)}{ch(k_i d)} cos(k_i x - \omega_i t + \varphi_i)$$

These two models are compared to the Vertical Stretching below, using the MCF loading model and the same DEL maps as presented before, on the Teesside case with a homogeneous diameter. The reference model in these comparisons is thus the MCF combined with the vertical stretching.

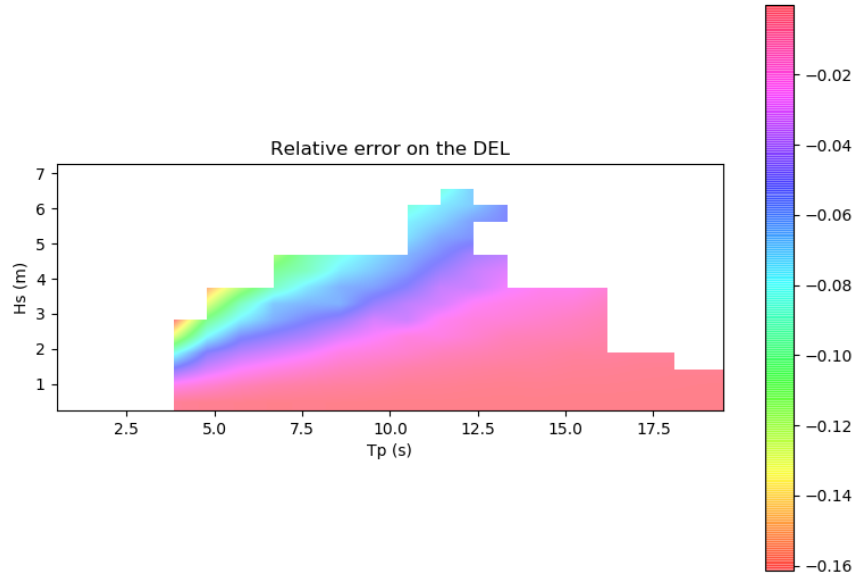
Figure 29: Water depth = 12.5m. Teesside-like homogeneous D=4.6m case.
Relative DEL error between MCF applied with the "Wheeler Stretching" and the "Vertical Stretching"
(negative value means Wheeler produces lower DEL than Vertical stretching).

Figure 30: Water depth = 12.5m. Teesside-like homogeneous D=4.6m case.
Relative DEL error between MCF applied with the "Wheeler+ Stretching" and the "Vertical Stretching"
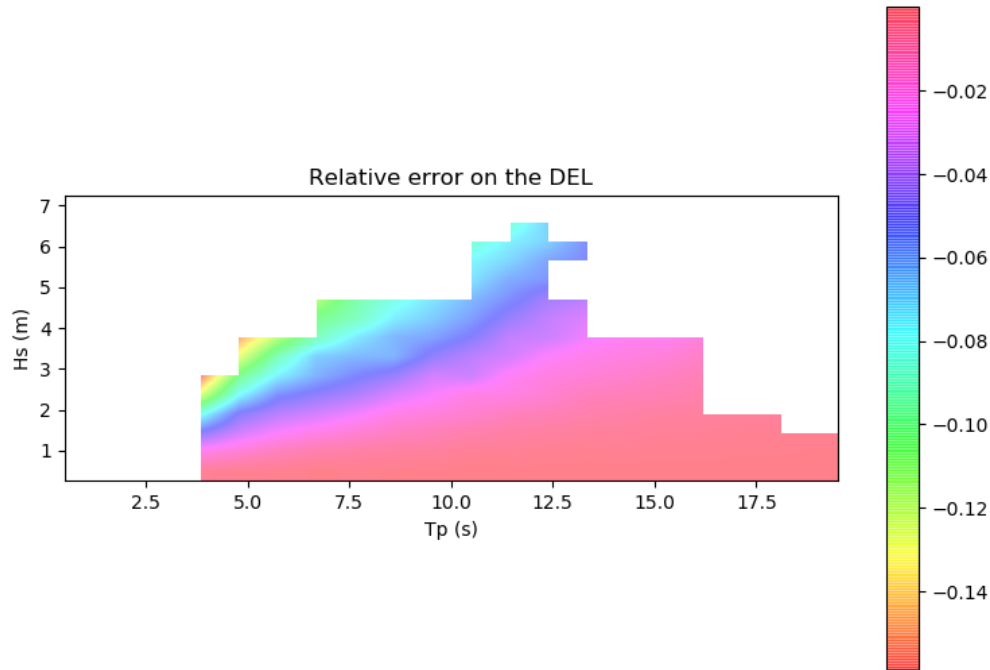*(negative value means Wheeler+ produces lower DEL than Vertical stretching).*

In both cases, the tendency is the same, with the "Wheeler" and "Wheeler +" stretchings predicting lower loads than the Vertical stretching model, from about 1% for the small waves to more than 10% for the short waves associated with Hs larger than 2m. The reduction was expected, given the idea of these 2 models is to reduce the kinematics on the water column to make it fit the maximum kinematics at the free surface instantaneous position, instead of the mean sea level. The reduction is stronger when *Hs* increases, as the perturbation of the kinematics on the water column is more important when the free surface elevation increases. On the most dominant wave conditions at Teesside, the reduction is in the order of 1 to 3% when using "Wheeler" or "Wheeler+" stretching models. The consolidated DEL, accounting for the probability of occurrence of each [Hs;Tp] couple, results in a -7% underestimation of the DEL by the Wheeler (or Wheeler+) stretching model as compared to the vertical stretching model.

4.1.5. Conclusion and recommendations for WP4

This section was devoted to monopile foundations and to the estimation of the uncertainty of the hydrodynamic models regarding the hydrodynamic DEL. Comparisons were done using as "industrial reference" a hydrodynamic model based on Airy irregular waves and the MacCamy & Fuchs correction (MCF) for the load estimations.

Several points have been looked at, for a 2.3MW and a 10MW monopile foundations, using 20 years of the Teesside wave climate as a reference for the case definition. Investigations have been made on the geometrical definition of monopiles and on the loading models, comparing the MCF model with linear and nonlinear Potential Flow methods, regarded as more accurate.

The outputs presented are the difference obtained on the DEL for any [*Hs,Tp*] couple in the Teesside scatter diagram, giving an estimate of the conditions for which the main deviation with the classical engineering model is observed.

The mains conclusions are:

- The MCF method, developed for cylinders of constant diameters but used in the OW industry on piles of variable diameters, can produce both overestimations or underestimations when compared to the Potential Flow method.
    - o For industrial-like geometries, overestimations in the range of 1% to 2% were observed on the global hydrodynamic DEL when the TP diameter crossing the free surface is large. In this case the reference diameter used for evaluation of hydro loads with MCF is equal to the maximum diameter of the geometry tested and this lead to a conservative result.
    - o On the opposite, when the TP is almost submerged and cross the free surface with a thinner diameter, the MCF correction led to underestimations of the global DEL, in the range of 5% to 7%. In this case the reference diameter used for evaluation of hydro loads with MCF is equal to the minimum diameter of the geometry tested.
    - o The ratio between the TP and the pile diameter is an important factor to characterize the level of difference between the MCF and Potential Flow prediction. As this ratio seems to be smaller for large monopile, the 10MW system was less impacted than the 2.3MW system.
- The MCF method applied in the time domain by structural design codes, like Bladed, can produce inaccurate loads due errors in the nonlinear wave forces when compared to the Potential Flow method.
    - o The DEL variation between the 2 methods is low for small waves, as the nonlinear effects stay small.
    - o For short waves, the MCF method overpredicts the DEL up to 10 to 20%, and similar results are found both for the 2.3MW and the 10MW systems.
    - o For long waves it is the opposite: MCF underpredicts the loads, by -30 to -50%. Again similar order of magnitudes are found for the 2.3 and the 10 MW systems
    - o At the end, for a water depth of 12.5m, the global DEL (accounting for all the wave conditions) is underestimated by the MCF model by 13 to 14% when compared to the potential flow.
    - o Moving the water depth from 12.5m (Teesside mean value) to 19m (Teesside upper value) does not affect the tendency but affects the order of magnitude: the MCF model underestimates by only 1.2% the global DEL predicted by the Potential Flow theory. Interestingly, the water depth seems to be more important than the pile diameter in such global comparisons.
- The influence of Stretching models has been briefly analyzed, comparing the Vertical Stretching to the popular Wheeler and Wheeler+ stretching models. These last ones seem to produce lower DEL than the vertical stretching model, by -1% (small wave heights) to -10% (short waves with *Hs*>=2m). Accounting for all wave conditions led to 7% reduction in the DEL when using the Wheeler stretching model instead of the vertical stretching model.

The 3 uncertainties have comparable effects in terms of magnitude, bringing 1 to 10% differences on the DEL depending on the wave case, thus about 5 to 50% differences on the damage itself.

For WP4, it is suggested to investigate:

- The effect of reducing the hydrodynamic DEL by 2%. This value is quite typical of the overestimations observed when industrially using the MCF model for the Teesside mean water level.
- The effect of reducing the hydrodynamic DEL by 10% only for the following wave conditions:
  - *Tp*<8s and *Hs*>1.5m
- The effect of increasing the hydrodynamic DEL by 5%, to cover potentially optimistic hypothesis on the wave kinematics due to stretching model and errors made on the high-frequency loads due to second-order effects.
- Ideally, the DEL relative error maps produced in this study could be used directly to apply increase/decrease of the DEL for each [*Hs*;*Tp*] couples, as significant variations can be found depending on the wave height and wave period.

References of the section 4.1

[1.] Wind Europe (2021). "Offshore Wind in Europe. Key Trends and statistics" 2020.

[2.] Katsikogiannis G &Al. (2021). "Environmental lumping for efficient fatigue assessment of large diameter monopile wind turbines". Marine Structures 77 102939.

[3.] Morison J.R & Al (1950). "The force exerted by surface waves on piles". AIME 189, 149-154

[4.] Mac Camy & Fuchs (1954). "Wave forces on piles: a diffraction theory. Beach Erosion" Board office of the chief of engineers. Department of the Army, Corps of engineers. Technical memorandum 69.

[5.] Pierella F., (2018). DIMSELO KPN project. Oral communication.

[6.] DNV-GL (2014). Bladed Theory Manual version 4.6.

[7.] Ramboll (2011). "Teesside Offshore wind farm. Design basis part 2 C2 – Geotechnical and environmental data". A001-WP05-1-DB-RAM-320-0001-C2.

[8.] https://lheea.ec-nantes.fr/valorisation/logiciels-et-brevets/nemoh-presentation

[9.] Kim MH and Yue DKP (1989). "The complete second-order diffraction solution for an axisymmetric body. Part 1, Monochromatic incident waves". Journal of Fluid Mechanics vol 200 pp235-264.

[10.] Kim MH and Yue DKP (1990). "The complete second-order diffraction solution for an axisymmetric body. Part 2, Bichromatic incident waves and body motions". Journal of Fluid Mechanics vol 211 pp557-593.

[11.] Molin B. (2002). « Hydrodynamique des Structures Offshore ». Ed Technip.

[12.] Sutherland J. (1992). "The Dynamics of Nonlinear Water Wave Groups". PhD Thesis, University of Edimburgh.

[13.] Malik M.G. (2016). "Hydrodynamic modeling effects on fatigue calculation for monopile offshore wind turbines". NTNU Master Theis.

[14.] Haver S. (1980). "Analysis of uncertainties related to the stochastic modelling of ocean waves". NTNU PhD Thesis.

Acknowledgements

4.2. Drag coefficient uncertainty for floating wind turbine

4.2.1. Introduction

In this chapter, an evaluation of the drag coefficients on a floating sub-structure in various conditions is presented. The final purpose is to provide an extended range of hydrodynamic coefficients to feed WP4 uncertainty analysis.

For that, two types of conditions (fixed body in wave and imposed motions in still water) have been studied for several geometrical sections on an offshore wind floating foundation.

Incoming Regular waves with a fixed floater   *Forced Oscillation in calm water (Sway/Heave/Pitch)*

Pitch example
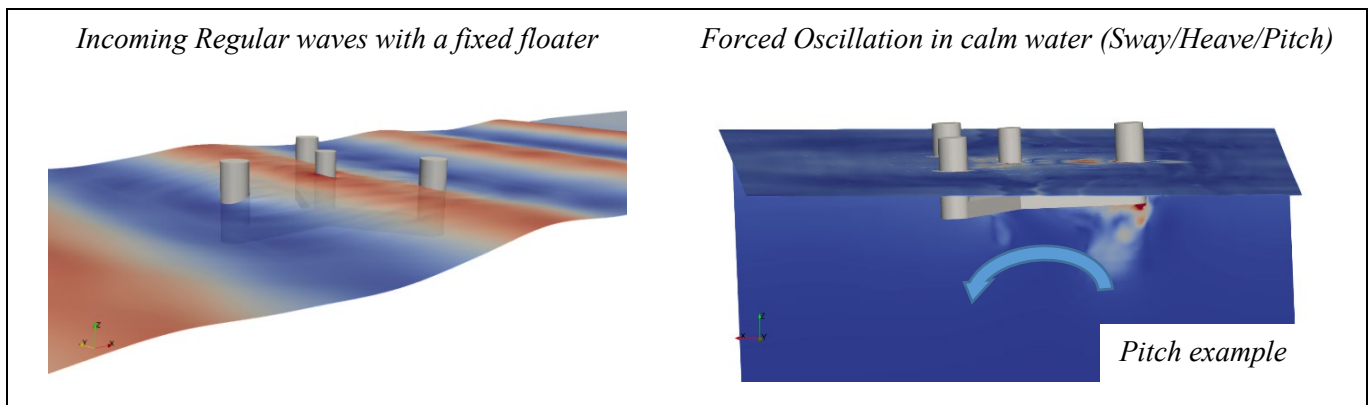
Figure 31 : Illustrations of wave modeling on a fixed floater (left); pitch oscillations on a floater without waves (right).

To carry out the study and be consistent with the case study of the Hiperwind project, the present methodology is applied on the open-source floater of University of Maine. As presented in Figure 32 the floater consists of two different geometries for drag coefficient calibration:

- vertical surface of piercing cylinders,
- horizontal pontoons.
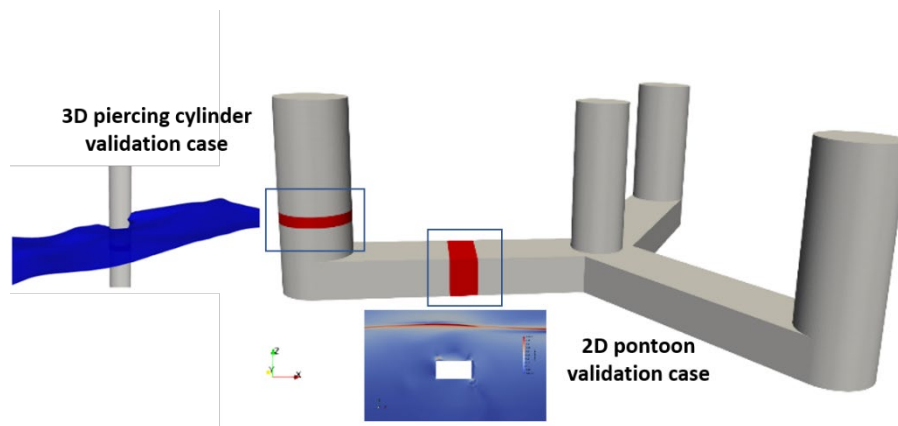
Figure 32 : UMaine Floater sketch with submerged rectangular.

44

To perform the final floater analysis, a step by step methodology is proposed studying first the two different geometries independently:

- step 1: 2D isolated submerged rectangular cylinder analysis with literature comparison,
- step 2: 3D isolated vertical column analysis with literature comparison,
- step 3: Full 3D floater analyses focused on piercing cylinders and submerged rectangular cylinders sections.

The hydrodynamic coefficients are obtained thanks to a Numerical Wave Tank (NWT) set up. Based on the Least Square method, a comparison between CFD efforts and the Morison's empirical formulation is done. [1] has already proposed this method to extract hydrodynamic coefficients experimentally obtained based on Morison's empirical formulation. [2] proposes a similar method replacing the experimental results with CFD forces.

This method is then applied in the final floater geometry configuration. Two different CFD codes have been used to assess the uncertainty coming from high fidelity tools: OpenFOAM® used by IFPEN and neptune_cfd used by EDF R&D.

4.2.2. CFD simulations tools

4.2.2.1. neptune_cfd Immersed Boundary model

The multiphase solver of SALOME_CFD, neptune_cfd, is developed in the framework of the NEPTUNE project (EDF, CEA, Framatome, IRSN). Navier-Stokes equations are solved for:

- 2D, 2D axisymmetric and 3D two-phase flows,
- steady or unsteady,
- laminar or turbulent,
- incompressible or compressible,
- adiabatic or not.

It can simulate boiling flows, sprays, droplet-laden flows, vapor condensation at the wall or on a free-surface, flashing, and large interfaces (slug or free surface).

Nowadays, the validation of the models has been realized for a large range of different application cases.

neptune_cfd is a 3D multi-field solver which was specifically developed for nuclear applications, but its field of application is growing with hydraulic, structure-wave interaction or naval applications. It is based on a two-fluid approach with a single pressure [3] [4]. Its objective is the modeling of multi-phase flows by solving a set of 3 equations per field [5] [6].

The discretization follows a 3D full-unstructured finite-volume approach, with a collocated arrangement of all variables. Numerical consistency and precision for diffusive and advective fluxes for non-orthogonal and irregular cells are taken into account through a gradient reconstruction technique. Convective schemes for all variables, except pressure, are centered / upwind schemes. Velocities components can be computed with a full centered scheme. The solver is based on a pressure correction fractional step approach. Gradients are calculated at second order for regular cells and at first order for highly irregular cells.

A set of local balance equations for mass, momentum and energy is written for each phase. These balance equations are obtained by ensemble averaging of the local instantaneous balance equations written for each phase. When the averaging operation is performed, the major part of the information about the interfacial configuration and the microphysics governing the different types of exchanges is lost. Consequently, several closure relations must be supplied for the total number of equations (the balance equations and the closure relations) to be equal to the number of unknown fields. We can distinguish three different types of closure relations: 1) those which express the inter-phase exchanges (interfacial transfer terms), 2) those which express the intra-phase exchanges (molecular and turbulent transfer terms) and 3) those which express the interactions between each phase and the walls (wall transfer terms) [5].

Several turbulence models are available in neptune_cfd to solve all kinds of high-Reynolds multiphase flows. Regarding free surface flows, classical models like k-ε [7] or k-ε "linear production" [3], where available in previous versions. A more advanced Reynolds Stress turbulence Model, namely Rij-ε SSG [8], has been introduced recently to model highly anisotropic turbulence.

neptune_cfd is using inlet/outlet functions and HPC capabilities from the open-source single-phase CFD software code_saturne[1], used as pre-requisites.

4.2.2.1.1 « Large Interface Model » : LIM

Wave-structure interaction scenarios involve interfaces between liquid and air which are generally much larger than the computational cells size: the "large interfaces". Specific models to deal with them were developed and implemented in neptune_cfd: it is the Large Interface Model (LIM) [6].It includes large interface recognition, interfacial transfer of momentum (friction), heat and mass transfer with Direct Contact Condensation (DCC). The LIM takes into account large interfaces which can be smooth, wavy or rough. Regarding the interface recognition, the method implemented in neptune_cfd is based on the gradient of liquid fraction. The first step consists in computing a refined liquid fraction gradient, based on harmonic or anti-harmonic interpolated values of the liquid fraction on the faces between the cells [9]. This refined gradient allows us to detect the cells belonging to the Large Interface (LI). The models – specific LI's closure laws – developed and implemented in neptune_cfd, are written within a three-cell stencil (LI3C) around the large interface position (including the two liquid and vapor neighboring cells located in LI's normal direction). This stencil is used to compute, on both the liquid and gas sides, the distance from the first computational cell to the large interface (Figure 33). Both distances are used in the models written in a wall law-like format. In this manner, only physically relevant values are used by choosing the interface side, where the phase is not residual and the effect of the LI's position with respect to the mesh is limited.
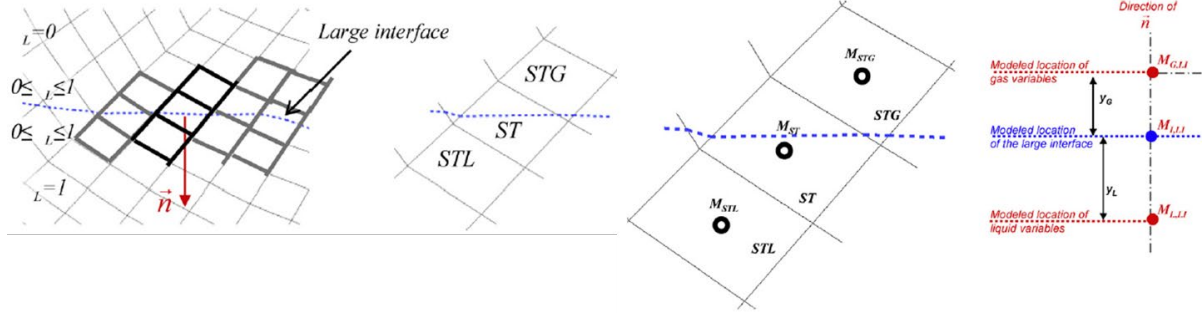
---

[1] www.code-saturne.org

Figure 33 : Illustration of the three-cell packet (LI3C) surrounding the interface.

4.2.2.1.2   Time and space dependent porosity method

Discrete forcing methods aim to strictly ensure the conservation laws at the close vicinity of the interface. The idea is to reshape the cells crossed by the interface and to build specific schemes inside them. The interface is approximated as a plane in each cut-cell. The domain contains the structure, which is considered as a real part of the calculation domain. A recognition function is therefore required to determine the solid location in the cells. The main advantage of these methods lies in the non-explicit representation of the structure. It is then possible to perform calculations on complex solid geometries using Cartesian grids. The major challenge of these methods is to reconstruct the interface properties. In the present method, the whole domain is considered in the framework of a porous media approach, where a time and space-dependent fraction called porosity is 0 in the solid and 1 in the fluid. The fluid-structure interface is consequently represented with a porosity between 0 and 1.

This method involves a non-moving mesh where the body is meshed and defined with a porosity equal to 0 insuring no mass transfer between solid and fluids. Here, the solid motion is tracked thanks to the porosity evolution in a Lagrangian framework. To take into account the solid motion and the presence of an interface in cut-cells, the porosity has to be convected and the momentum balance equations are formulated differently. Based on dedicated geometric parameters, the wall is reconstructed based on interpolations. For low values of porosity (under 10^{-10}), clippings are used to avoid numerical issues. Then, the different two-phase flow numerical models are consequently adapted. This fluid-structure interface tracking method is called time and space dependent porosity method, further details can be found in [10].

4.2.2.1.3   Wave generation and absorption methods

To ensure a correct generation and absorption of the waves, a relaxation technique is used on a portion of the numerical domain. In these zones, a source term is added to the momentum equation to drive the water velocity toward a theoretical propagative regular wave of a given amplitude and period. The theoretical wave is computed through a highly accurate non-linear model based on the stream function theory. In addition, an inlet condition is implemented, to enforce the wave elevation from this same theoretical model. Together, those technique proves to generate an accurate wave field, both in terms of surface elevation and velocity profiles in the bulk of the water, in the absence of the object. The method was also shown to be able to absorb incoming waves, with only a small fraction of energy reflected into the domain.

4.2.2.1.4 Setup

4.2.2.1.4.1 Physical modelling

2 continuous fluids — following parameters are chosen:

- predefined flow: None,
- water field: liquid, continuous,
- air field: gas, continuous.

4.2.2.1.4.2 Thermodynamic properties:
- Water: constant and uniform physical properties, to the values of reference which are 1025kg/m3 (salted water) and 0.001 Pa.s for volumetric mass and dynamic viscosity respectively,
- air: constant and uniform physical properties, to the values of reference which are 1.2 kg/m3 (salted water) and 1.8 10-5 Pa.s for volumetric mass and dynamic viscosity respectively.

4.2.2.1.4.3 Closure model
- Turbulence: $k - \epsilon$ linear production, (also tested in laminar and with R_{ij}),
- interfacial transfer of momentum: Large Interface Model,
- gravity: 9.81 m.s-2.

4.2.2.1.4.4 Initial conditions
- Initial pressure: 1 bar in air and hydrostatic pressure in water,
- free surface at: z = 0.m,
- initial velocities: null.

4.2.2.1.4.5 Boundary conditions
- Top: outlet
  - Reference pressure: 0 bar,
  - volume fraction in case of backflow: gas 1, liquid 0,
- bottom, Side 1, Side 2: wall,
- side 3, Side 4: symmetry.

4.2.2.1.4.6 Wave maker

The wave in generated and enforced along a length of 1.5λ to 2λ depending on the application case, where λ is the wavelength.

4.2.2.1.4.7 Absorber

In the same manner the absorption of the incoming waves is enforced throughout a length of 1.5λ to 2λ. In this zone, the target velocity is (0,0,0)m/s.

4.2.2.1.4.8 Time stepping

Adaptative time step in time and uniform in space:

- Kind of time step: adaptive,
- Initial time step (dtref): 10-4 s,
- Maximum Courant number:
  - Water: 1.0
  - Air: 1.5.

Note that this 1.5 maximum courant for the air was chosen because the air phase, despite not being of prime interest, was often driving the choice of the time-step to lower values than needed to correctly capture the free surface and hydrodynamic effects.

4.2.2.1.4.9 Numerical parameters

Numerical schemes and parameters are standards.

4.2.2.2. OpenFOAM® model

OpenFOAM® (for "Open-source Field Operation And Manipulation") is an open-source software based on executables that use packaged functionality contained within a collection of C++ libraries, as presented in Figure 34. OpenFOAM® is installed with more than 250 pre-built applications divided into 2 categories: solvers, designed to solve a specific problem of fluid mechanics, and utilities, designed to perform tasks that involve data manipulation as pre- and post-processing tasks.
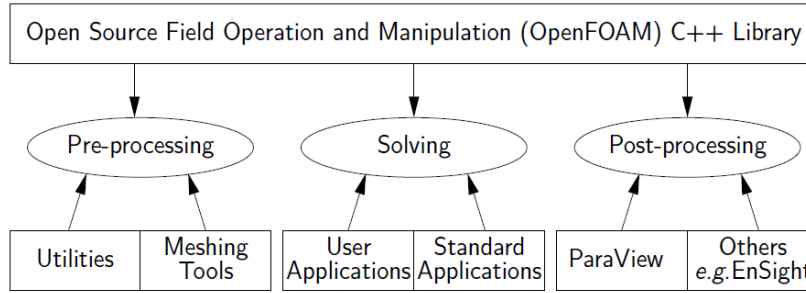

Figure 34:Overview of OpenFOAM® structure (source: https://OpenFOAM®.org/)

Two kind of simulations have been performed in the study: wave propagation with a fixed body and forced motion in still water. Both approaches use the Fluid-Structure Interaction (FSI) solvers with multiphase modeling.

Two fluids, air and water, have to be considered in the computational domain. The fluids are separated by an interface: the free surface. Both air and water are assumed to be incompressible, thus the governing equations for the incompressible fluid are as follows:

$$\frac{\partial u_i}{\partial x_i} = 0$$

$$\frac{\partial \rho u_i}{\partial t} + \frac{\partial \rho u_j u_i}{\partial x_j} - \frac{\partial}{\partial x_j}\left[\mu_{eff}\frac{\partial u_i}{\partial x_j}\right] = \frac{\partial p^*}{\partial x_i} - F_{b,i}$$

Equation 1: Momentum equation for incompressible fluids

where u_i is the fluid velocity vector noted in Cartesian coordinates (i = x,y,z), ρ the fluid density, μ_{eff} the effective dynamic viscosity, p^* is the pressure in excess of the hydrostatic. OpenFOAM® does not directly solve the pressure p but instead $p^* = p - \rho g x$. On the right member of the second equation of Equation 1, F_b is an external body force including the acceleration due to the gravity as follows:

$$F_{b,i} = -g_i x_i \frac{\partial \rho}{\partial x_i}$$

Equation 2: External body force

where the gravitational acceleration vector $\vec{g} = [0; 0; -9.81] \; m/s^2$ and x_i is the position vector.

An additional equation has also to be solved to consider the two phases, air and water. That is done using VOF (Volume of Fluid) approach [10].

An indicator phase function called α is defined as the quantity of water per unit of volume in each cell. This means that if $\alpha = 1$ the cell is full of water, if $\alpha = 0$ the cell is full of air. All the other values concern the air/water interface description. It is straightforward to calculate any of the properties of the fluid at each cell, just by weighting them by the VOF function. For example, the fluid density and the dynamic viscosity of the cell are computed as detailed in Equation 3 and Equation 4:

$$\rho = \alpha \rho_{water} + (1 - \alpha)\rho_{air}$$

Equation 3: Fluid density ρ calculated by a weighted value based on the volume fraction α.

$$\mu_{eff} = \alpha \mu_{water} + (1 - \alpha)\mu_{air} + \rho \nu_t$$

Equation 4: Effective dynamic viscosity μeff (sum of a weighted value based on the volume faction α and a turbulent viscosity ρνt)

Please note the presence of the turbulent kinematic viscosity ν_t. If a laminar solution is sufficiently accurate, ν_t is equal to zero. In the other case, turbulent effects are incorporated in the RANS (Reynolds Average Navier Stokes) equations by solving one or more additional transport equations to yield a value for the turbulent kinematic viscosity ν_t.

In VOF method the interface between air and water is tracked by solving an advection equation of the phase fraction field, namely the interface:

$$\frac{\partial \alpha}{\partial t} + \nabla \cdot (\alpha u) = 0$$

Equation 5: Advection equation of the interface

Two methods are available in OpenFOAM® to solve the equation of the phase fraction field:

- *MULES* (Multidimensional Universal Limiter for Explicit Solution) method used in *interFoam,*
- *isoAdVector* approach used in *interIsoFoam.*

The original and most commonly way to track the interface in OpenFOAM® is done with the MULES approach that is used in the interFoam solver. Special works exist giving the detail of the different approaches. That has not been done in this study [11]. Numerical Wave Tanks (NWT) are basins in which waves are generated, propagated and absorbed. Specific boundary conditions for the velocity, pressure and phase fraction fields are imposed on edges of the tank, as illustrated in Figure 35.
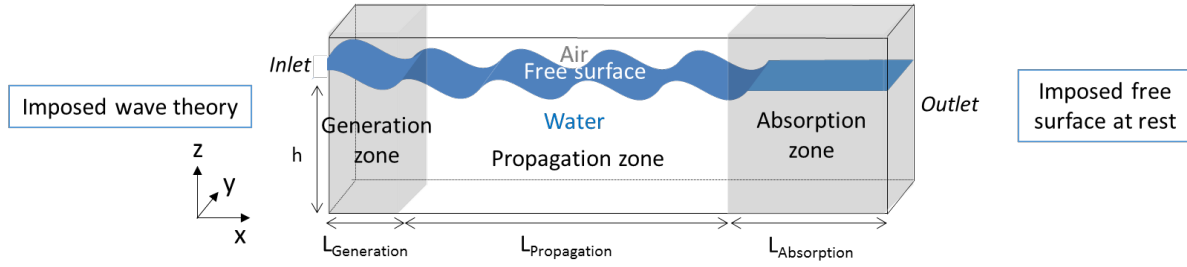
Figure 35: NWT illustrative sketch.

The wave modeling in a NWT with a controlled wave propagation has to consider a minimal damping along the tank and reflection at the outlet and walls. Several solvers exist in OpenFOAM® to model waves accurately as "olaFlow" and "waveFoam". Both are solvers available in OpenFOAM® to generate and absorb waves applying different methods. OlaFlow does not use some generation and absorption zones as waveFoam (Figure 35). However, as illustrated in the literature, OlaFlow is more adapted to shallow water problems. In this study, waveFoam has been chosen to perform the simulations.

The waveFoam library applies the relaxation zone method at the inlet and the outlet of the domain. This library proposed by Jacobsen is based on a generation zone at the inlet for the creation of waves. The absorption zone at the outlet of the NWT controls the wave absorption to avoid reflection. This method is considered passive due to the presence of relaxation zones. In each zone, the velocity and the alpha field are updated at each time step based on a chosen weighted function defined below as represented in Figure 36:

$$\mathbf{u} = \chi \mathbf{u_{computed}} + (1 - \chi)\mathbf{u_{target}}$$

$$\alpha = \chi \alpha_{computed} + (1 - \chi)\alpha_{target}$$

Equation 6 : U and alpha weighted function fields

where u_{target} and α_{target} represent the target values of velocity and alpha fields defined by the selected wave at the inlet, based on wave theory. In the outlet, a null velocity and free surface at rest are imposed. The computed values are the numerical values based on Navier Stokes and VOF equation resolution. Different weighted functions have been introduced by [12]. The most common is the default one: the exponential weight detailed in Equation 7 .
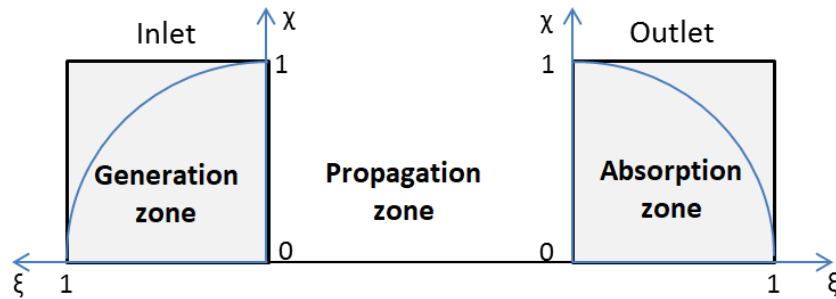

Figure 36: Relaxation zones.

ξ represents the local coordinate system for relaxation zones. χ is assigned such that the target value (u_{target} or α_{target}) gains more weight near the boundary wall (inlet or outlet) away from the propagation zone. Thus, the boundary conditions at the wall are not affected by the computed field between the two relaxation zones.

$$\chi(\xi) = 1 - \frac{\exp\left(\xi^\beta\right) - 1}{\exp\left(1\right) - 1}$$

Equation 7 : exponential weighted function for wave generation and absorption

4.2.3. Extractions of the hydrodynamic coefficients

4.2.3.1. Computation of the hydrodynamic coefficients

From a given discretized wave field and associated load time series, multiple strategies can be employed to extract the different hydrodynamic coefficients, namely the inertia and drag coefficients C_d and C_m that model the loads *via* the so-called strip theory. In its most common formulation, the Morison equation, the strip theory requires the knowledge of the relative velocity and acceleration of an object within a fluid:

$$F_{mx} = \rho V C_{mx} \dot{u}_x + \frac{1}{2} \rho S_x C_d u_x |u|$$

Equation 8 : Morison equation

where x is the direction of the load, u the relative velocity of the object, ρ the fluid density, V the volume of the object (or the part of the object), and S_x the projected surface of the object on a plane normal to the x axis.

From a given load series F_{xi}, extracted from a numerical simulation or an experiment, multiple solutions exist to extract the C_d, C_m for which F_{mx} is the closest as possible to F_{xi} at every instant.

4.2.3.2. L2 method [13]

A commonly used method is to minimize the L_2 norm of the difference between the loads modelled by the Morison equation and the obtained loads, *i.e.* C_d, C_m that minimize:

$$e = \sum_{i=0}^{N} (F_{mx}(t = t_i) - F_{xi})^2$$

Equation 9 : L_2 norm of the difference between the loads modelled by the Morison equation and the obtained loads

The derivation with respect to C_d and C_m of this equation has been done in [13], and is also presented in [14].

$$C_{Dx,z} = \frac{2}{\rho S_{x,z}} \frac{f_1 f_2 - f_3 f_4}{f_2 f_5 - f_4^2}$$

$$C_{Mx,z} = \frac{2}{\rho V} \frac{(f_3 f_5 - f_1 f_4)}{f_2 f_5 - f_4^2}$$

where

$$f_1 = \sum_i^N F_{x,z}(i) u_{x,z}(i) |u(i)|$$

$$f_2 = \sum_i^N \dot{u}_{x,z}^2$$

$$f_3 = \sum_i^N F_{x,z}(i) \dot{u}_{x,z}$$

$$f_4 = \sum_i^N u_{x,z}(i) |u(i)| \dot{u}_{x,z}$$

$$f_5 = \sum_i^N u_{x,z}(i)^4$$

This method will ensure that, for the selected time window, the Morison load that is obtained is the "best" (in the L_2 sense), to model the numerically or experimentally obtained one. However, this method is prone to a large sensitivity to the phase shift, especially the drag coefficients: for example, during the project, a modification of 2% (relative to the period) of the load phase was shown to yield an increase of the C_d by up to a factor 2.

This L_2 method will be applied in most of the application cases described later. When a relative phase shift was observed, a less sensitive method will be applied to identify the hydrodynamic coefficients which is an extension of the work of [15].

4.2.3.3. Extension of [15] to an "order 3" method.

Another method that also relies on identifying which part of the loads is in phase with $\dot{u}_x$ and which part is in phase with $u_x|u|$ was developed by [15]. We enforce the displacement as $x = a \sin(\omega t)$ and thus $\dot{u} = -a \omega^2 \sin(\omega t)$ and $u|u| = a \omega \cos(\omega t) | a\omega\cos(\omega t)|$

We can approximate the $u|u|$ by its Fourier decomposition at order 3: $u|u| = a^2 \omega^2 (0.849 \cos(\omega t) + 0.169\cos(3\omega t))$, and thus the Morison model of the load becomes:

$$F_{mx} = -\rho V C_{mx} a \omega^2 \sin(\omega t) + \frac{1}{2} \rho S_x C_d a^2 \omega^2 (0.849 \cos(\omega t) + 0.169 \cos(3\omega t))$$

Performing a Fourier decomposition of the obtained loads series: $F_x = F_{xcj} \cos(j\omega t) + F_{xsj} \sin(j\omega t)$ allows one to identify the hydrodynamic coefficients:

$$C_{mx} = -\frac{F_{xs1}}{\rho V a \omega^2}$$

$$C_{dx} = \frac{F_{xc1}}{\frac{0.849}{2} \rho S_x a^2 \omega^2}$$

This is how the method was presented and applied in [15]. However, this application is also prone to a large sensitivity in the phase shift because it relies on the repartition of the load into the sine and the cosine terms. To overcome this limitation, we instead use the other possible identification: we identify the C_d thanks to the 3rd harmonic of the load.

$$C_{dx} = \frac{\sqrt{F_{xc3}^2 + F_{xs3}^2}}{\frac{0.169}{2} \rho S_x a^2 \omega^2}$$

This allows us to identify the C_d without using the phase, to guess the distribution into a sine and cosine part. However, it can only be applied under the hypothesis that the unique contributor to the 3rd order of the loads is the drag. In other word, an object submitted to nonlinear waves is supposed to be outside the range of application of this method. As we will see in sections 4.2.7 and 4.2.8, this "order 3" method will thus only be applied in forced motion cases, where a relative phase shift was observed, mainly with neptune_cfd (roughly 4% of the period), leading to a large discrepancy in terms of drag coefficient (roughly 200%).

Last, we underline that the strip theory ignores the radiation damping, which brings a contribution in $\cos(\omega t)$ in the force distribution presented above. In the case of large sections, this can influence the drag coefficient identification.

4.2.4. Benchmark on 2D submerged rectangular cylinders

The first benchmark step has been done on a rectangular- based submerged rectangular cylinder in 2D. In this benchmark case, the wave force Morison coefficients obtained by CFD with the two different codes are compared to experimental ones obtained by [13]. As detailed in Venugopal experiment, the Morison's equation has been extended to horizontal cylinder efforts and the forces per unit length of the horizontally submerged rectangular cylinder are expressed as:

$$F_x = \frac{1}{2} \rho C_{Dx} D u \sqrt{(u^2 + w^2)} + \rho C_{Mx} A \dot{u}$$

$$F_z = \frac{1}{2} \rho C_{Dz} B w \sqrt{(u^2 + w^2)} + \rho C_{Mz} A \dot{w}$$

Equation 10 : exponential weighted function for wave generation and absorption

where F_X and F_Z are respectively the wave force in horizontal and vertical directions. C_{DX} and C_{DZ} are drag coefficients associated with F_X and F_Z. C_{MX} and C_{MZ} are the horizontal and vertical direction inertia coefficients. D represents the cylinder section depth in the vertical direction. B is the cylinder section width in the horizontal direction and A the cross-sectional area of the cylinder. Finally, u and w are respectively the horizontal and vertical particle velocity. And $\dot{u}$ and $\dot{w}$ correspond to horizontal and vertical particle acceleration.

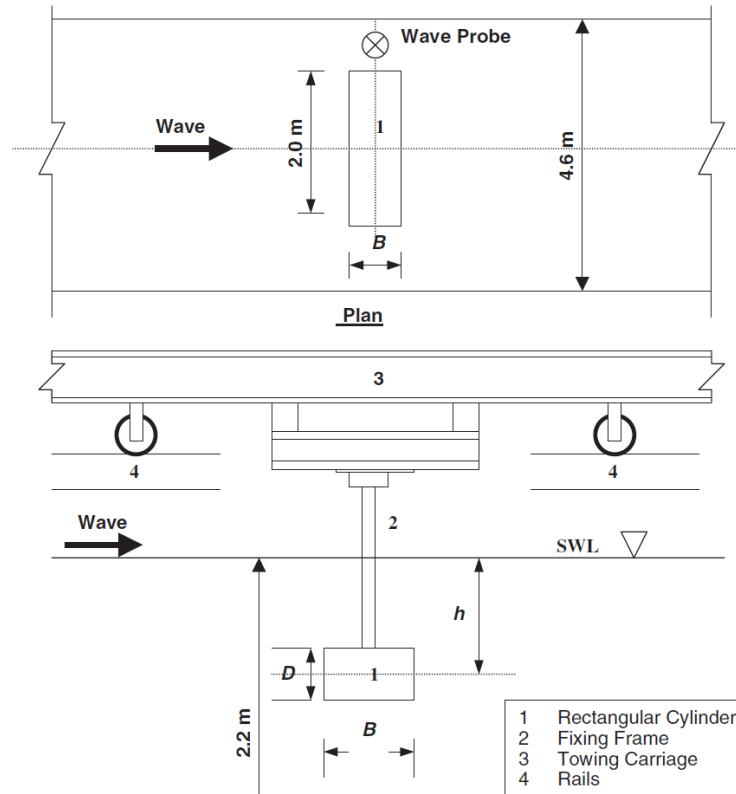## 4.2.4.1. Experimental set up comparison

Figure 37 : Experimental set-up from Venugopal in a towing tank [1].

The UMaine floater rectangular cylinders have an aspect ratio of 0.56. That is close to the 0.5 aspect ratio rectangular cylinder experiments proposed in the experiments from Venugopal. All the dimensions are summarized in Table 4.
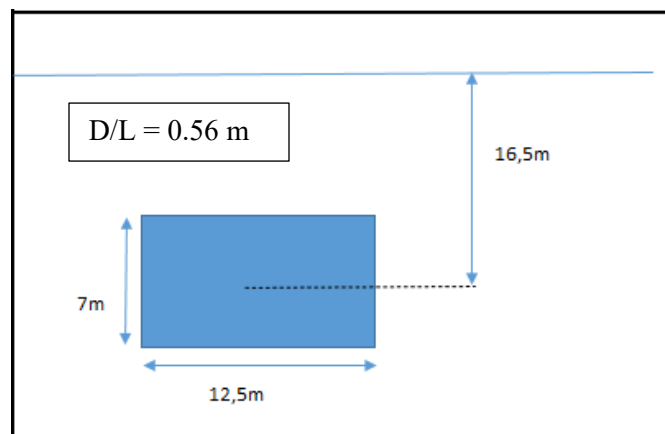

Figure 38 : Hiperwind rectangular cylinder dimensions

Table 4 : Rectangular cylinders dimensions

	UMaine pontoon	Venugopal Experiment
D [m]	7	0,2
L [m]	12,5	0,4
Aspect Ratio	0.56	0.5
Total depth [m]	150	2,2
Submerged depth [m]	16,5	0,47
Depth Ratio	0,11	0,21

Four waves have been selected according to the Keulegan-Carpenter number (KC) range. The coefficients have then directly compared to experiments comparing Cd, Cm = f(KC).

H: height
A: amplitude
T: period
h: water depth
λ: wavelength

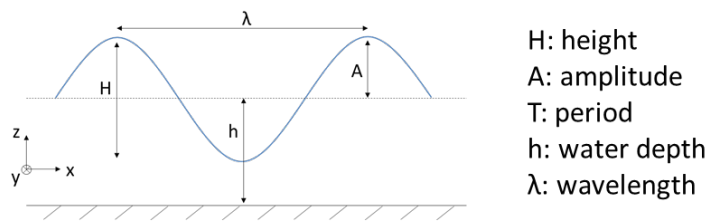Figure 39 : Wave characteristics

Table 5 : Four wave characteristics used in this 2D benchmark

Case	H [m]	T [s]	h [m]	λ [m]	kA (steepness) [-]	KC [-]
Wave 1	0.078	1.3	2.2	2.638	0.030	0.2
Wave 2	0.172	1.9	2.2	5.558	0.031	0.8
Wave 3	0.301	1.9	2.2	5.558	0.053	1.4
Wave 4	0.366	1.9	2.2	5.558	0.065	1.7

Hiperwind reference KC range

Kc = f(Hs / Tp)	8 s	10 s	12 s	15 s
2 m	0,18			
6 m		0,78		
9 m			1,43	1,68

Venugopal et al. experiment equivalence

Kc = f(H / T)	1,3 s	1,9 s
0,078 m	0,20	
0,172 m		0,80
0,301 m		1,40
0,366 m		1,70

4.2.4.2. Meshing and NWT validation

For each tool, OpenFOAM® and neptune_cfd, a meshing preprocessing step has been carried out to set up the NWT with good accuracy. The mesh convergence study is a crucial step to obtain a valid mesh and thus a correct generation, propagation, and absorption of the waves along the tank. Despite particular attention has been paid to this step, only the final meshing configuration is presented in the report. Note that the mesh used by neptune_cfd extend within the interior part of the object, because of the variable porosity method that is employed (porosity field shown on Figure 40).

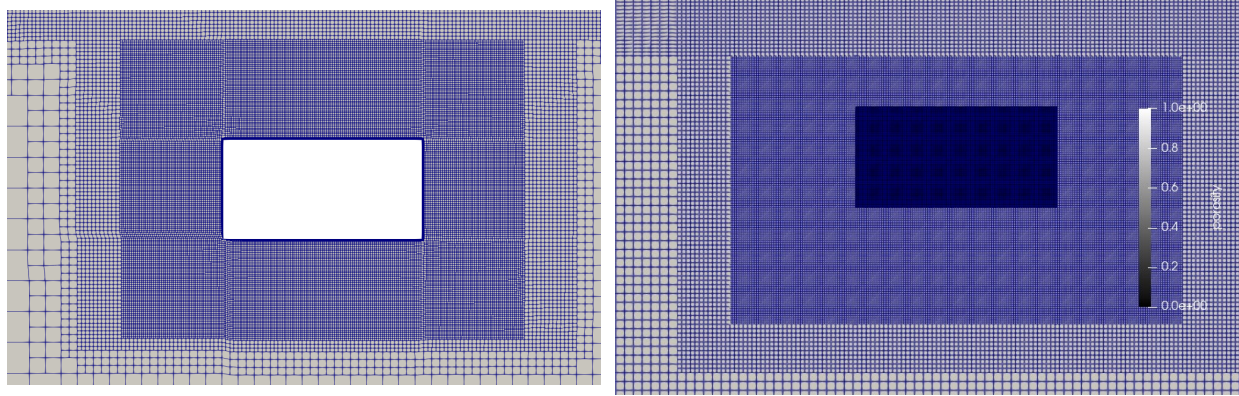*Figure 40 : Different Meshing strategies for each CFD tool (IFPEN on the left, Neptune on the right)*

The global 2D mesh domain counts 245000 cells (Figure 41).
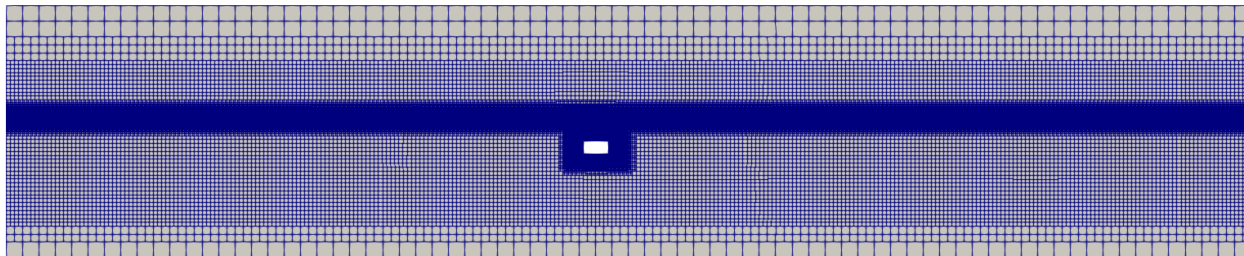

Figure 41 : The global 2D meshing domain

A focus on the base grid and the free surface refinement zone is shown in Figure 42. On IFPEN side, the refinement strategy has been carried out with the inner OpenFOAM® meshing tool *snappyHexMesh*.

57
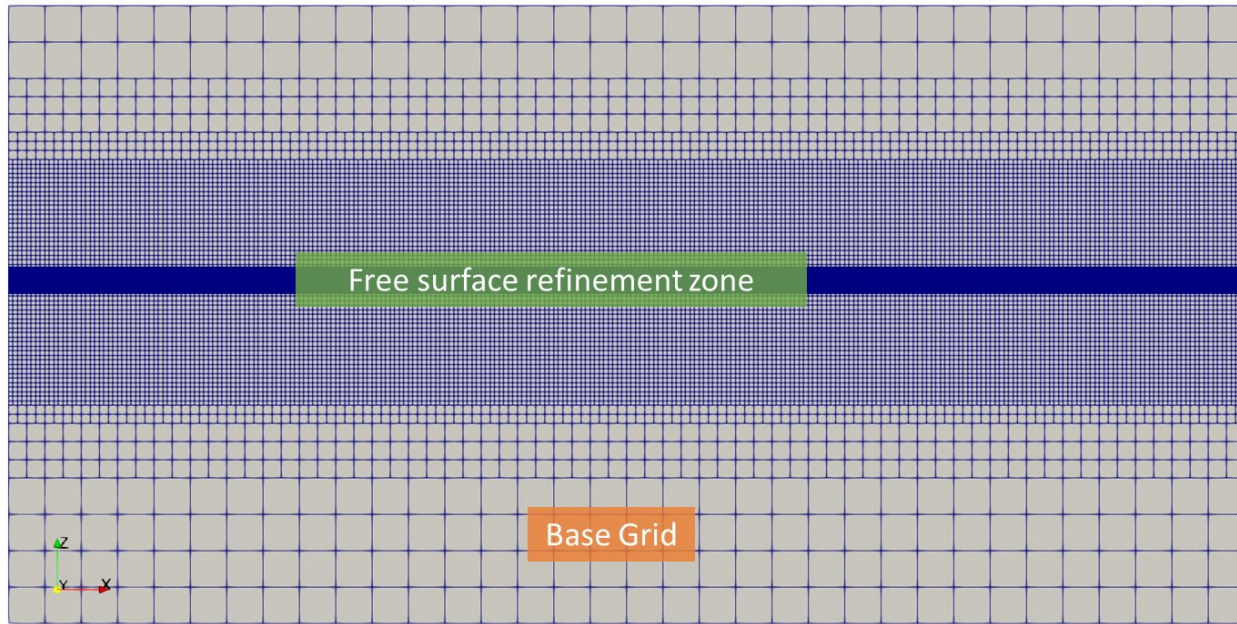
Figure 42 : Refinement strategy example on snappyHexMesh

The implementation of the numerical wave tank and its validation has been based on [2] with a corresponding refinement strategy. Several tests have been done to check the influence of the mesh and domain on the wave elevation before introducing the submerged object. The wave elevation has been calculated at the rectangular cylinder location, but without the cylinder included and compared to the theoretical wave. The reflection and damping of the waves were also studied by plotting the variation of the wave height along the tank. Based on these numerical tests, a set of optimal parameters was determined to propagate the waves in a controlled manner while keeping the computation time reasonable.

Figure 43 : Probes along the NWT to validate the wave propagation

Figure 44 : Example of wave modeling along the basin wave 2. Wave elevation time series for one probe (left). Wave elevation all along the tank (right).

The following numerical settings have been chosen to fit the experiments with a good tradeoff between accuracy and time computing for OpenFOAM® simulations.
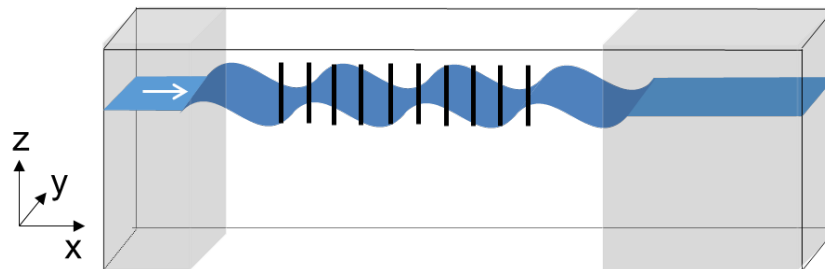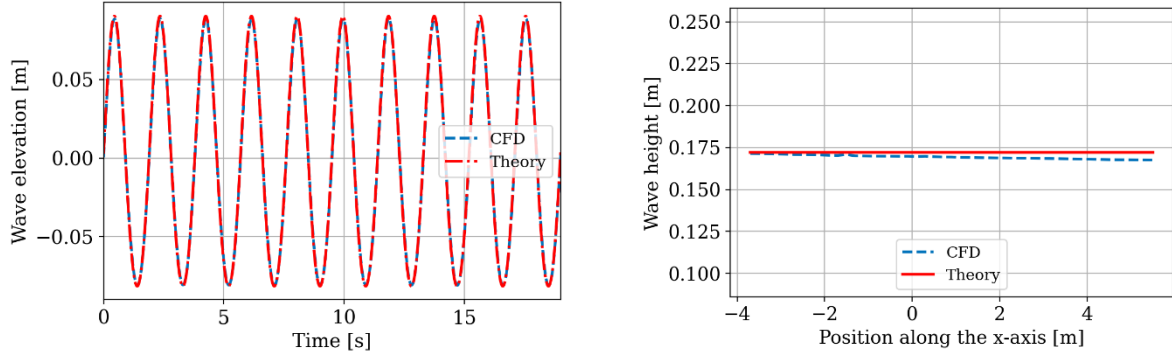
Table 7 : Numerical schemes used for the study in OpenFOAM®

Detail	Term	Numerical scheme
Time derivative terms	ddt(U),ddt(alpha)	Euler
Continuity equation	grad(U)	Gauss linear
Convection term in the momentum equation	div(rhoPhi,U)	Gauss limitedLinearV 1
Diffusion term in the momentum equation	laplacian(gamma,phi)	Gauss linear corrected
Convection term in the VOF equation	div(phi,alpha)	Gauss vanLeer
Compression term in the VOF equation	div(phirb,alpha)	Gauss interfaceCompression

4.2.4.3. Results

The results presented in this section have been obtained using the Least Square method "L2" method presented in 4.2.3.2. As briefly shown Figure 45, this method makes it possible to fit the Morison formulation from CFD loads extracting the corresponding Morison coefficients.
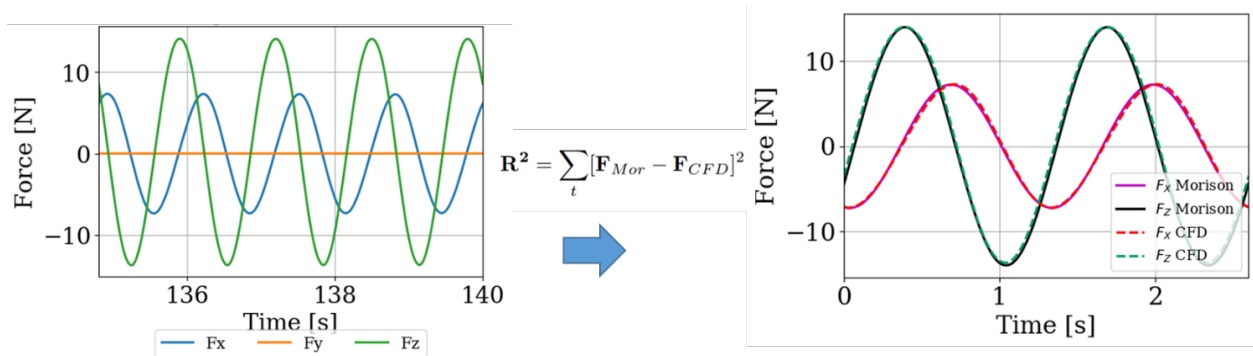

$$\mathbf{R^2} = \sum_t [\mathbf{F}_{Mor} - \mathbf{F}_{CFD}]^2$$

*Figure 45: Example of efforts fitting from CFD to Morison formulation.
Right figure shows the load reconstruction using Morison coefficients*

59

The final coefficient results for the 4 waves are presented in Figure 46. Each graph shows the variation of one-directional coefficient (Cm at the top and Cd at the bottom) at different levels of KC. This figure gives a good overview of the uncertainty obtained on the coefficients experimentally and numerically. Blue circles represent the Venugopal experiments, the remaining symbols corresponding to different reference CFD simulations. The filled circles correspond to neptune_cfd results with two different turbulence models. The diamond and cross shape correspond to OpenFOAM® results. The diamond shape has been fitted with the same method that the circle shape results, while the cross shape only differs by the theoretical velocity taken. A Stokes 3rd order method wave theory has been taken instead of a stream function method as detailed in 4.2.3.2. That shows the uncertainty linked to the theoretical horizontal and vertical velocity method for a given wave.
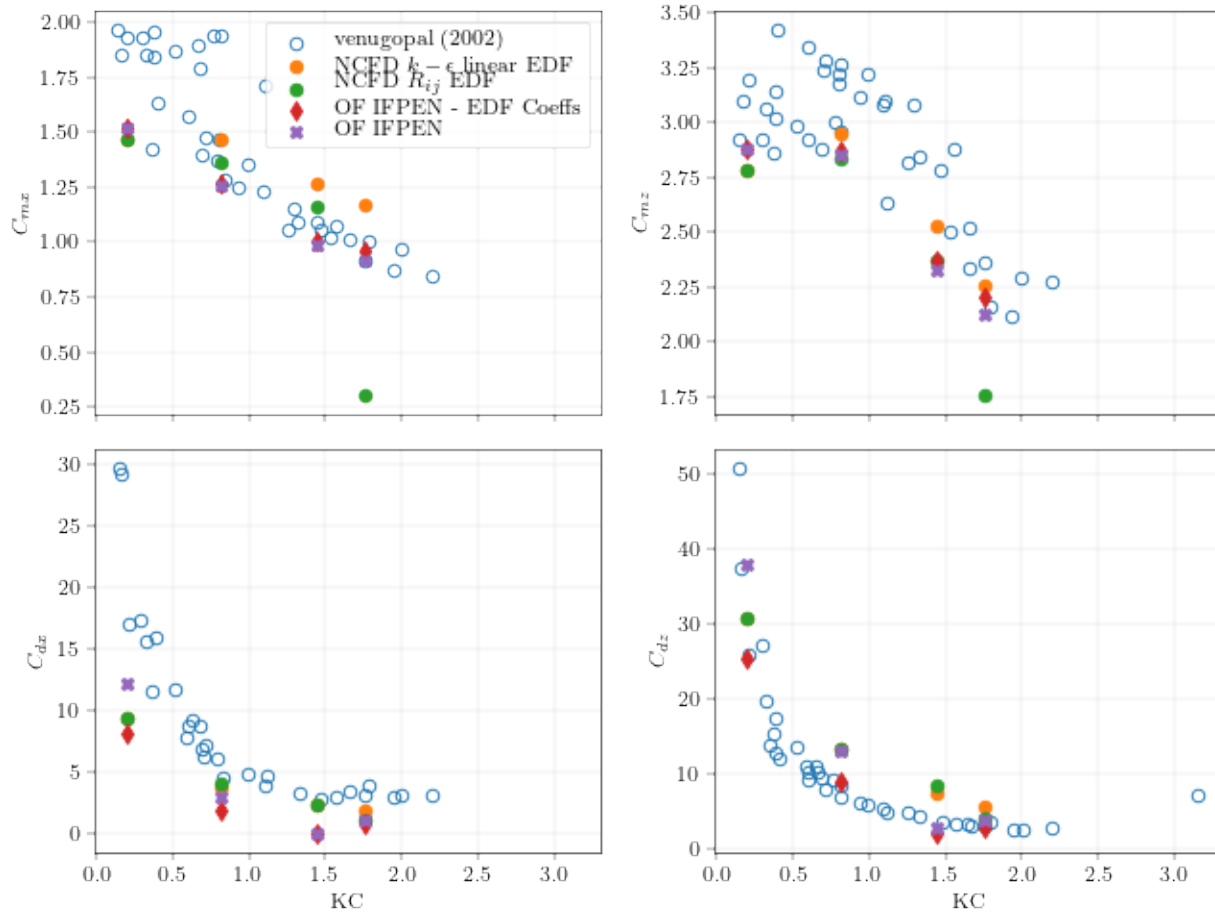
Figure 46 : Neptune_cfd (colored dots), OpenFOAM® (cross and diamonds) results compared to Venugopal's experiments.

Considering the experimental dispersion observed, it can be confirmed that the CFD simulations have a fairly good agreement with experiments. However, a high sensitivity is observed at KC = 1.4, where a larger variation can be observed depending on the code and the theoretical particle velocity method. At low KCs (0.2 and 0.8), a good agreement is observed between both codes and the experiments. Finally, a relative influence of the turbulence model is observed. To deal with vortex shedding, different turbulence models have been tested on both codes. On IFPEN, "stab kOmegaSST" from Larsen, [16] has been mainly used. On EDF side, two satisfactory models have been tested and shown in the figure, the k-ε linear production model is finally selected and applied for the rest of the present neptune_cfd simulations.

4.2.5. Benchmark on 3D piercing columns

The second benchmark of the surface piercing cylinder reproduces the tests of a constrained cylinder in deep-water waves, based on [17]. As presented in Figure 47, a 0.2 m diameter cylinder has been studied.
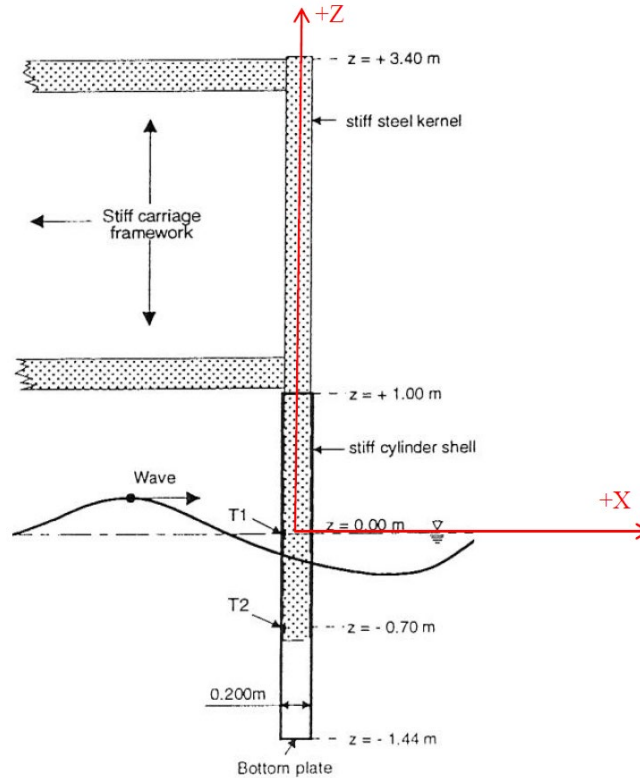
Figure 47 :Surface Piercing Cylinder Experimental set up [17]

The same methodology has been applied for the 3D case. Table 8 presents the 3 different waves selected for this validation step.

Table 8 : Selected waves for 3D case validation

	H [m]	T [s]	h [m]	λ [m]	KC [-]
Wave 1	0.15	1.53	10	3.655	2.36
Wave 2	0.23	1.53	10	3.655	3.61
Wave 3	0.37	1.53	10	3.655	5.81

4.2.5.1. Results

Contrary to the rectangular cylinder case, no coefficients were available in the experimental database, but only the time series of the efforts. As a validation step, time series have been regarded as enough to validate our methodology before modelling the full floater.

Figure 48 illustrate the times series of efforts on the incident wave direction obtained on the cylinder for 3 waves. Satisfactory results have been obtained for this case. Blue dotted lines correspond to the

experiments, gently shared by the NREL [18]. OpenFOAM® results are in orange while green and red ones correspond to neptune_cfd results.
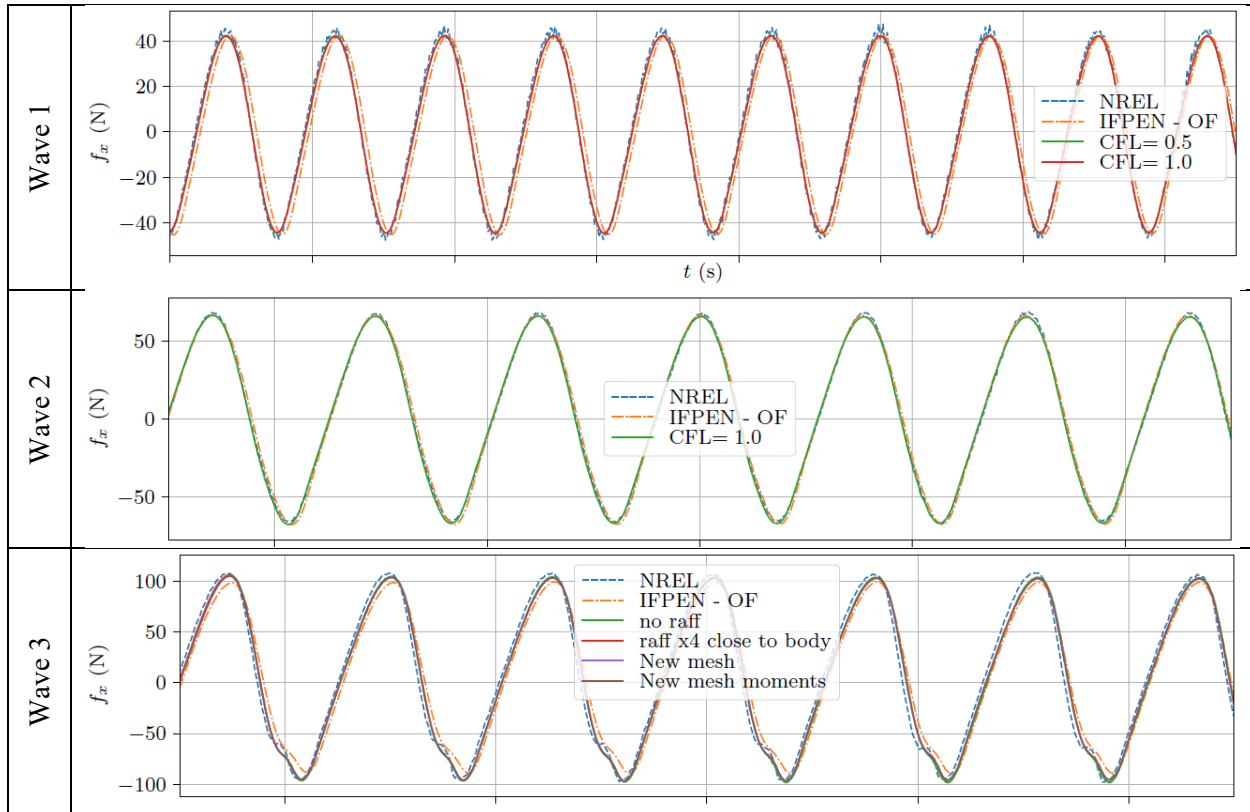
Figure 48 : Efforts on x direction comparison, "NREL" being the experimental result. NREL results represented with a dashed blue line, OpenFoam (IFPEN) in orange. Solid lines are used for the neptune_cfd results. Two different CFL values are tested on wave 1, and different mesh and refinements are used on the wave 3.

4.2.6. Benchmark on the full University of Maine floater

The analysis of the full floater focused on 5 particular zones. From each zone, the coefficients have been extracted. Those 5 zones are illustrated in Figure 49. Before analyzing a large range of conditions, a short comparison between neptune_cfd and OpenFOAM® has been performed on relevant cases: sway motion, heave motions and imposed waves.
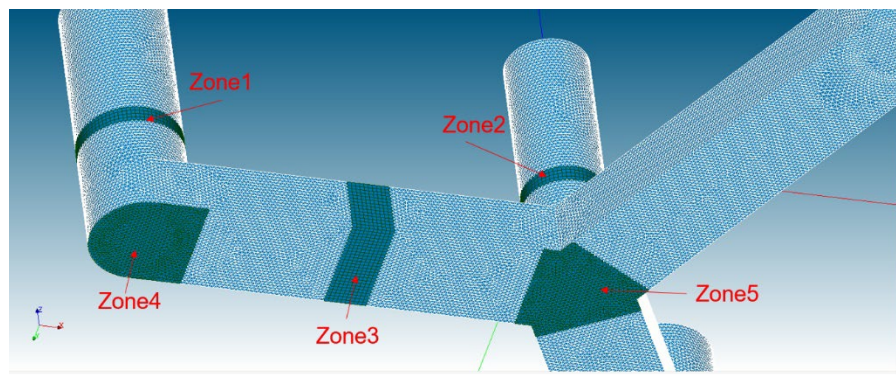
Figure 49 : Zones used to extract the Morison coefficients

Table 9 : Benchmark cases to compare the Morison coefficients on each zone.

Team	#	Name	Wave Conditions			Imposed motion conditions			Horizontal Forces				Vertical Forces	
			H [s]	T [s]	Orientation [deg]	Amplitude [m]	Period [s]	Direction [-]	KC - Zone 1	KC - Zone 2	KC - Zone 3	KC - Zone 4	KC - Zone 5	KC - Zone 3
EDF/IFPEN	A	Benchmark 1	6	10	0				1,18	1,48	0,78	1,39	1,39	1,39
EDF/IFPEN	B	Benchmark 2				3	10	Sway	1,51	1,88	1,51			
EDF/IFPEN	C	Benchmark 3				3	10	Heave				2,69	2,69	2,69

4.2.6.1. Forced sway motion analysis

As a first benchmark case, a sway motion was enforced and simulated with both OpenFOAM® (IFPEN) and neptune_cfd (EDF), with a period of $T = 10s$ and amplitude of $A = 3m$.

First is investigated the hydrodynamic loads on the central column, as well as its decomposition into hydrodynamic coefficients.

Figure 50 : Time series of the hydrodynamic horizontal load applied on an horizontal slice of the central column (zone 2), predicted by OpenFOAM® (IFPEN, dashed line, purple) and neptune_cfd (EDF, solid line, red). Morison contributions (computed from the Neptune_cfd predictions) are also added as dash-dotted lines (mass, drag and mass+drag), for the Neptune_cfd case.

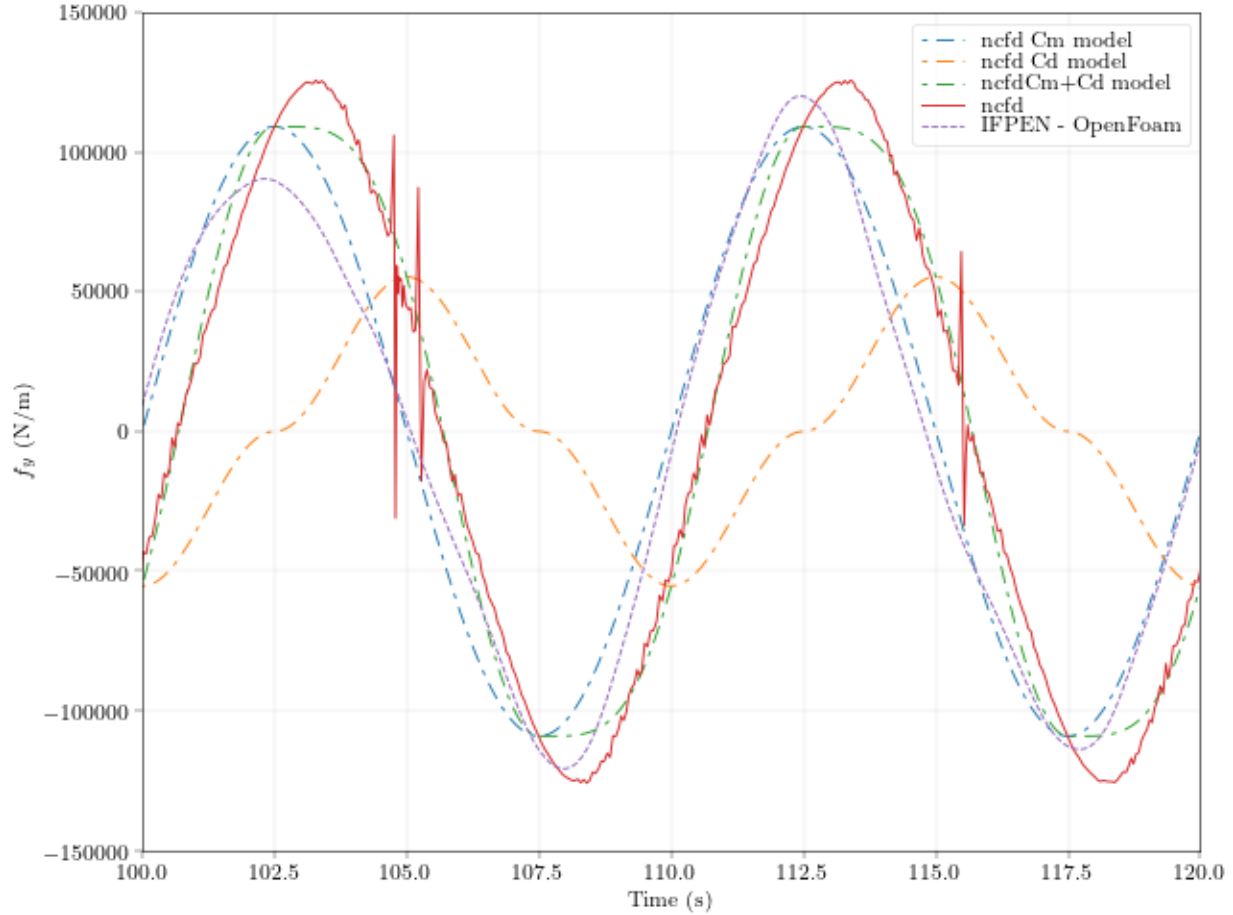Figure 50 shows the different time series of the loads in this first benchmark case, where the floater is forced into a sine sway motion. While the time series of OpenFOAM® and neptune_cfd are in relative agreement concerning the amplitude, a phase shift is denoted. That phase shift influences the computation of the Morison coefficients with the "L_2" method: even the "best" set of coefficients is not appropriate to accurately model the horizontal loads obtained with neptune_cfd. A small phase shift error, compared to the "$\sin(\omega t)$" (phased with the relative acceleration of the object), leads to a large part of the time series being forwarded into the "$\cos(\omega t)|\cos(\omega t)|$" contribution, thus largely overpredicting Cd (3.07). Please note that a slight amplitude variation is observed between 102 and 112s on IFPEN curve, that could come from a wall interaction effect caused by an insufficient damping zone in y axes (radiation/diffraction due to forced oscillations). However, that does not impact too much the present analysis.

Table 10 : Drag and Mass coefficients obtained with the L2 method and the "order 3" identification method (see section 4.2.3.3)

	Cd		Cm	
	L2	Order3	L2	Arai
OpenFOAM®	1.07	1.45	1.07	1.08
Neptune_cfd	3.07	1.36	1.14	1.07

64

However, it was denoted that shifting in time the load series before performing the L2 method could affect the obtained drag coefficient in a significant manner: a shift of 4.5% of the period leads to a reduction of the Cd from 3.07 to 1.04. In this case, the Morison model can fit the "shifted" time series. This very high sensitivity is mainly due to the low contribution of the drag in the total load.

To overcome this effect and obtain a reliable yet accurate drag coefficient, a new method was developed and implemented, based on the norm of the third-order component of the load ("Order 3" method), and thus not relying on the phase of the obtained series. With this method, the obtained drag coefficient is retrieved at a value closer to the expectations and the drag coefficients extracted from OpenFOAM® and neptune_cfd are in agreement (1.36 and 1.45 respectively).

Note that a high frequency is perturbating the neptune_cfd signal, which is linked to the cell shift of the porosity field, thus leading to increased difficulty to retrieve the object faces at some time steps. The obtained hydrodynamic coefficients are, however, relatively close as the high frequencies are somehow ignored and filtered out by the identification processes, with both methods. For this reason, a high frequency filter is applied on the temporal series of efforts obtained with neptune_cfd, and only those filtered temporal series will be shown throughout the rest of the document.

4.2.6.2. Other benchmark cases and summary of results

4.2.6.2.1   Heave benchmark case

The floater is forced into a heave motion of period 10s and amplitude 3. In the same way, the predicted loads are extracted from the simulation on the different zones of interest (presented in Figure 49). Time series of the vertical loads for zone 3 are shown in Figure 51 which exhibit a good agreement between the OpenFOAM® and neptune_cfd predictions.
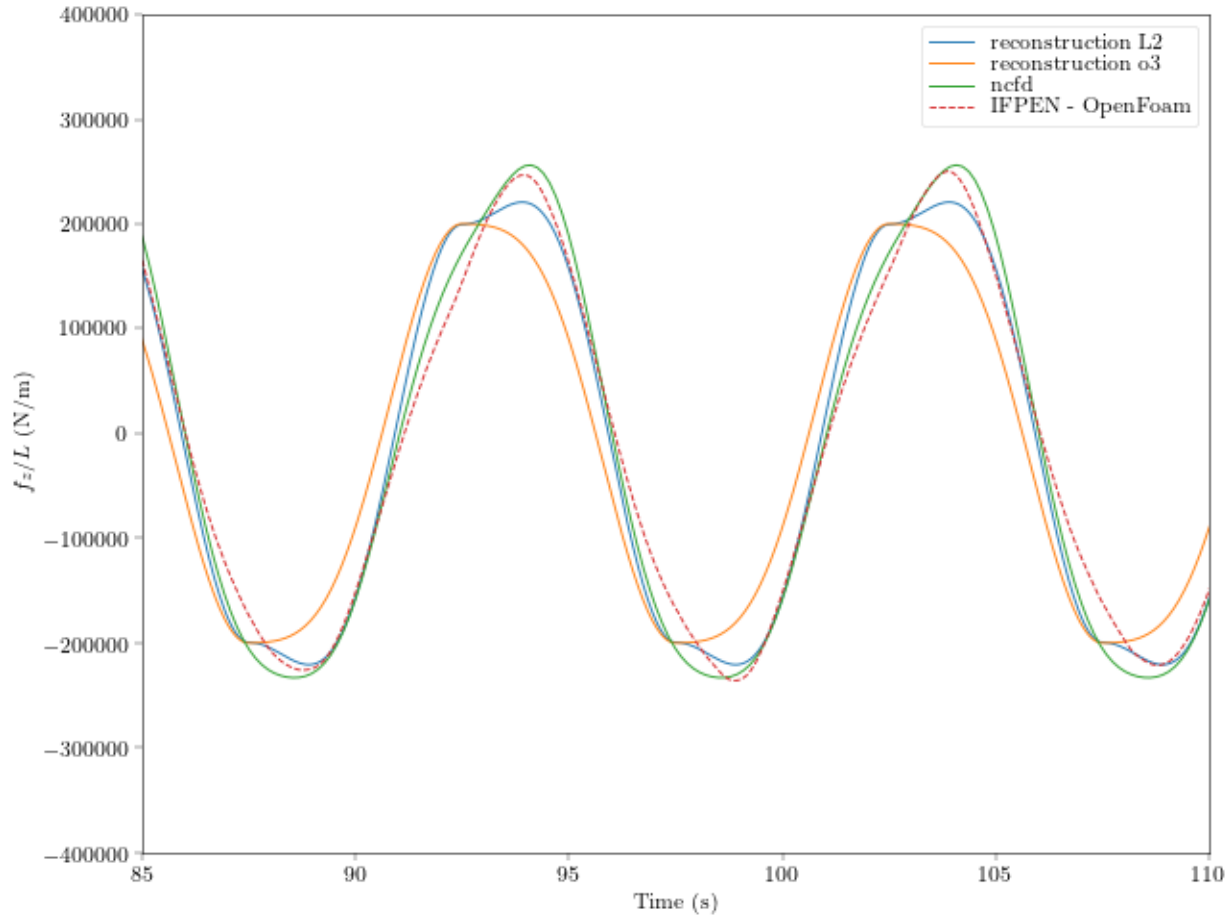
Figure 51: Vertical load series predicted by OpenFOAM® and neptune_cfd on the pontoon (zone 3), for a forced vertical heave motion of amplitude 3m and period 10s. The load is divided by the horizontal length of the considered zone. Reconstruction of the loads series are shown using the values given in Table 11 (Neptune_cfd reconstruction), below

However, while those time series seem relatively consistent, the obtained hydrodynamic coefficients with both the "order 3" and the "L2" method do not give a very satisfactory time series approximation.

Table 11:Drag and Mass coefficients obtained with the L2 method and the "order 3" identification method, for the zone 3

Zone3	Cd		Cm	
	L2	Order3	L2	Arai
OpenFOAM®	6.95	10.46	1.76	1.01
Neptune_cfd	6.93	3.96	1.87	1.88

Concerning the other zones (respectively the base of the front column, zone 4, and the base of the central part, zone 5), the temporal load series are, once again, in quite good agreement.
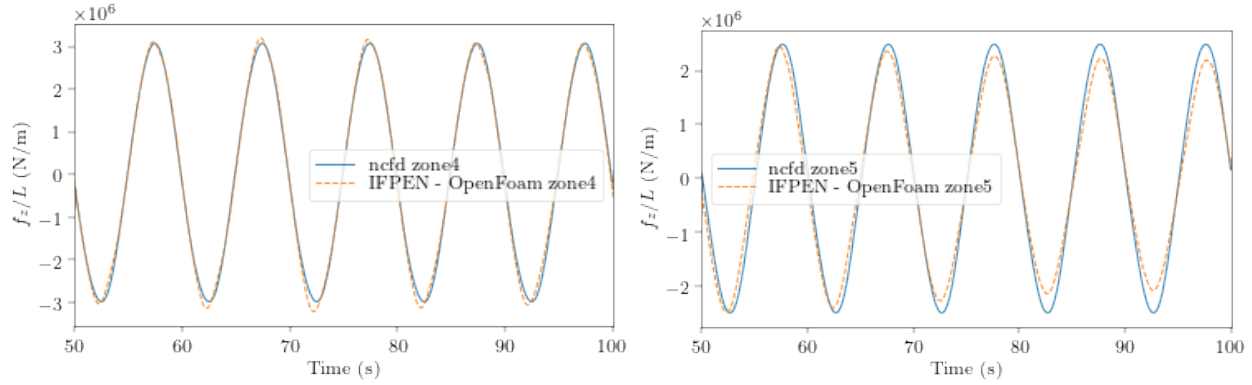
Figure 52: Time series of the hydrodynamic vertical load applied on zones 4 (left) and 5 (right), predicted by OpenFOAM® (IFPEN) and neptune_cfd (EDF).

Note that in this case, a C_m value is not completely meaningful, as we do not have any full "volume" being subjected to a given relative kinematics

Table 12 : Drag coefficients obtained with the L2 method and the "order 3" identification method, for the zone 4 and 5

	Cd Zone 4		Cd Zone 5	
	L2	Order3	L2	Order3
OpenFOAM®	1.15	1.54	0.08	1.43
Neptune_cfd	0.89	0.89	-0.72	0.99

4.2.6.2.2   Incident wave, benchmark case

The same analysis can be performed on the case of incident regular waves of period 10s and height *H*=6m. In this context though, the "order 3" method cannot be applied, because it is expected that not only the drag from the order 1 kinematic generates third order loads, but also the order 3 part of the kinematics directly.

Figure 53: Predicted vertical wave load time series on a portion of the pontoon (zone 3). OpenFOAM®, Neptune_cfd, and Nemoh (no drag hypothesis)

Figure 53 shows the time series for the vertical loads on zone 3. While we can remark a discrepancy in terms of obtained amplitude between OpenFOAM® and neptune_cfd, a relative agreement is found in phasing between the three models. Concerning the amplitude diff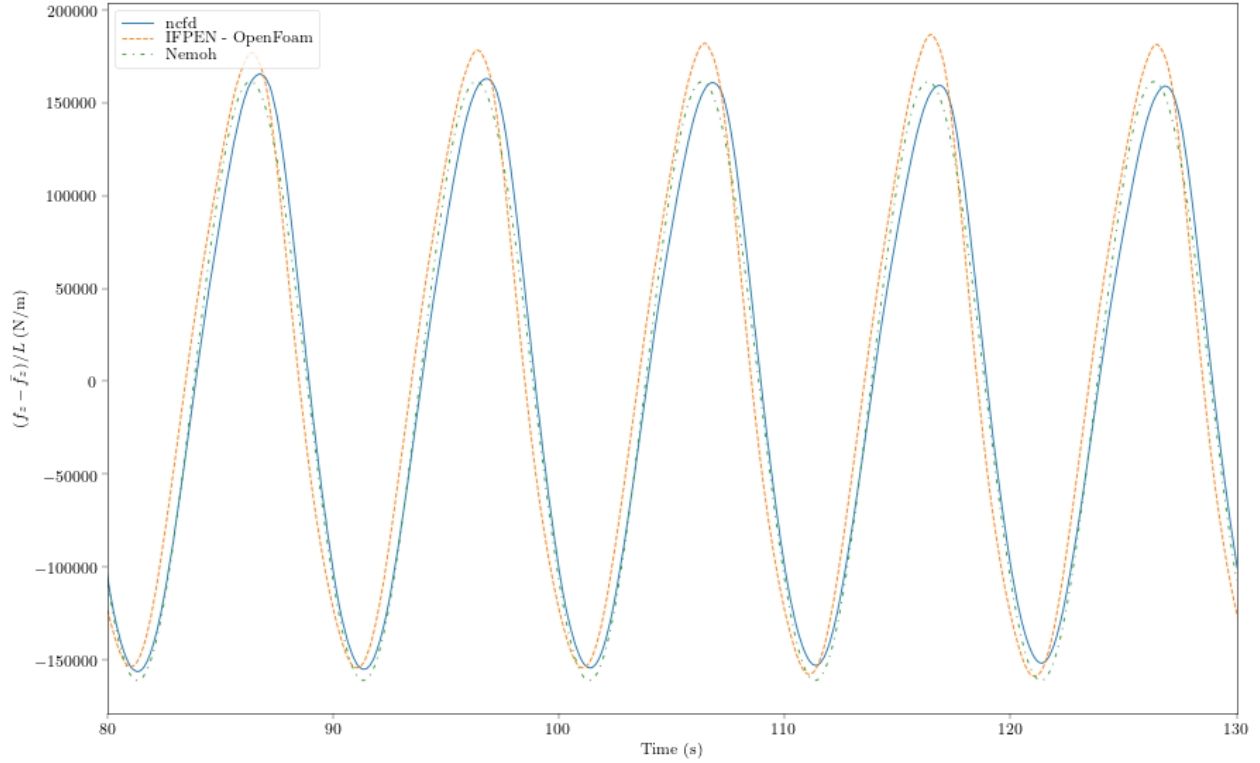erence, the higher maximum efforts observed with OpenFOAM® could come from differences on close body mesh strategies and the different turbulence modeling used by each code. Because Nemoh (BoEM linear potential model) uses the potential hypothesis, no drag can be predicted. The obtained loads are thus completely in phase with the particle acceleration (under the strip theory assumption, which is supposed to be almost applicable given the floater geometry). Because a phase shift can be observed between neptune_cfd and OpenFOAM® predictions, the latter being more in phase with the results of Nemoh, it can be foreseen that a lower drag coefficient will be obtained with OpenFOAM®. In that case, we indeed predict a $C_d = 4.80$ from the OpenFOAM® results and a $C_d = 13.33$ from the neptune_cfd results, using the L2 method. Note that the C_m, generating the large majority of the loads here, are in better agreement, with 3.02 and 2.68 respectively.

The same agreement can be found in the horizontal load series of the two columns of interest.
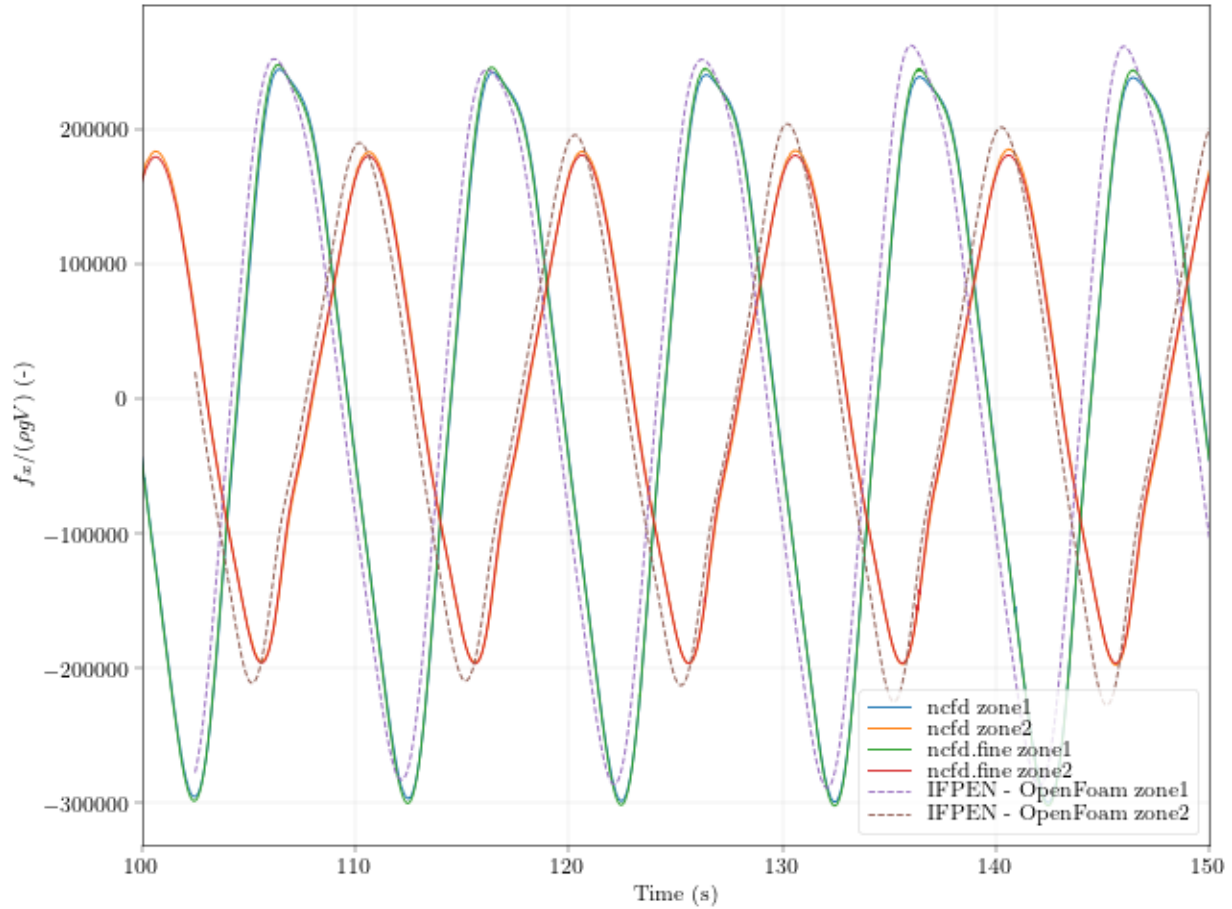
Figure 54 : Predicted horizontal wave load time series on a portion of the central and front columns (zone 1 &2). OpenFOAM®, Neptune_cfd

Table 13 : Drag and Mass coefficients obtained with the L2 for all considered zones in the benchmark case, incident wave of period 10s and wave heights of 6m.

	Zone 1		Zone 2		Zone 3		Zone 4		Zone 5	
	Cmx	Cdx	Cmx	Cdx	Cmz	Cdz	Cmz	Cdz	Cmz	Cdz
OF	2.23	-2.03	2.67	3.03	3.02	4.80	-	6.06	-	-0.89
Ncfd	2.20	5.22	2.23	7.11	2.68	13.33	-	8.36	-	-7.89

Overall, the predicted coefficients by OpenFOAM® and neptune_cfd are in fair agreement. Once again, the drag contribution is of small amplitude compared to the inertia component of the load. For that reason, the dispersion of the obtained drag coefficient is higher, with even some negative - and thus unphysical - coefficients obtained. Note however that because the drag contribution is not of dominant effect, the reconstruction of the load with the Morison equation is not significantly affected.

4.2.6.3. Discussions

The time series of the predicted loads by OpenFOAM® and neptune_cfd, are relatively in agreement. Small discrepancies can however be pointed out, probably due to the different meshes, methods, turbulence models *etc.* that were used. Those small discrepancies can lead to significant differences in terms of computed drag coefficients, showing a large sensitivity of the drag determination to the committed numerical uncertainties. Two different hydrodynamic coefficient identification methods are used. The "order 3" method relies on the correct computation of a term of small relative amplitude (the third-order component of the loads), which can also be prone to errors. On the other hand, the L2 method relies on the correct computation of the phase - which has never proved to exceed 3 to 4% of error - but exhibits a large sensitivity to any phase shift error. This phase shift seems to be higher in the neptune_CFD results and makes its results more sensitive to the coefficient identification method. The OpenFOAM® results sometimes exhibits low frequencies contributions, which do not seem to affect too much the determination of the hydrodynamic coefficients.

4.2.7. Test matrix and results of drag coefficient

Once the benchmark analysis done, each partner has carried out the following cases presented in Table 14. That is representative of a basin test campaign test matrix used to create an extended data base of Cds at different KC levels.

Table 14 : Complete test matrix performed with the full floater by IFPEN and EDF

Team	#	Wave Conditions				Imposed motion conditions			Horizontal Forces			VerticalForces		
		Name	H	T	Direction	Amplitude	Period	Direction	KC -Zone 1	KC - Zone 2	KC - Zone 3	KC - Zone 4	KC - Zone 5	KC - Zone 3
EDF	1	KC1	2	8	0				0,50	0,43	0,18	0,32	0,32	0,32
EDF	2	KC2	4	10	0				1,01	0,99	0,52	0,92	0,92	0,92
EDF	3	KC3	8	12	0				2,01	2,12	1,27	2,26	2,26	2,26
EDF	4	KC4	12	14	0				3,02	3,33	2,15	3,84	3,84	3,84
EDF	5	KC5	15	16	0				3,77	4,29	2,91	5,19	5,19	5,19
IFPEN	7	KC2	4	10	30				1,01	0,99	0,52	0,92	0,92	0,92
EDF	11	KC1				1	8	sway	0,50	0,63	0,50	NA		
EDF	12	KC2				2	10	sway	1,01	1,26	1,01			
EDF	13	KC3				4	12	sway	2,01	2,51	2,01			
EDF	14	KC4				6	14	sway	3,02	3,77	3,02			
EDF	16	KC1				1	8	heave	NA			0,90	0,90	0,90
EDF	17	KC1				2	10	heave				1,80	1,80	1,80
EDF	18	KC2				4	12	heave				3,59	3,59	3,59
EDF	19	KC2				6	14	heave				5,39	5,39	5,39
IFPEN	21	KC3				1	8	pitch				0,81	NA	0,41
IFPEN	22	KC4				3	10	pitch				2,43		1,22
IFPEN	23	KC4				6	12	pitch				4,86	NA	2,43
IFPEN	24	KC5				8	14	pitch				6,46		3,23
IFPEN	25	KC5				10	16	pitch				8,07		4,03

4.2.7.1. Horizontal drag coefficients, sway tests.

The different figures (Figure 55, 56, and Figure 57) represent the evolution of the obtained horizontal drag coefficient with the evolution of the Keulegan Carpenter number. The two different methods of coefficients extraction are performed on all considered cases. Only the cases where the body is in enforced sway motion are presented here, which explains the presence of only one IFPEN point (done at the benchmark step).

Figures show in order the extracted coefficients in: zone1 (Figure 55, a slice of the vertical column), zone2 (Figure 56, a slice of the vertical central column), and zone 3 (Figure 57, a slice of the horizontal pontoon).
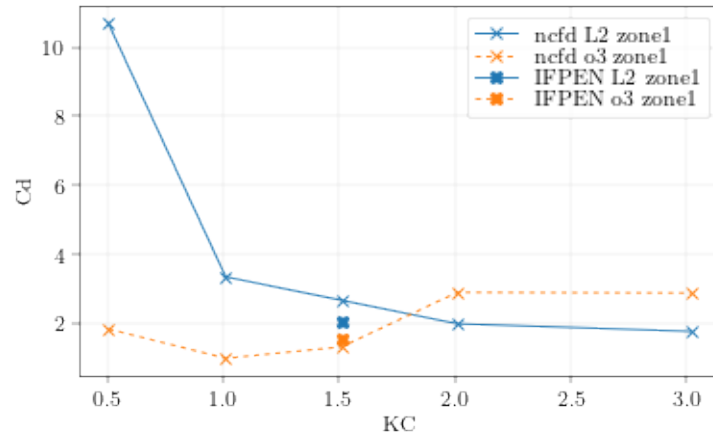

Figure 55: Obtained drag coefficient with two different extraction methods. Sway imposed motions. KC varying
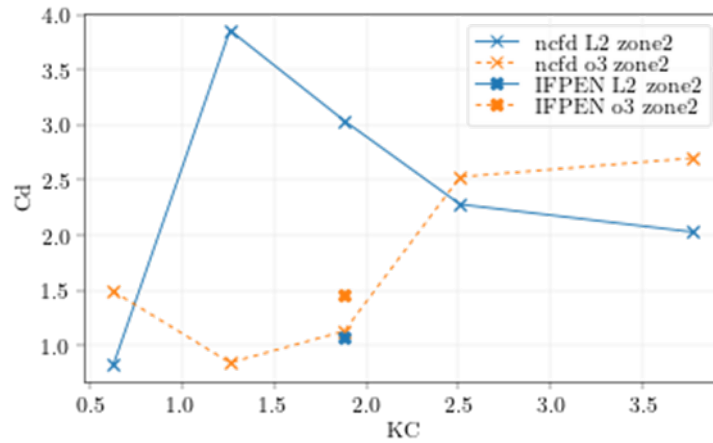

Figure 56: Drag coefficient for zone 2, with two different extraction methods. Sway imposed motions. KC varying.
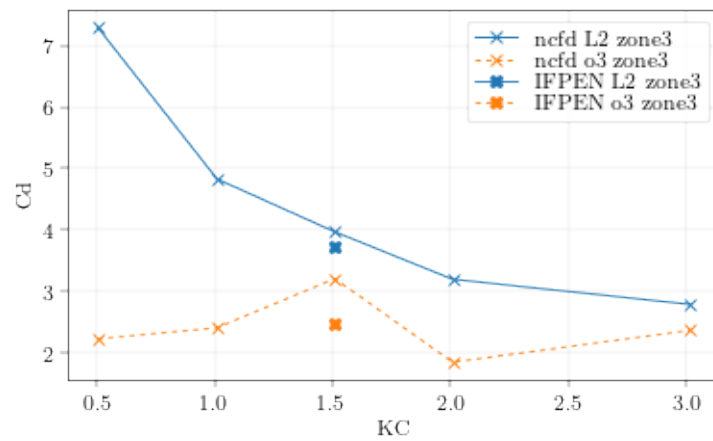

Figure 57: Drag coefficient for zone 3, with two different extraction methods. Sway imposed motions. KC varying

While at larger KC values, the two methods seem to exhibit approximately the same hydrodynamic drag, the sensitivity to the used method is larger for smaller KC values.

For those lower values of KC, the L2 method, relying on the phase shift between the body acceleration and the obtained load series, the reconstruction is not adapted and a higher confidence could be granted to the results of the "order 3" method, even though the latter relies on a contribution of low relative amplitude.

4.2.7.2. Vertical drag coefficients heave + pitch motions

Vertical drag coefficients obtained with the two methods are gathered on the three following figures (Figure 58, 59 and 60) when available. This means that both the results obtained in the pitch forced motion and the heave forced motion will be presented together in the same zones.

Figure 58 : Drag coefficient for zone 3, with two different extraction methods. Heave and pitch imposed motions. KC varying.

First is presented the obtained vertical drag coefficient on the slice of the pontoon (Figure 57, zone 3), then on the base of the external column (Figure 58, zone 4), and the base of the central part of the floater (Figure 59, zone 5). Once again, the "order 3" method as well as the "L2" method results are presented side by side for the heave cases. For the pitch cases, the relative fluid kinematics are more complex, with expressions of the acceleration including some order 2 terms. For that reason, thorough derivation of the equations and extension of this method to the pitch motion would be necessary if one would want to apply it.
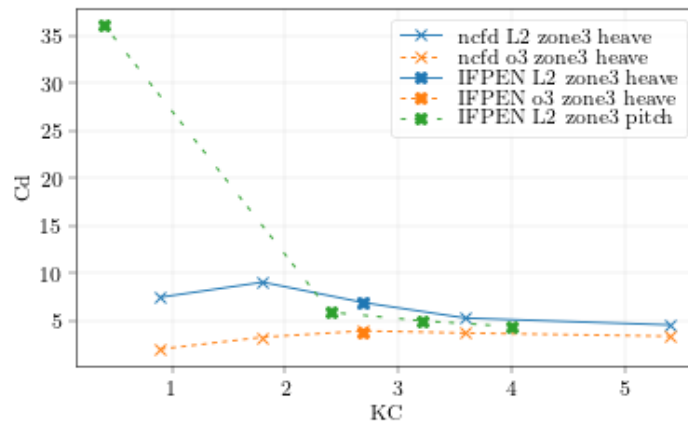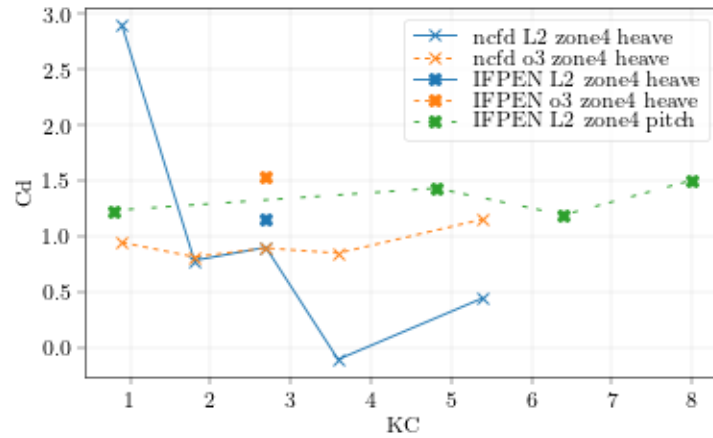
Figure 59 : Drag coefficient for zone 4, with two different extraction methods. Heave and pitch imposed motion. KC varying.

For all the considered cases, the two methods seem to converge on the predicted Cd for the larger values of KC considered. For lower KC values, the L2 method seems to overpredict the drag coefficient, particularly in the pitch motion on zone 3 and the heave motion on zone 4.
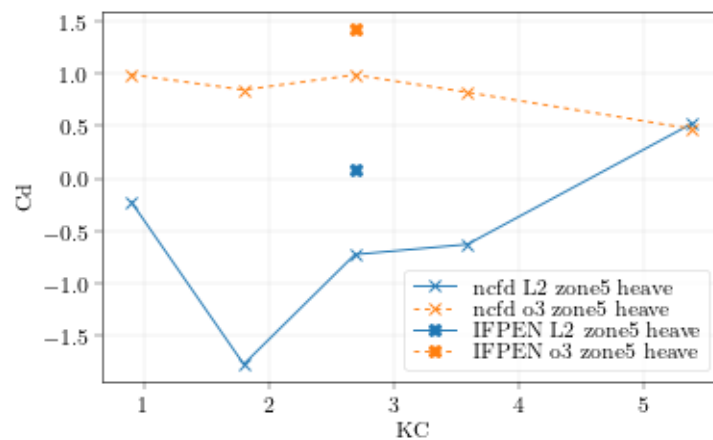

Figure 60 : Obtained drag coefficient for zone 5 with two different extraction methods. Pitch and heave imposed motion. KC varying.

Negative drag coefficients are obtained with the L2 method on the base of the central part of the floater. This is probably due to a physical phase shift emerging from 3D effects and perturbations radiated wave fields from the other part of the floater. Note that, in every considered case, the part in phase with the relative acceleration is always dominant. The drag contribution is thus always difficult to extract and interpret.

4.2.8. Analyses of drag coefficient obtained by different methods and discussion

A relatively important dispersion can be observed depending on the method of computing the coefficients itself. However, it can be noted that larger KC usually leads to better agreement between methods. An error is commited by the CFD model itself, due to the different approximations and models (domain discretization, spatial scheme discretizations, temporal discretization). This error could be roughly estimated to be less than 3~5% and could impact the obtained temporal series both *via* a phase shift or through the load amplitude or shape. In addition, an error might be commited by the post-treatment, within the CFD code, to extrapolate the loads. This is, for example the case of the neptune_cfd porosity method, which can present irregular time series due to a shift in the geometrical definition of delimited area on the floater.

Two methods are considered of coefficient extraction are considered.

-   The "order 3" method will output a coefficient based on the overall shape (third order of the load series) and thus relies on a small contribution to the total load series amplitude. Moreover it is also relatively impacted by the spurious effects on the loads computation. On the other hand an error in phase will not modify the obtained Cd with this method.
-   The "L2" method is, on the contrary not largerly impacted by spurious effects, or an overall error in shape or in amplitude, but relies in background on the phase shift between the velocity acceleration and the obtained loads and is very sensitive to this value.

Given the different obtained load series and their associated small errors, the goal is to match a Morison model, that we consider to be valid for simple shapes in oscillatory or orbital relative fluid displacement. In the case of incident waves, the range of validity is also ensured for small objects compared to the oscillation amplitude of a fluid particle, *i.e.* when the drag and inertia dominates over the diffraction effects (approximately $\frac{\pi D}{\lambda} < 0.5$, where D is the object characteristic dimension, and λ the wavelength). The underlying assumption is that the object does not perturb the fluid kinematics in a significant manner. This hypothesis is of course questionnable in our study, because the flow is 3D and the different part of the full floater radiate/diffract waves that will modify the relative fluid kinematics in the considered zone. As many floating foundations can experience similar issues, it is worth trying to quantify the dispersion obtained on drag coefficients in that situation.

However, for large values of KC (approximately $> 1.5 \rightarrow 3$ depending on the considered case/zone), the two methods seem to converge consistently. Note that this is also the zone where the drag increases, relative to the inertia part of the load (with an infinite KC, the floater would be forced in constant infinite translation/rotation, and thus, no inertia effect would take place).

For lower KC, both the "order 3" and the "L2" method gives valuable information. For example, the reconstruction is always better with the "order 3" method, denoting that either

- 1. A phase shift error is present, largely impacting the results obtained with the "L2" method,

or

- 2. The Morison model is not perfectly able to capture and render the complex effect that occurs in the flow.

The most probable explanation of the obtained results is that both 1. and 2. are at play.

Another method was developed that also tries to suppress the high sensitivity with respect to a phase shift but relies instead on the overall shape of the obtained load series. This method consists in taking the best possible "L2" approximation, for all possible shifts in time of the kinematics. In other words, instead of minimizing the reconstruction error with respect to Cd and Cm to get the best possible approximation, we minimize the L_2 reconstruction error with respect to Cd, Cm, and "time-shift", parameterizing a potential error in phase. While the reconstruction of the temporal series is always relatively consistent with this method, the obtained results are also very dependent on the overall shape, and often lead to negative and thus unphysical Cds.

Possible future studies and extensions could encompass two main axes:

- First and foremost, the convergence studies in both mesh and time discretization could be pushed further, especially in the case of enforced motions, where the relative kinematics are explicitly enforced. The incident wave case adds another source of error in phase shift, related to the wave propagation simulation. This phase shift was shown to play a determinant role in the determination of the hydrodynamic drag. In this incident wave case, it is also possible to simulate the same problem on the same meshes without the body to extract the real kinematics (or phase shift) at the location of the zones.
- Then, and especially in neptune_cfd, a better method of local wave load extraction could be implemented for two main reasons: to remove the spurious effects on the load series, but also to better all types of zones and shapes. The simulations could also be refined by assessing the effect of not using absorber zones in the "x" direction for the sway motion case.

4.2.9. Synthesis on drag uncertainty for design simulations and recommendations for WP4

While the time series of the predicted loads are in good agreement between the two set of simulations, modeling them and reducing them to only two coefficients (Morison model) is a difficult exercise. In the selected conditions (and most of the applicative cases on large objects or sections), the drag is not the dominant part of the load series. That leads to uncertainties when extracting the coefficients from a model results that also contain - in a far lesser amplitude – uncertainties and errors. In other words, changing the value of the drag coefficient does not affect in a significant manner the Morison time series reconstructed.

- For the external column (zone 1), the horizontal C_d is best selected at $C_d = 2.5 \pm 0.5$ for larger values of KC ($KC \geq 2$), with a larger uncertainty for smaller KC ($KC < 2$): $C_d \in [2,5]$.
- For the central column (zone 2), we recommend $Cd \in [2; 2.7]$ for $KC \geq 2.5$ and $C_d \in [1; 4]$ for $KC < 2.5$.
- For the pontoon (zone 3), the horizontal drag coefficient $C_{dx} \in [2; 3]$ and $C_{dx} \in [2; 5]$ for respectively $KC \geq 2$. And $KC < 2$. We recommend a selection for the vertical drag as $C_{dz} \in [3; 6]$ for $KC \geq 2.5$ and $C_{dz} \in [2; 10]$ for $KC < 2.5$.
- For the bottom part of the external column (zone 4): $C_d \in [0.5; 2]$ for the whole range of KC studied.
- For the bottom part of the central volume of the floater (zone 5), the Morison model seems to be at its limits of applicability: we could advise a cautious selection of $C_d \in [0;1.5]$ for $KC < 4$ and $C_d \in [0.3; 0.7]$ for $KC \geq 4$

While those intervals of uncertainties on the drag coefficients might seem of large amplitude, note that their effects on the excitation load amplitudes are relatively contained, mostly due to the relatively low amplitude of the drag component relative to the inertial component (see for example section 4.2.6). This assertion is especially true for low values of KC. However, their effects on the response of the full system might be of significant importance as they are the main contributors of damping effects.

References of section 4.2

[1] V. Venugopal, "Wave force coefficients for horizontally submerged rectangular cylinders," *Ocean Engineering 33,* pp. 1669-1704, 2006.

[2] C. Clément, "Evaluation of Morison approach with CFD modelling on a surface-piercing cylinder towards the investigation of FOWT Hydrodynamics," *Ocean Engineering, Volume 251,* 2022.

[3] S. Mimouni, "A second order turbulence model based on a Reynolds stress approach for two-phase boiling flow. Part 1: Adiabatic to the ASU-annular channel case.," *Nuclear Engineering and Design,* 2009.

[4] J. Delhaye, Thermal-hydraulics of two-phase systems for industrial design and nuclear engineering, Hemisphere and McGraw Hill, 1981.

[5] P. Coste, "A Large Interface Model for two-phase CFD," *Nuclear Engineering and Design, 255, 38-50,* 2013.

[6] M. Ishii, Thermo-fluid Dynamics Theory of two-Phase Flow, Eyrolles: Collection de la direction des Etudes et recherches d'Electricité de France, 1975.

[7] V. Guimet, "A linearized turbulent production in the k-ε model for engineering applications," *Proceedings of the 5th international symposium on engineering turbulence modelling and measurements,* 2002.

[8] P. Coste, "Modelling turbulence and friction around a large interface in a three-dimension two-velocity eulerian code," *Proceedings of NURETH-12,* 2007.

[9] C. Speziale, "Modelling the pressure-strain correlation of turbulence: an invariant dynamical systems approach," *Journal of Fluid Mechanics, 227, 245-272,* 1991.

[10] C. Hirt and D. Nichols, "Methods for Calculating Multi-Dimensional, Transient Free Surface Flows Past Bodies," in *Proc. Of the First International Conference on Numerical Ship Hydrodynamics*, Gaithersburg, Maryland, October 20-23, 1975.

[11] L. Gamet, "Validation of volume-of-fluid OpenFOAM® isoAdvector solvers using single bubble benchmarks," *Computers & Fluids,* 2020.

[12] Jacobsen, "waves2Foam Manual Technical Report," August 2017. [Online]. Available: https://www.researchgate.net/publication/319160515_waves2Foam_Manual.

[13] V. Venugopal, *Hydrodynamic force coefficients for rectangular cylinders in waves and currents,* Glasgow, Scotland: University of Glasgow, 2002.

[14] F. Robaux, *Numerical simulation of wave-body interaction: development of a fully nonlinear potential flow solver and assessment of two local coupling strategies with a CFD solver,* Marseille: Aix-Marseille Université, 2020.

[15] s. Arai, "Forces on and flows around a horizontal rectangular cylinder submerged in regular waves," in *Third International offshore and polar engineering conference*, Singapore, 1993.

[16] B. E. Larsen and D. R. Fuhrman, "Animations comparing surface wave simulations with standard and "stabilized" two-equation turbulence models. https://doi.org/10.11583/DTU.8180708.v1," Technical University of Denmark, 2019. [Online].

[17] C. Stansberg, "Comparing ringing loads from experiments with cylinders of different diameters—an empirical study," *BOSS '97 Conference,* 1997.

[18] A. W. F. Robertson, "OC5 Project Phase I: Validation of Hydrodynamic Loading on a Fixed Cylinder," *Offshore and Polar Engineering Conference (ISOPE 2015),* 2015.

[19] T. Larsen and A. Hansen, "How 2 HAWC2, the user's manual," Risø-R-1597, Roskilde, Denmark, 2019.

[20] M. Hansen, Aerodynamics of wind turbines, Routledge, 2015.

[21] S. Øye, "Dynamic stall simulated as time lag of separation," in *Proceedings of the 4th IEA Symposium on the Aerodynamics of Wind Turbines*, Rome, Italy, 1991.

[22] H. Glauert, A general theory of the autogyro, HM Stationery Office, 1928.

[23] L. Prandtl, "Appendix to Betz's article: Schraubenpropeller mit geringstem energieverlust-mit einem zusatz von L. Prandtl.," *Göttinger Klassiker der Strömungsmechanik Bd,* pp. 3, 89-92, 1919.

[24] G. H. Cottet, Vortex methods: theory and practice, Cambridge: Cambridge university press, 2000.

[25] T. Sebastian, "Characterization of the unsteady aerodynamics of offshore floating wind turbines," *Wind Energy,* pp. 339-352, 2013.

[26] K. S. Boorsma, "Final report of IEA wind task 29 Mexnext (Phase 3)," *Wind Energy,* 2018.

[27] H. Glauert, Airplane propellers, Berlin, Heidelberg.: Springer, 1935, pp. pp. 169-360.

[28] S. Lloyd, "Least squares quantization in PCM," *IEEE Transactions on Information Theory,* vol. 28, no. 2, pp. 129-137, 1982.

[29] D. J. C. MacKay, "Information-Based Objective Functions for Active Data Selection," *Neural Computation,* vol. 4, no. 4, pp. 590-604, 1992.

[30] D. A. Cohn, "Neural Network Exploration Using Optimal Experiment Design," *Neural Networks,* vol. 9, no. 6, pp. 1071-1083, 1996.

[31] Méchitoua, "An unstructured finite volume solver two-phase water/vapor flows modelling based on an elliptic-oriented fractional step method," *Proceedings of NURETH-10,* 2003.

[32] A. Guelfi, "NEPTUNE – A New Software Platform for Advanced Nuclear Thermal-Hydraulics," *Nuclear Science and Engineering, 156, 281-324,* 2007.

[33] B. Launder, "The numerical computation of turbulent flows," *Computer Methods in Applied Mechanics and Engineering, 3, 269-289 ,* 1974.

[34] J. Laviéville, "Numerical modeling of liquid-gas stratified flows using two-phase Eulerian approach," *Proceedings of the 5th International Symposium on Finite Volumes for Complex Applications,* 2008.

[35] P. Coste, "A two-phase CFD approach to the PTS problem evaluated on COSI experiment," *Proceedings of ICONE 16,* 2008.

[36] P. Coste, "A Wall Function-Like Approach for Two-Phase CFD Condensation Modeling of the Pressurized Thermal Shock.," *Proceedings of NURETH-13,* 2009.

[37] W. Benguigui, "A discrete forcing method dedicated to moving bodies in two-phase flow," *International journal for numerical methods in fluids,* 2018.

[38] P. Moriarty and A. Hansen, "AeroDyn theory manual," 2005.

[39] P. Ranjan, D. Bingham and G. Michailidis, "Sequential Experiment Design for Contour Estimation From Complex Computer Codes," *Technometrics,* vol. 50, no. 4, pp. 527-541, 2008.

[40] M. D. McKay, R. J. Beckman and C. W. J., "A Comparison of Three Methods for Selecting Values of Input Variables in the Analysis of Output from a Computer Code," *Technometrics,* vol. 21, no. 2, pp. 239-245, 1979.

[41] C. E. Rasmussen and C. K. I. Williams, Gaussian Processes for Machine Learning, The MIT Press, 2006.

[42] M. O. L. Hansen, J. N. Sørensen, S. Voutsinas, N. Sørensen and H. A. Madsen, "State of the art in wind turbine aerodynamics and aeroelasticity," *Progress in aerospace sciences,* pp. 42(4), 285-330., 2006.

[43] K. Boorsma and J. Schepers, "New MEXICO experiment: Preliminary overview with initial validation," 2014.

[44] Y. Auffray, P. Barbillon and J.-M. Marin, "Maximin design on non hypercube domains and kernel interpolation," *Stat Comput.,* p. 22:703–712, 2012.

[45] C. E. R. Williams and C. K. I., Gaussian Processes for Machine Learning, The MIT Press, 2006.

[46] K. Shaler, B. Anderson, L. A. Martinez-Tossas, E. Branlard and N. Johnson, "Comparison of Free Vortex Wake and BEM Structural Results Against Large Eddy Simulations Results for Highly Flexible Turbines Under Challenging Inflow Conditions.," *Wind Energy Science Discussions,* pp. 1-22, 2022.

[47] T. J. Burton, S. D. N. and E. Bossanyi, Wind energy handbook, John Wiley & Sons, 2011.

5. Aerodynamic loading uncertainty

Fully coupled simulations performed for AEP estimations of wind farm in pre-design stage are commonly carried out using the Blade Element Momentum (BEM) theory [1.]. This widely used aerodynamic method has a low computational cost (1-10h on 1 CPU), enabling it to simulate substantial Design of Experiment (DoE). Nevertheless, some assumptions of BEM theory might be limiting [2.] for the large offshore floating wind turbines which have been recently developed (see. e.g. the IEA15MW OWT [3.] for a representative example). Particularly, the rotor motions induced by the floater might generate specific air flows around the turbine that significantly differ from the BEM validity range (more details are provided in section 5.1.1). Based on an explicit representation of the wake, the vortex methods (detailed in 5.1.2) should be more appropriate to describe the physics in such cases.

In this context, it has been proposed to study the differences in the outputs of BEM and Vortex simulations for two different offshore wind turbines, one fixed (from Teesside wind farm of EDF, east coast of UK) and the other floating (generic wind farm composed of IEA15MW OWT on UMaine semi-submersible floater in South Brittany, west coast of France). To achieve this, fully coupled simulations with DIEGO (EDF), HAWC2 (DTU) and DeepLinesWind™ (IFPEN) using BEM approaches have been performed through a substantial DoE: 300 for the fixed case to achieve a parametric study over 3 environmental variables, and 700 for the floating case for 6 environmental variables. On the other hand, simulations using DeepLinesWind™ coupled with CASTOR, an IFPEN in-house vortex-based aerodynamic model, have been performed to evaluate the uncertainty introduced by the BEM model. As the computational time of vortex approaches is higher (1-10day on 1 GPU), the full DoE could not be fully covered: a multi-fidelity Gaussian process methodology has been applied to iteratively enrich an initial coarse DoE and obtain a final uncertainty meta-model which is optimally reducing the uncertainty given the simulation budget.

5.1. Aerodynamic Theories

5.1.1. Blade Element Momentum

The Blade Element Momentum theory [1.] is the most frequently used model in the industry to predict the performances of Horizontal Axis Wind Turbines (HAWT) and aerodynamic loads acting on blades [4.][5.][6.][7.][8.].

The BEM approach is based on a coupling between two theories. The Moment theory considers a steady homogeneous incompressible flow on a disk representing the area swept by the rotor of a wind turbine. It estimates the decrease of upstream wind speed induced by wake losses, known as the "induction effect", by assuming the thrust and the torque known. In parallel, the Blade Element theory considers finite blades discretized into 2-dimensional airfoil elements. It estimates the thrust and the torque by assuming the induction effect known. Finally, an iterative procedure is employed until the force applied by the wind on the disk corresponds to the force recovered by the rotor.

Nevertheless, the theory is based on strong assumptions and might be corrected for specific usages, such as the tip loss corrections for a finite number of blades, dynamic inflow modeling for unsteady winds, yaw and tilt misalignment modeling, or dynamic stall modeling for unsteady flow around the airfoils. The

existing corrections are sometimes empirical, and based on observations performed on old generations of wind turbines: they might show limitations for large offshore floating wind turbines. In particular, the future highly flexible wind turbine would generate many complex phenomena that violate BEM assumptions [9.], such as swept rotor area deviating from rotor plane, interactions between blades and wake, large rotor motion, non-uniform helical wake, important 3D and dynamic stall effects, etc.

To evaluate the uncertainties of BEM methods, three software have been employed. Each BEM correction has been used according to the recommendations of the software developer (see Table 15).

DLW:
Deeplines Wind$^{\text{TM}}$ is an aero-servo-hydro-elastic dynamic simulation tool using a finite element analysis formulation developed by IFPEN and Principia. It provides a solution to perform fully-coupled dynamic finite element analysis simulations of fixed and floating offshore wind turbines for the turbine components, the floating platform, the dynamic mooring lines, and the power cable. DLW is coupled with aerodynamic libraries to compute the loads along the blades: BEM or Vortex methods can be used.

HAWC2:
Hawc2 [19] is an aero-servo-hydro-elastic dynamic simulation tool developed and maintained by DTU, which is used to calculate wind turbine response in the time domain. Hawc2 can simulate offshore wind turbines on monopile, jacket, or tripod foundations, as well as floating turbines with mooring lines. The structure is represented by beam finite elements using a multibody formulation that allows handling large nonlinearities. Hawc2 uses the BEM approach to compute aerodynamic loads. A comprehensive study on the corrections applied to the BEM method and their effect on aerodynamic loads is available in [10.].

DIEGO:
DIEGO is an aero-servo-hydro-elastic dynamic simulation tool developed to fully model floating or fixed-bottom offshore wind turbines. It assesses the impact of the environment on the turbine loads and motions in time-domain results. The structure is represented through a full finite element approach, the aerodynamic interactions follow the Blade Element Momentum Theory and the hydrodynamic fluid-structure interactions builds on previous EDF tools.

5.1.2. Vortex

5.1.2.1. Overview

Vortex methods offer a variety of possibilities to discretize the geometrical parts of the wind turbine body and the wake. Regarding the discretization of the blade, one can represent the full 3D geometry using vortex panels. Another possibility is to consider the lifting surface approximation, in which the blades are supposed to be infinitely thin plates. It is also possible to consider the lifting line approximation, in which the blades are supposed to be infinitely thin lines. Regarding the wake, one can use panels, filaments, viscous or inviscid vortex particles. For a deeper understanding of such theories, readers can refer to [11.].

In this study, the lifting line theory is used with vortex filaments for both blade and wake discretization. The lifting line approach allows a lower computational cost, and it includes the viscous flow along the blade as it uses aerodynamic polars. The vortex filaments are more accurate than the particles, especially when a single wind turbine is studied. The current vortex filament implementation is purely inviscid and incompressible.

In the lifting-line model, blades are discretized into several vortex filaments, called the "Bound Vortex", where the aerodynamic forces are evaluated. Aerodynamic forces are supposed to be acting at the quarter chord location of the airfoil and act in the normal and tangential directions with respect to the chord. These forces are computed based on the user-provided lift and drag curves (i.e., airfoil polar). The wake is also discretized using vortex filaments. A distinction can be made between the "shed" filaments, which carry the unsteady effects (time variation according to blade rotation), and the "trail" filament, which carries the variation of the circulation along a blade (spatial variation). A schematic representation of the vortex system is given in Figure 61:
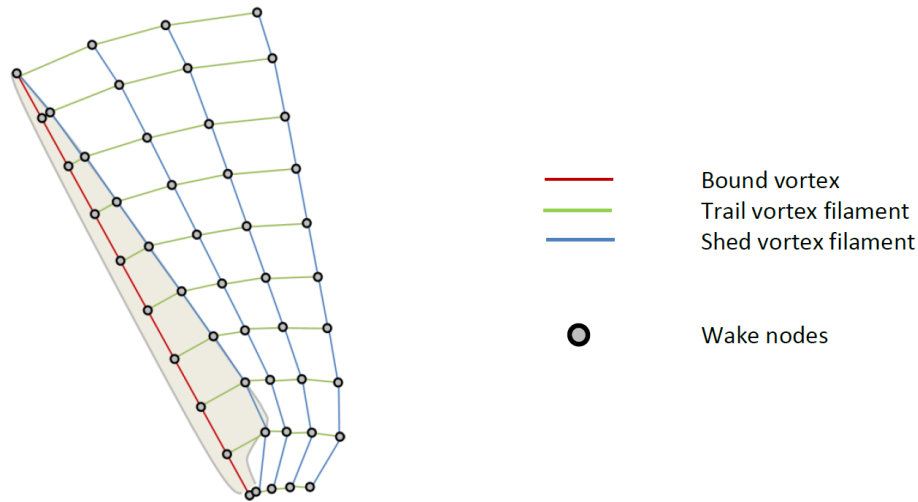

Figure 61: Schematic representation of the vortex system on a blade

At the end of each time step, the vortex filaments belonging to the wake are advected. Both wind velocity and induced velocities (due to the presence of the bound filaments and the shed/trail filaments) are considered so that the wake freely deforms. The wind acting on the blades is also affected. Consequently, the wake has an impact on the blade loads, and the induction zone is intrinsically accounted for. This is the so-called "losses induced by the wake". By decreasing the upstream wind velocity, the entire wake induces losses on the loads, and so on the power production. The induced velocity of a filament is computed by using the Biot and Savart's law.

If the computational cost of such a method is higher than BEM, fewer empirical corrections are needed as most phenomena are inherent to the vortex model. Table 15 lists the phenomena that need to be corrected or not when using the BEM or the Vortex method.

Table 15: Comparison of corrections BEM vs Vortex

Corrections	BEM	Vortex
Tower Shadow	Corrected	Corrected
Dynamic Stall Model	Corrected	Corrected
Root / Tip losses	Corrected	Inherent
Dynamic Inflow	Corrected	Inherent
Skewed wake model	Corrected	Inherent
Turbulent wake state	Corrected	Inherent
Radial induction	Not accounted	Inherent

In this project, the CASTOR IFPEN library is used. CASTOR needs to be coupled with an external solver that provides the necessary information regarding the geometry and kinematics of the solid body (blade element positions, orientations, lengths, and velocities). Given this information, CASTOR can compute the aerodynamic forces acting on the blades and send them back to the external simulator. To this end, CASTOR has been coupled with the DeepLines Wind™ aero-hydro-servo-elastic solver. DeepLines Wind™ can use any turbulent wind files (generated here by HiperSim [19.]) as input to provide the wind velocity at any position and any time. CASTOR has been validated through different benchmarks, as during the IEA TCP Wind Task 29 Mexnext [12.].

5.1.2.2. Optimizing Vortex simulations

To freely transport the wake nodes, not only the free wind speed must be known, but also the velocities induced by each filament. The number of vortex nodes in the wake can be very high. If one considers a typical simulation with a time step equivalent to a hub rotation of 5°, with 15 rotations kept in the wake (length of the filaments) and a discretization of 48 elements per blade for a three-bladed rotor, it leads to approximately 1×10^{11} Biot-Savart law evaluations. The total number of evaluations is massive, thus this part of the solver has been ported to GPU (Graphical Processing Units) using the CUDA programing language. A typical GPU has thousands of cores, and the gain in computational time is substantial.

However, when using a controller, the time step is much lower, leading to a hub rotation of around 0.5° per time step. Considering the same example, the total number of Biot-Savart law evaluations would be about 1×10^{13}, and even the GPU parallelization is not enough. To make the computation cost reasonable, two technics, illustrated in Figure 62, have been applied to reduce the number of filaments:

- Shed merging method: the shed filaments are progressively combined downstream to reach a targeted azimuthal step. Considering the previous simulation, the filaments are emitted every 0.5°. They will be merged in the near wake while being advected. It happens several times until an equivalent maximum azimuthal step below 10° is reached.
- Tip vortex simplification: the trail filaments are combined into 2 filaments per blade (root and tip). As the far wake has less influence on the performances, it is possible to simplify it after a certain distance. Besides the main influence is produced by the tip vortices (so-called "tip losses"), as they contain most of the vorticity. All in all, the far wake can be reduced to tip vortices by merging all the trail filaments into them. During this merging process, the shed filaments are removed from the wake. The transition location is fixed after a certain number of rotations, depending on the operating state of the wind turbine (ie. Tip Speed Ratio). Based on previous studies and the work of [9.], we chose 15 rotations for above-rated conditions, 20 rotations for rated conditions, and 25 rotations for underrated conditions.
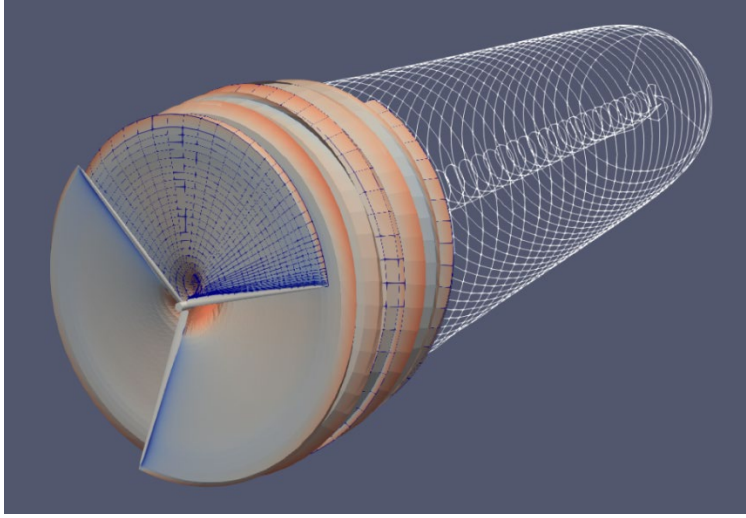
Figure 62: 3D illustration of a "reduced" vortex wake. In the near wake, the size of the filaments (vortex elements) increases progressively ("shed merging" technic). After a transition, only the tip vortices remain to model the far wake. For this illustration, the wake has been frozen.

5.2. General methodology

5.2.1. Design of experiments generation

The objective of the design of experiments (DoE) presented in this report is to optimize the use of the high-fidelity and computationally expensive free vortex wake model (FVW) to both corroborate the BEM models and to quantify the model discrepancy and uncertainties between BEM and FVW models.

As both the BEM and Vortex models require a non-negligible time to simulate a scenario, it is not practically feasible to explore the infinite set of all relevant scenarios through simulations. However, as many physical processes exhibit a continuous behavior (*i.e.* at least differentiable), several regression models exist which can be trained on a set of simulations and then used as a fast-running approximation, or surrogate model, for scenarios not explicitly simulated. That is, we want to approximate the costly simulation function f with an approximative function $\hat{f}$ such that:

$$\hat{y} = \hat{f}(x) \approx y = f(x_{sim}),$$

where $\hat{y}$ is the estimated response of the surrogate model at the input vector $\boldsymbol{x}$. The components of the vector $\boldsymbol{x}$ are the components of the full input vector of the simulator x_{sim} that dominate the response. Hence, $\boldsymbol{x} \in \mathbb{R}^{n_x}, \boldsymbol{x_{sim}} \in \mathbb{R}^{n_{x_{sim}}}$ with $n_x < n_{x_{sim}}$ and where n_x is the number of parameters that are assumed to dominate the response and $n_{x_{sim}}$ is the number of input parameters of the simulator.

It is important that the entire relevant input space $\Omega \subset \mathbb{R}^{n_x}$ is sufficiently explored, while at the same time focusing the simulation effort close to where the simulated responses are most critical. For this report, the relevant quantities of interest are presented and described in section 5.2.2.3, and the objective strategy to optimize the DoE is detailed in general terms in section 5.2.1.1 for BEM simulations and section 5.2.1.2 for vortex simulations.

5.2.1.1. For BEM simulations

The DoE used for the BEM simulations aims at spanning correctly the entire domain Ω. In this context, a space-filling method is appropriate and we decide to use the approach described in [13.]. It consists in creating a sequence of DoEs defined such that it converges to a maximin DoE (i.e. a DoE which maximizes the minimal distance between two points of the DoE). The approach can be summarized as follows:

1. First, N points are randomly drawn in Ω and k points are then randomly selected among these N points. These k points represent the initial DoE.

2. Then, the DoE is sequentially updated as described in Algorithm 1 of [13.]. At each iteration, the following steps are performed:
   a. A pair of points of the current DoE is drawn according to a distribution that favors two close points. Then, one point of this pair is selected with a probability of 1/2.
   b. The selected point x is displaced by drawing a new point from a normal distribution centered at x and thus, a new DoE is proposed.
   c. This proposed DoE is accepted with a probability that depends on the previous DoE and the proposed DoE. This probability favors the proposed DoE if it is better than the previous one in the maximin sense.

3. These updates of the DoE continue until the maximum number of iterations is reached.

We refer to algorithm 1 of [13.] for a more precise description of the approach.

The algorithm is performed by first normalizing every variable in [-1, 1]. Therefore, the DoE obtained at the end is optimal in the maximin sense in the space $[-1, 1]^{n_x}$.

The definition of the domain Ω and the parameters of the DoE used for the fixed case and the floating case are described in dedicated sections below.

5.2.1.2. For Vortex simulations

5.2.1.2.1 LHS algorithm

Latin Hypercube Sampling (LHS) [14.]is often used to produce a space-filling design of a hypercube input space. However, for an irregular input space, the LHS is not fulfilling the intention of being a space-filling design. To alleviate this, we have used a k-means clustering algorithm (see e.g. [15.]) to select candidate points that optimize the hyper-space between each candidate point. The algorithm to come up with these k input points can be described as:

Pseudo algorithm for the space-filling design of irregular input space:

1. Sample N points x_i from the n-dimensional hyper-cube input space Ω_{HC} using an LHS where $N \gg n$ (i.e. much larger sample than the number of dimensions).

2. Filter out all points which fall outside the irregular input space Ω so that the remaining M points $x_i \in \Omega \quad \forall i$
3. Apply a k-means clustering algorithm to cluster the M remaining samples into k clusters
4. Select either the center point of the cluster or the closest of the M points in each cluster as candidates for the space-filling design.

Figure 63 illustrates one set of filtered LHS where each color represents one of the k clusters and the black crosses are the center of each cluster.
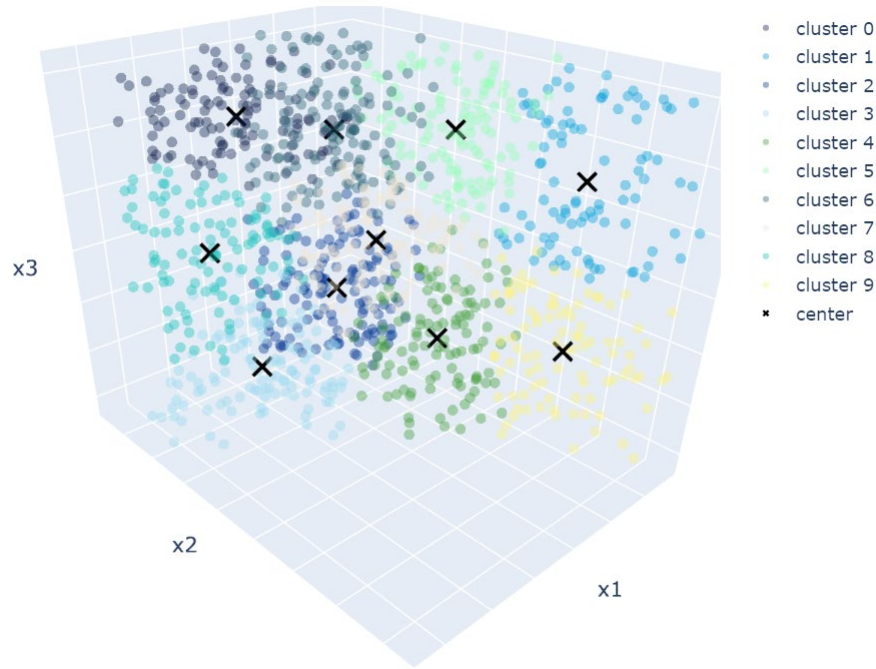

Figure 63 K-Means candidates for space-filling design

5.2.1.2.2   GP uncertainty-based exploration-exploitation strategy for DoE iterations

A Gaussian process (GP) is a stochastic process where any finite linear combination of the random variables has a multivariate normal distribution. A Gaussian process $\hat{f} \sim \mathcal{GP}(\mu(x), K(x, x'))$ can be used as a prior probability distribution over function $f: \mathbb{R}^{n_x} \to \mathbb{R}$ and is fully defined by its mean and covariance functions:

$$\mu(x) = \mathbb{E}[\hat{f}(x)]: \mathbb{R}^{n_x} \to \mathbb{R},$$

$$K(x, x') = \mathbb{E}\left[\left(\hat{f}(x) - \mu(x)\right)\left(\hat{f}(x') - \mu(x')\right)\right]: \mathbb{R}^{n_x \times n_x} \to \mathbb{R}.$$

Here x is a vector in $\mathbb{R}^{n_x}$ which corresponds to a point in the input space. Let X be the $n_x \times N$ matrix of N input vectors, while $Y = [y_1, \ldots, y_N]^T$ is the corresponding observations. The vector

$\hat{f}|\mathbf{X} \sim \mathcal{N}(\mu(X), K(X,X))$ is then multivariate Gaussian, and under the assumption that the relationship between the latent function values and the observed output is Gaussian, $Y|\hat{f} \sim \mathcal{N}(0, \sigma^2 I\_N)$, the distribution of new observations at X^* can be predicted as:

$$\mathbb{E}[\mathbf{f}^*|X^*, X, Y] = \mu(X^*) + K(X^*, X)[K(X,X) + \sigma^2 I_N]^{-1}(Y - \mu(x)),$$

$$cov(\mathbf{f}^*|X^*, X, Y) = K(X^*, X^*) - K(X^*, X)[K(X,X) + \sigma^2 I_N]^{-1}K(X, X^*),$$

where $\hat{f}^*|X^*$ is the predictive distribution of $f(X^*)$ and $\hat{f}|X^*, X, Y$ is the predictive posterior given the observed data X, Y.

For a physical system with a continuous response, it is reasonable to select a covariance (kernel) function which is at least once differentiable. A much-used covariance function for physical systems is the Mátern 5/2 kernel which is twice differentiable:

$$K(x, x') = \sigma\left(1 + \frac{\sqrt{5}r}{\ell} + \frac{5r^2}{3\ell^2}\right)exp\left(-\frac{\sqrt{5}r}{\ell}\right)$$

where

$$r = \sqrt{\sum_{i=1}^{n_x} \frac{(x_i - x_i')^2}{l_i}}$$

and l is the anisotropic length scale for each of the i dimensions. The length scale is an important hyperparameter that is optimized when training the GP. See [16.] for more details.

After running an initial set of simulations that produces the outputs $Y|X$ one way to optimize the selection of new input scenarios is to select a point in the input space that has a high predictive variation in one of the relevant response parameters (see e.g. [14.]) within the relevant input domain Ω.

Figure 64 (left) shows a trained GP fitted to the time-averaged power of electricity production of 10 simulation runs of the Vortex simulator. On the right, the standard deviation (std) of the GP is plotted. Note that the input and response space is normalized using a Standard scaler to remove the mean and scale it to unit variance.

Based on the method described by [14.], where the objective is to reduce the maximum uncertainty in the predictions across the relevant input space, a good candidate for a new simulation would be the sample with the maximum std (i.e. one of the darkest red points in the upper right of the right-hand plot in Figure 64).

There are also other alternative objectives for exploration-exploitation that might be relevant to explore (e.g. selecting scenarios that would reduce the global uncertainty [17.] or reduce the uncertainty close to a certain response value [18.]).
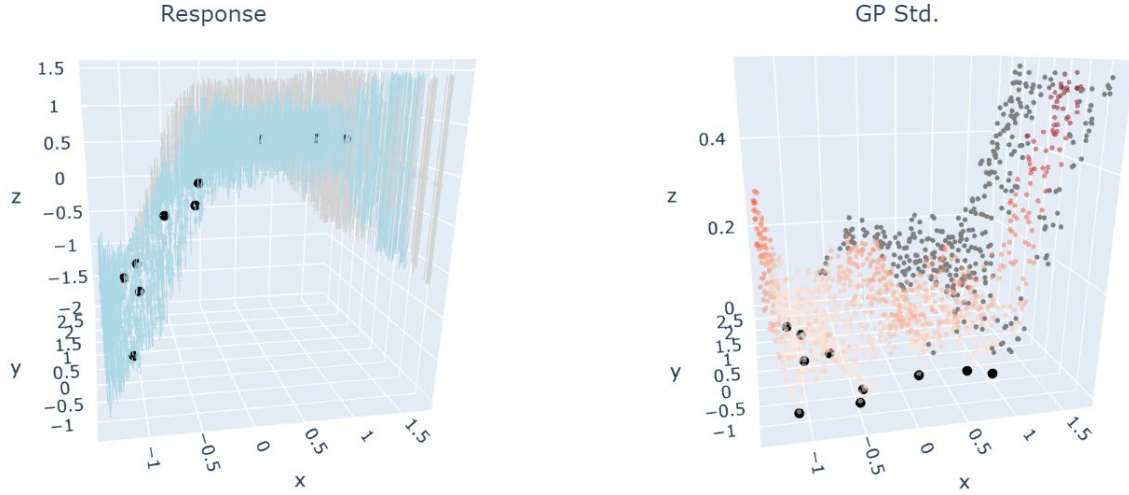
model: gp_Pow

Figure 64 Left: GP prediction for a large LHS (grey points are outside the input domain). Error bars correspond to the standard deviation of the GP. Black points correspond to simulated responses from Vortex simulations. Right: GP predicted standard deviation (std) of LHS (gray points are outside input domain), color scale corresponds to the std plotted on the z-axis – i.e. darker red corresponds to higher std.

Ideally, the adaptive DoE would be most effective if we could update the surrogate model between each new simulation run. However, the simulation runs are constrained by a limited number of iterations, and a certain number of simulations should be run in parallel to optimize the computational resources. In addition, there are multiple aspects that we would like to optimize the selection of scenarios against.

Because of the time constraint for this deliverable report, a naïve algorithm to force a space-filling exploration and at the same time, select simulations with high predictive uncertainty has been applied.

Pseudo algorithm for selecting N_{new} input scenarios across multiple objectives.

1. For each relevant response parameter y
2. Fit a GP to the current set of observations X, Y
3. Estimate the response and predictive uncertainty for a reasonably large LHS across the relevant input domain Ω
4. Perform Steps 1 through 3 of the space-filling design of the irregular input space algorithm described in section 5.2.1.2.2
5. For each cluster mark the point with the highest std as a candidate
6. Manually select N_{new} scenarios among the set of generated candidates while considering that selected candidate points across the different objectives should not be too close in the input space as these would generally be less informative than two points spaced further apart.

Figure 65 shows the GP std of the time-averaged power with the first iteration of vortex simulations (black points), new candidate points in dark blue based on the DEL of Flap moment delFlap (points), DEL of Edge moment delEdge (+), time-averaged Power Pow (diamond), and time-averaged Thrust (x). The final selection of new simulation points is represented by magenta points. Note that only the Power (diamonds) corresponding to the LHS std is shown in the figure. The other candidate points are plotted at the std for their corresponding response, but this has not been plotted to declutter the figure.
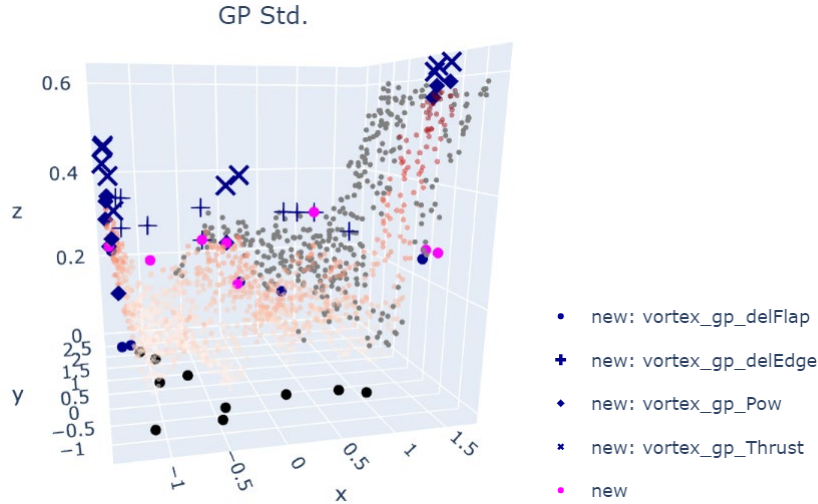
Figure 65 GP std of the time averaged power with candidates and new points selected for the second iteration

5.2.2. Aero-servo-hydro-elastic simulations

5.2.2.1. Wind generation

The wind input files for the ASHE simulations (ie. "turbulent box") are generated using HiperSim, developed earlier in the HIPERWIND project [19.]. They are generated according to the DoE, giving, for each case, different values of wind speed at hub height (U_h) and turbulence intensity (TI). Other constant parameters have been adjusted and used for all wind generation, such as the time length of the wind file (3900s), includes 300 s for setting the simulations and which are filtered in the 1h results, and the temporal resolution (dt = 0.1). The synthetic turbulence is generated using a Mann spectrum with the same seed number for all turbulent winds. Consequently, this study does not integrate uncertainty due to a potential variability due to the seed of turbulent wind realization.

Teesside and South Brittany wind turbines having different sizes and hub heights, distinct spatial resolutions are used for each case, but with a common strategy to obtain at least 25 elements per rotor diameter. Regarding the size of the turbulence box, it is proportional to the different wind turbine sizes and the solver approaches. Therefore, wind files with domains between 1.25Dx1.25D and 1.5Dx1.5D are used for BEM simulations while for the Vortex ones an 8Dx8D domain is proposed, where D denotes the rotor diameter.

A deeper insight into the input parameters for the turbulent box generation using HiperSim for both wind turbines can be found in Appendix A.

5.2.2.2. General simulations set up

To perform a comparison between the (Diego, HAWC2 and DeepLines Wind™), a significant amount of simulations were performed for different environmental conditions according to the distinct DoE cases.

For each case, aero-elastic simulations were performed during a total physical length of 3900 s, using turbulent wind files of 3900sec. The timeline is illustrated in Figure 66. The analyses (code-to-code comparisons) have been performed over the last 3600 s (*i.e.* "Analysis phase").
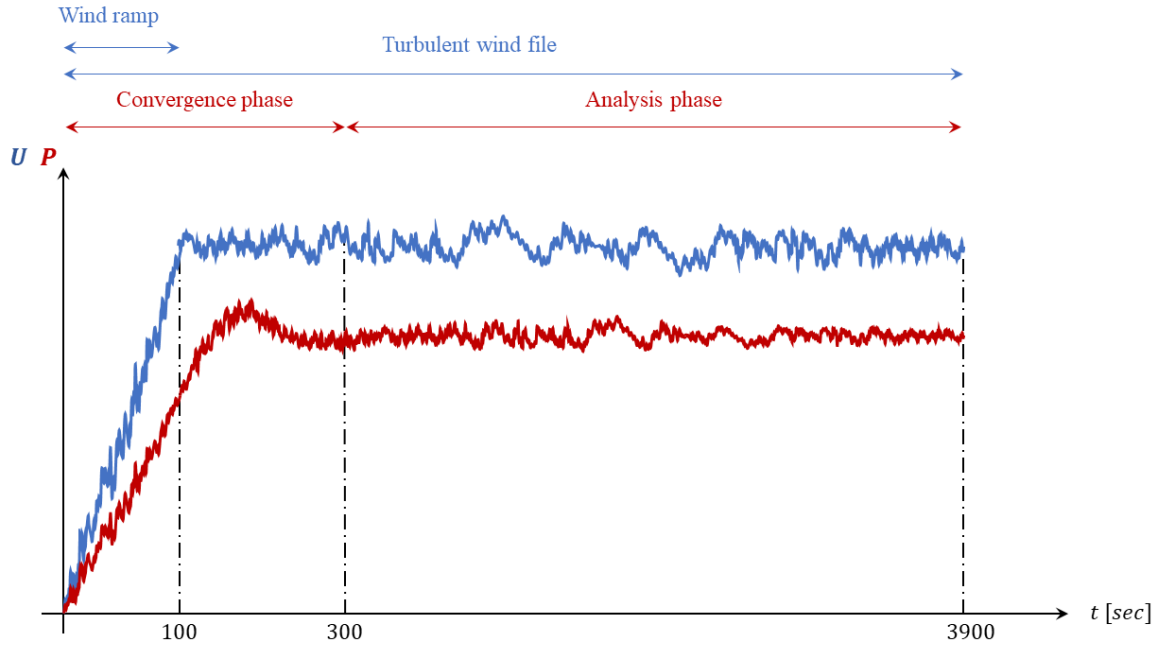

Figure 66: Timeline of the simulations

To let the wind turbine reach a converged operating state, a "Convergence phase" of 300 s is considered:

- At the beginning of the simulation, a wind ramp of 100 s is applied to the wind to progressively reach the target mean wind speed. Moreover, an initial torque is imposed to initiate the hub rotation.
- After these first 100s, additional 200s will be considered as spin-up time, leaving the last 3600 s of the simulations for output analyses.

All the aero-elastic simulations follow the settings shown in **Table 16**.

***Table 16**. Aero-elastic model configuration*

Simulation length	3900 s
Δt	0.01s
Number of blade elements	48 (Teesside) or 49 (South Brittany) (as in WP1)
Wind ramp	*0-100% over* 100 s
Env. Conditions	from DoE

Although it is intended to perform the same simulations with the 3 BEM solvers, numerical models might be slightly different. To evaluate the uncertainties of aero-elastic simulations as used in the industry, it seems relevant to use the software as recommended. Therefore, the setup of the simulations respected the best practices advised by the software developers, especially for the BEM corrections. The different BEM corrections models used by the 3 BEMs are listed in **Table 17**.

Table 17. Different correction models used for BEM simulations by the partners

Model	IFPEN	EDF	DTU
Dynamic inflow	Øye [20.]	Øye [20.]	Øye [20.]
Dynamic stall	Øye [21.]	Beddoes-Leishman [29]	Øye [21.]
Skewed wake	Glauert [23.]	Pitt and Peters [25.]	[27.]
Root/Tip Loss	Prandtl [24.]	Prandtl [24.]	Prandtl [24.]
Tower shadow	Yes [26.]	No	Yes [26.]
3D effects	No	No	Yes [28.]

On the other hand, the corrections used for vortex simulations are presented in **Table 18**.

Table 18. Different correction models used for free vortex wake simulations

Model	Vortex
Dynamic stall	Øye [21.]
Tower shadow	Yes [26.]

Note that in the case of the South Brittany wind turbine only DLW BEM and Vortex simulations are carried out because of time constraints, leaving the study with the other two BEM's models for a future work.

For the sake of simplification, the controller parameter setting are chosen to be the same for both BEM and Vortex simulations, hence being non optimal for the Vortex ones. As it is discussed later, this choice may have a large influence on the rotor speed and consequently on the production and design considered quantities, specifically for the large floating OWT case study.

5.2.2.3. Simulation outputs: quantities of interest

To compare the different solvers, time series of integrated loads on the rotor, aerodynamics loads along the blades, and fatigues at blade roots are considered. A shortlist of the outputs is given below.

- *Integrated loads on the rotor (hub coordinate system):*
    - *Mechanical thrust*
    - *Mechanical torque*
    - *Electrical power of electricity production*
- *Aerodynamic loads along the blades (airfoil coordinate system):*
    - *Normal aerodynamic load*
    - *Tangential aerodynamic load*
- *Fatigue at blade root (elastic coordinate system):*
    - *Flapwise moment DEL*
    - *Edgewise moment DEL*

Aerodynamic loads

Both normal $\overrightarrow{F_N}$ and tangential force $\overrightarrow{F_T}$ are compared. The forces are illustrated in **Figure 67**: the tangential force is colinear to the chord line; the normal force is normal to the tangential one.
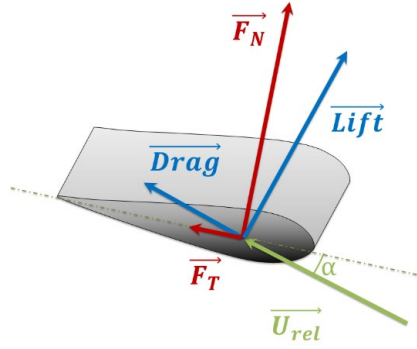
Figure 67. *Illustration of normal and tangential forces*

These outputs are evaluated on 5 points along the blades. The aim was to have two points close to the root and to the tip respectively, and three in the middle. In terms of percentage, the distances for the positions were 10%, 25%, 50%, 75%, 90% from root to tip. The loads were linearly interpolated to the exact position of interest from the two closest points. The results on these points are not displayed in this report but can be provided on demand.

Fatigue

For the fatigue comparison, blade root edgewise and flapwise moments time series (elastic frame) are used to compute the respective DEL as follows:

1. The time-series of edgewise and flapwise moments of the considered blade root (considering only the last 3600 s of simulation) are respectively denoted M_{edge} and M_{flap};
2. The rainflow cycle counting method is used to extract the number of cycles $n_{edge,i}$ (resp. $n_{flap,i}$) with range $M_{edge,i}$ (resp. $M_{flap,i}$) from M_{edge} (resp M_{flap}) for every cycle range observed by the rainflow algorithm;
3. The edgewise and flapwise moment DEL denoted respectively DEL_{edge} and DEL_{flap} are then given by:

$$DEL_{edge} = \sqrt[m]{\frac{\sum_i M_{edge,i}{}^m n_{edge,i}}{N_{ref}}} \quad \text{and} \quad DEL_{flap} = \sqrt[m]{\frac{\sum_i M_{flap,i}{}^m n_{flap,i}}{N_{ref}}}$$

where the Wöhler exponent m is set to 10 and $N_{ref} = 10^7$.

5.3. Fixed case: a turbine of Teesside farm

5.3.1. DoE generation for BEM simulations

5.3.1.1. Goal of the Design of Experiments

The relevant input space Ω is defined as the set of (U, TI, θ_{yaw}) such that:

- The time-averaged wind speed at hub height $U \in [u_{min}, u_{max}]$. The lower and upper bounds of this interval correspond respectively to the cut-in and cut-out of the wind turbine;
- the bounds of the turbulence intensity TI (i.e. U over std) are defined from the empirical 1% and 99% conditional quantiles of TI. These quantiles were computed using 5 years of SCADA data measured on the Teesside wind farm;
- the wind yaw misalignment $\theta_{yaw} \in [-30°, 30°]$. This interval is larger than the usual $[-10°, 10°]$ uncertainty of non-optimal wind turbine yaw alignment to the wind, to consider also a potential wake steering strategy.

The method described in section 5.2.1.1 is used to obtain a DoE of 300 points that covers the domain Ω. The data of Teesside wind farm are confidential. Therefore, throughout this section, every quantity displayed in the figures is linearly normalized in [0,1] with 0 as minimum and 1 as maximum (except for θ_{yaw}).

5.3.1.2. Figures of the resulting DoE

After 3 million iterations of the algorithm, the 2D projections and the 3D plot of the resulting DoE are displayed in the following figures:
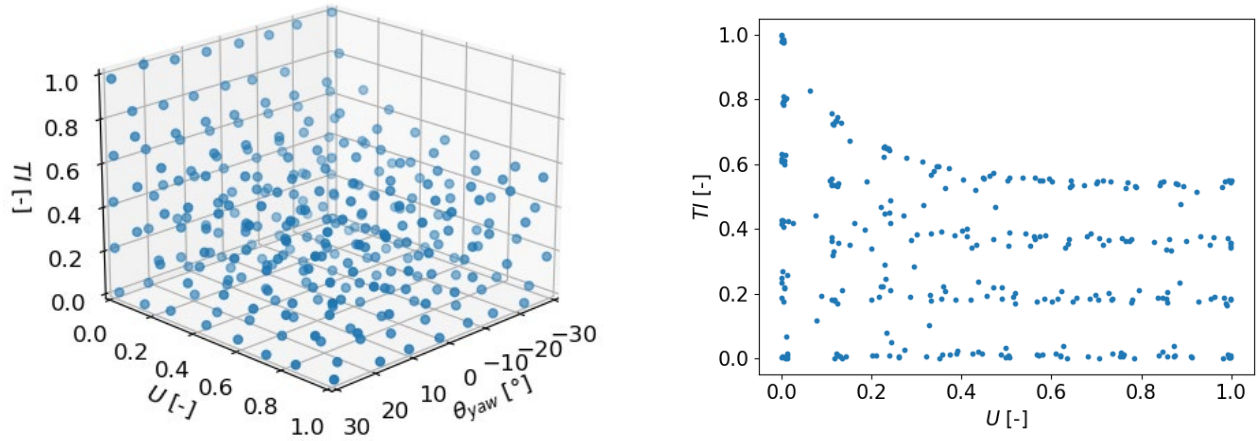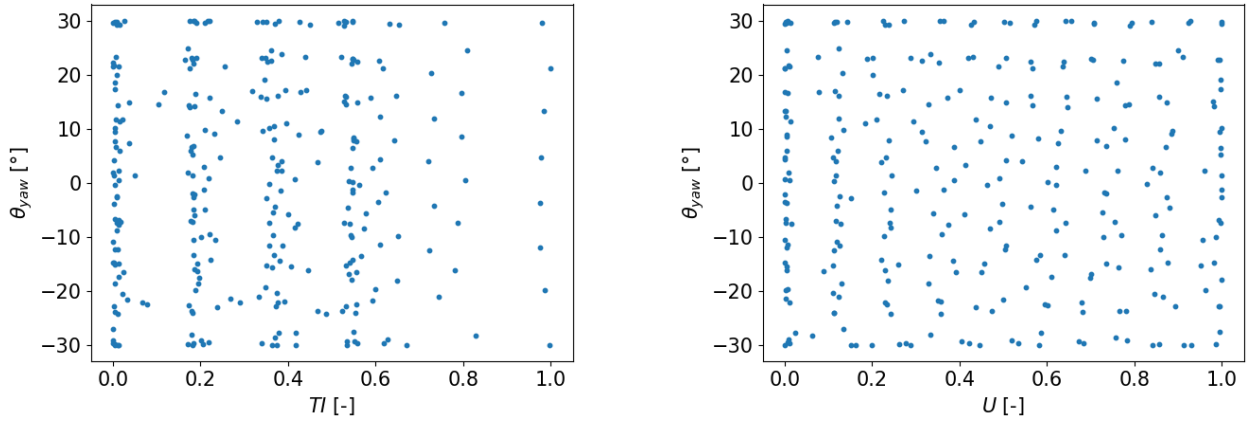
Figure 68. 2D and 3D plots of the DoE for the BEM simulations

The 3D plot, given in top left figure, shows that the points of the DoE are well spread over the entire domain of interest Ω. The other 2D plots illustrate the projections of the DoE points in the different subspaces.

5.3.2. Simulation set up

As Teesside has fixed wind turbines, only environmental conditions related to the wind field were considered while the state of the sea was neglected. Each simulation was forced by the corresponding wind file among the 300 wind files produced with HiperSim, according to the wind speeds and turbulent intensities defined for each case in the DoE stage.

General simulations inputs parameters have been introduced in 5.2.2.2. The wind turbine includes a controller, which imposes a time step of $\Delta t = 0.01$s. The simulation length and the wind file length are about 3900s, enabling a convergency phase with a wind ramp (0-100% over 100s) and an initial torque (over 10s). More details about wind generation can be found in Appendix A. As mentioned in 5.2.2.3, the outputs are averaged over the last 3600 s. The yaw is applied on the wind turbine (ie. not in the wind file), according to the convention given in Figure 69.
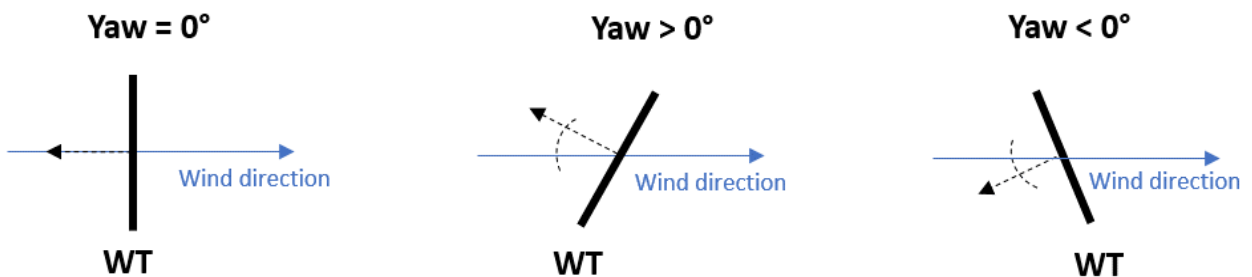

Figure 69. Illustration of yaw angle, seen from the sky

94

5.3.3. Overview of BEM results

In this section, an insight into BEM simulations results is proposed. The vortex results will be analyzed later. The aim here is to give the reader an overview of the results obtained, before going deeper in the analysis. Even though all the quantities of interest mentioned in section 3.2.2.2 were analyzed, only some of the BEM results for power, thrust, torque, and DEL are presented. However, all the 3D plots for the entire outputs can be provided on demand. One can note that the values are linearly normalized in [0;1] for confidentiality purposes.
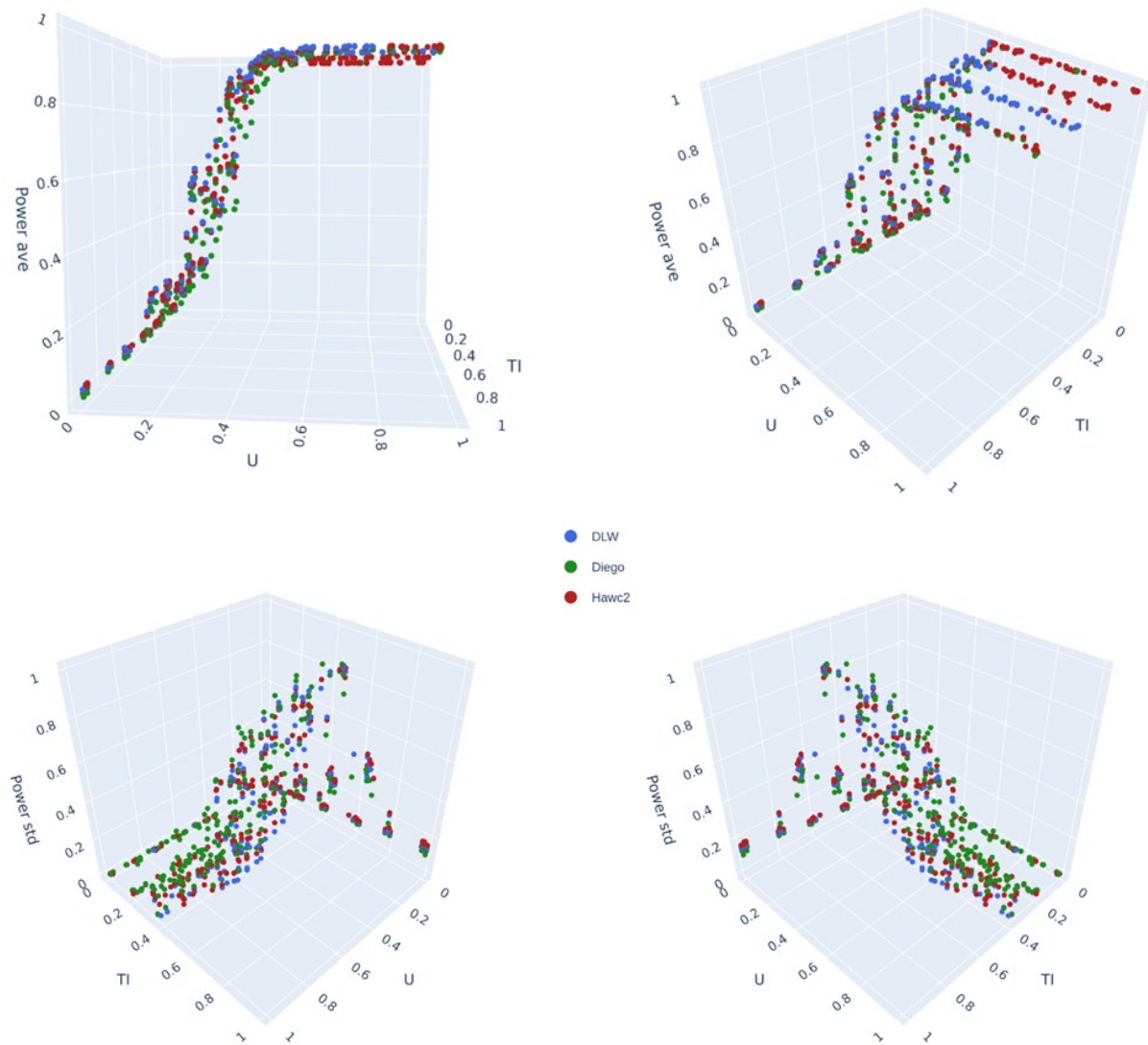
5.3.3.1. Power

Figure 70. BEMs results for mean power (top) and power std (bottom).

Figure 70 presents the BEM model results for the time-averaged and the standard deviation of the power. These 3D plots give the normalized power (z-axis) for different values of wind speed and turbulent

intensities (x-axis and y-axis respectively). One can note that θ_{yaw} is not represented: two close points of (U, TI) can have different yaw angles. On the top left plot, the power curve for Teesside wind turbines can be observed. From the analysis of the same plot with a different view (top right), it can be inferred that the main driver for the power is U while the effects of TI are less dominant. However, when the std is analyzed (bottom plots), one can see that TI plays an important role in the power variability. Both figures highlight that the power std increases rapidly with TI, especially for rated conditions (i.e. near U=0.4).
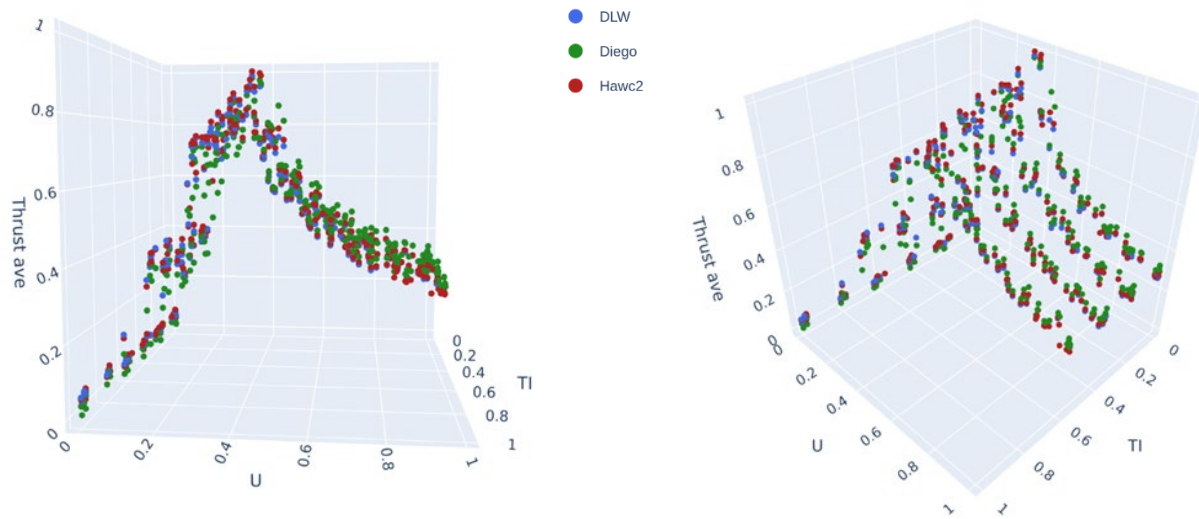
5.3.3.2. Thrust

Figure 71. BEMs results for mean thrust.

In Figure 71 the BEM's results for the time-averaged thrust are presented. On both plots, the typical thrust curve can be observed with an increasing thrust below the rated speed, followed by a reduction at above-rated wind speeds. With a different view angle (right plot), it is possible to identify the effect of the TI on the thrust. This plot suggests that for a constant wind speed, the thrust increases when the TI diminishes.
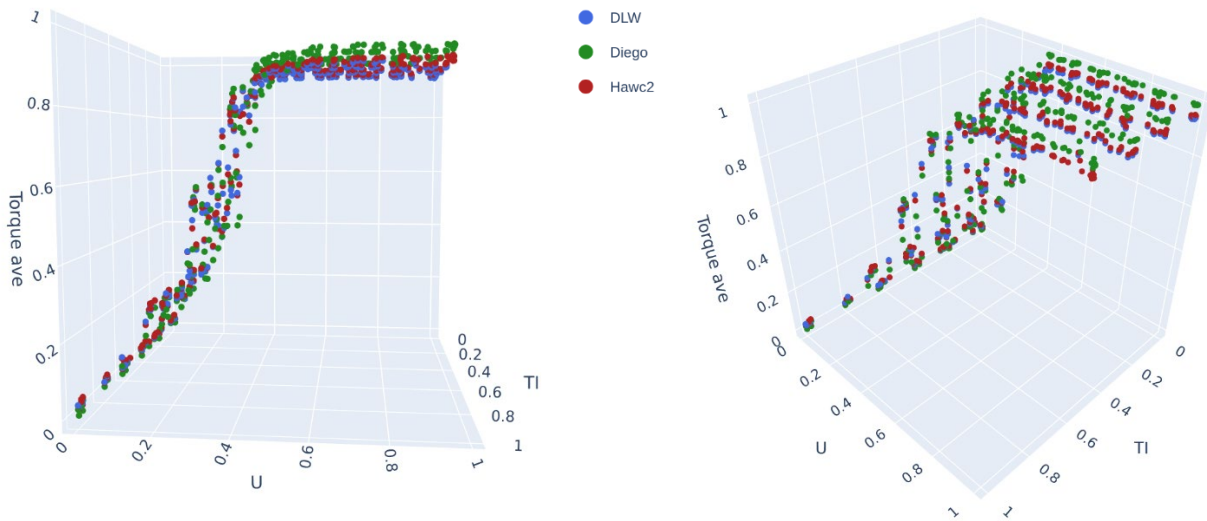
5.3.3.3. Torque

Figure 72. BEMs results for mean torque.

Figure 72 shows the BEM's results for the mean torque. In this figure is possible to observe the typical torque curve and that the three models are consistent. Moreover, it can be seen for the power and the thrust, the effect of the TI and the Yaw on this variable is, as expected, less dominant than the effect of the wind speed.
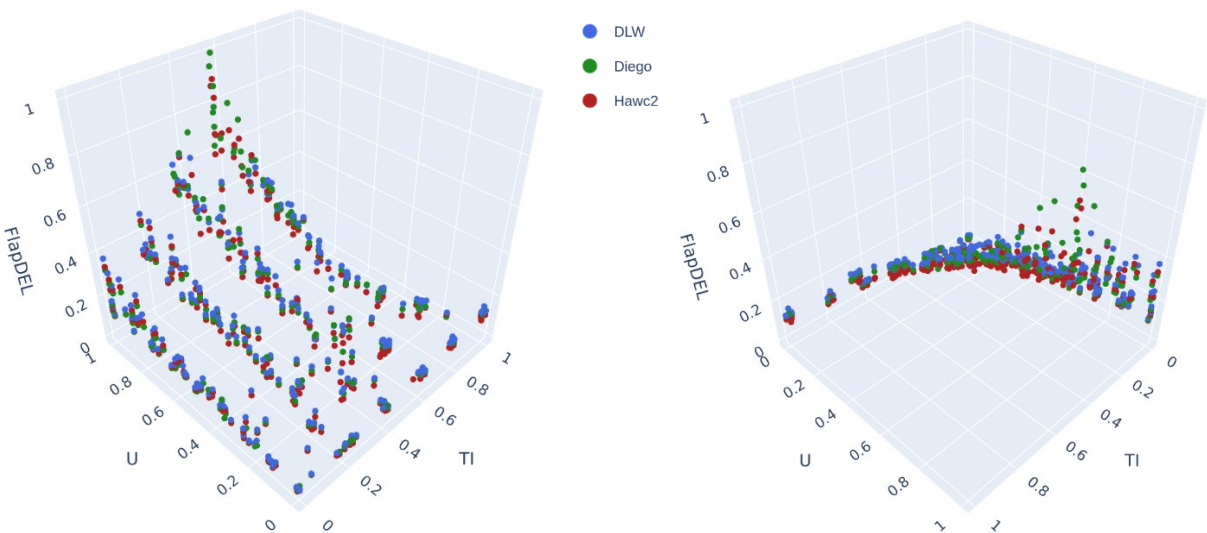
5.3.3.4. DEL

Figure 73. BEMs results for flapwise DEL.

Figure 73 shows the BEM's results for the flapwise DEL from two angle views. It appears from these figures that the DEL increases with respect to *TI* and *U* and that there is a good agreement between the 3 codes. These trends are usual and can be interpreted as a contribution of *TI* to the number of rainflow cycles and of *U* to the cycle amplitudes.

5.3.4. Uncertainty evaluation

To estimate the uncertainties between BEM and Vortex solvers, an iterative and optimized DoE (30 points) for vortex simulation has been defined, as described in section 5.2.1.2. The setup of the simulation corresponds to section 5.3.2, using the vortex code setup introduced in 5.1.2.2.

This section presents the Gaussian Process (GP) regression models trained on both the BEM and Vortex simulations, as well as their validation and general considerations related to the combination of GPs based on low-fidelity BEM and high-fidelity vortex simulations.

5.3.4.1. Validation of Gaussian process models

Several GP models have been trained based on different relevant responses in the simulation results from both the BEM and Vortex simulations. To document the process and the accuracy of the fit for some selected responses, this section introduces validation results for four quantities of interest from both the BEM and Vortex simulations. The four quantities have been selected from those presented in section 5.2.2.3 and have been denoted by the short form:

Table 19 Selected quantities of interest and short-form denotation

Short form	Description (see section 5.2.2.3)
Power	*Power of electricity production - Integrated loads on the rotor (hub coordinate system)*
Thrust	*Mechanical thrust - Integrated loads on the rotor (hub coordinate system)*
delFlap	*Flapwise moment DEL - Fatigue at blade root (elastic coordinate system)*
delEdge	*Edgewise moment DEL - Fatigue at blade root (elastic coordinate system)*

A GP is fully defined by the selected mean function, kernel function, the optimized (trained) hyperparameters, and the data used to optimize it (see section 5.2.1.2.2). To validate how well the model generalizes and avoids overfitting, prediction residuals have been calculated using two different cross-validations (CV) techniques.

The GP in this work has been optimized using the python package GPyTorch [33.] and the optimization routines of the tensor package torch [34.]. The GPs have been optimized using the Adam optimizer with a Marginal log-likelihood loss function.

The BEM simulations have been run for 300 input scenarios. A K-Fold cross-validation has been used to split the simulation results into 10 folds where the trained model (i.e. the optimized hyperparameters of the kernel function) is kept fixed, while the GP makes use of approximately 90% of the simulation data while leaving the remaining 10% out, and comparing the GPs prediction with the true observations for this 10%.

Then, iterating across all combinations of the 10 folds (i.e. all combinations of 90% training data and 10% test data), a full set of cross-validated data is obtained.

The Vortex simulations have only been run for 30 input scenarios (compared to the 300 for the BEM simulations). This is a much sparser data set, and thus the CVs have been obtained through leave-one-out. This technique is similar to the K-Fold technique, but because of the limited amount of data only one input scenario is left out at each iteration.

The Root-mean-squared-error and the Coefficient-of-determination (r2-score) have been calculated for the full CV set of predictions and true observations and are presented in Table 20.

Table 20 Regression metrics for the accuracy of fit - Teesside

	delFlap BEM / Vortex	delEdge BEM / Vortex	Power BEM / Vortex	Thrust BEM / Vortex
RMSE	0.053 / 0.146	0.091 / 0.173	0.009 / 0.083	0.029 / 0.193
r2-score	0.997 / 0.972	0.992 / 0.927	0.9999/ 0.992	0.999 / 0.957

In Figure 74 three plots illustrate the prediction accuracy of the GP for each of the four selected responses. On the left, a quantile-quantile (qq) plot shows the standardized CV residual plotted as quantiles against the theoretical quantiles of a standard normal distribution. In the middle, the distribution of the CV residuals (histogram) and the corresponding estimated probability density using kernel-density-estimate (kde) are compared to the probability distribution of the standard normal distribution. Both plots show that the predictions errors of the fitted GPs are reasonably well Gaussian distributed. The bulk of the predictions is concentrated closer to the real values than a Gaussian distribution would indicate. Note, however, that there are also some outliers where the residuals are outside the assumed Gaussian variations. On the right, the CV predictions are plotted against the true observations in a unity plot. Here, all plots that are on the dashed black diagonal indicate a "perfect" prediction. The GPs are generally accepted as good models when the predictions including their uncertainty are close to the unity line, and when the prediction uncertainty is sufficiently small (i.e. where the uncertainty is less than what is needed to discriminate between the relevant decisions based on the predictive responses).
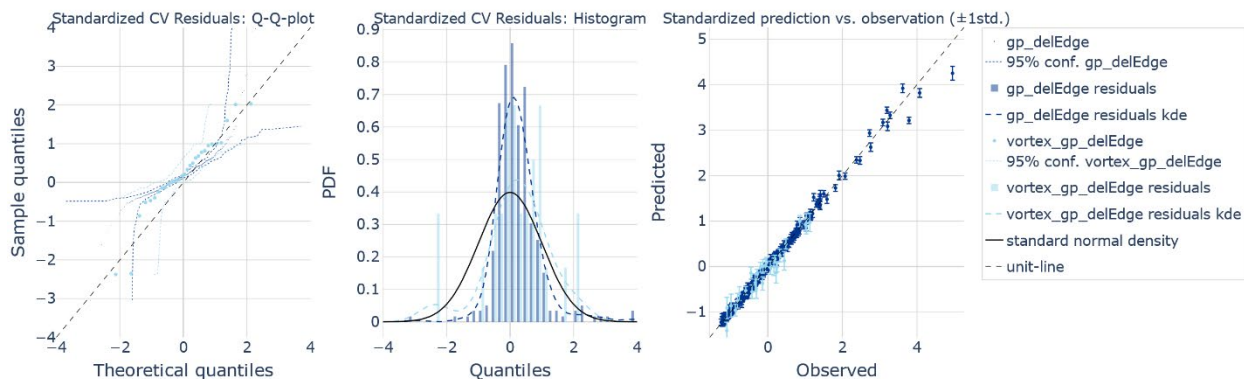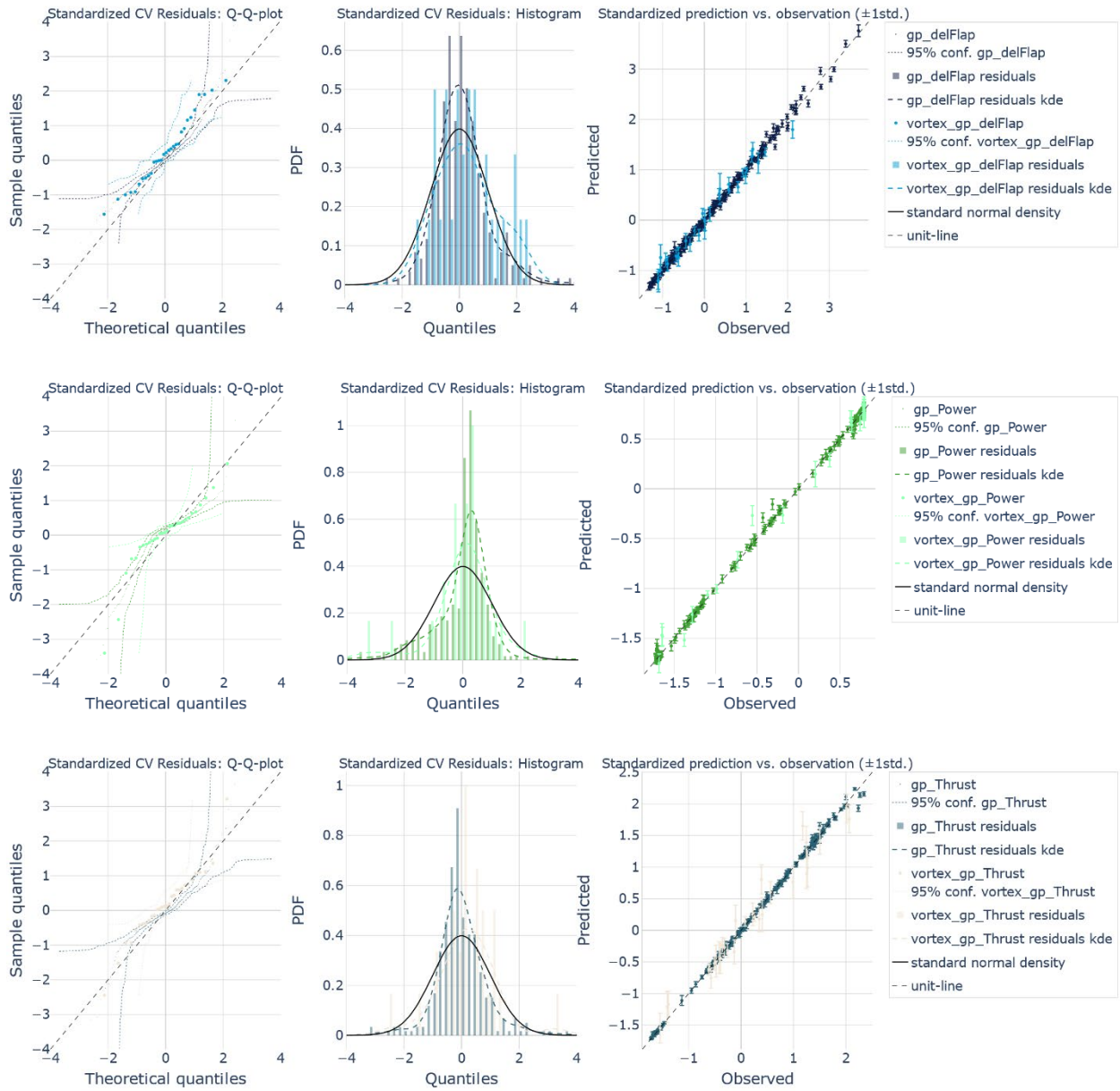
Figure 74 For each of the standardized quantities of interest: (left): plot of the Theoretical vs. Sample quantiles of the CV residuals, (middle): corresponding distribution of CV residuals, (right): CV prediction vs true observation including 1 standard deviation. From top to bottom the plots represent the distribution of Edge DEL, Flap DEL, Power, and Thrust.

5.3.4.2. Uncertainty evaluation

The GPs fitted to the Vortex simulation results and the corresponding GPs fitted to the BEM results show a reasonable agreement across most of the relevant input space (i.e. for input scenarios within the environmental contours [31.]). To analyze the difference between the Vortex and BEM simulation results,

an LHS has been generated from the entire input space and filtered based on the environmental contours for the Teesside site. Figure 75 shows three plots for each of the selected quantities of interest.

On the left, the simulated response, as well as the GP prediction of the response for the LHS, are plotted in different colors. The large circles correspond to Vortex and BEM simulations (see legend), while the small dots indicate the mean GP prediction for each sample in the LHS. The vertical lines illustrate two std of the prediction uncertainty. Note that samples outside the environmental contours are plotted in gray.

In the middle, the standard deviation of the GP prediction is plotted relative to the maximum range of response of the observations (e.g. max-min) for both the GP based on BEMs and Vortex simulations. The dots are colored according to the size of the standard deviation where the blue ones correspond to the GP based on the BEM simulations and the red ones correspond to the GP based on the Vortex simulations.

On the right, the relative deviation between the GP predictions based on Vortex and BEM simulations is plotted. The gray error bars indicate the combined uncertainty of the discrepancy between the two GPs.

For all the plots the positions of the Vortex simulations are indicated in magenta.

For all of the quantities plotted here, there seems to be a reasonably good agreement between the Vortex and BEM GPs in the region of the input space where the bulk of the environmental scenarios are located. The biggest discrepancy can be found for low wind speeds U and relatively high turbulence intensity TI, conditions which are rarely occurring, for the DEL based on the Flap and Edge moments, denoted delFlap and delEdge in Figure 75. For the Power and Thrust response, the biggest discrepancy between the Vortex and BEM GP predictions is found where the response has a fairly steep incline for wind speeds in underrated conditions. On the response plateau above approximately slightly overrated conditions, the discrepancy between the GPs are reasonably low. More metrics about relative uncertainties are provided in section 5.5.
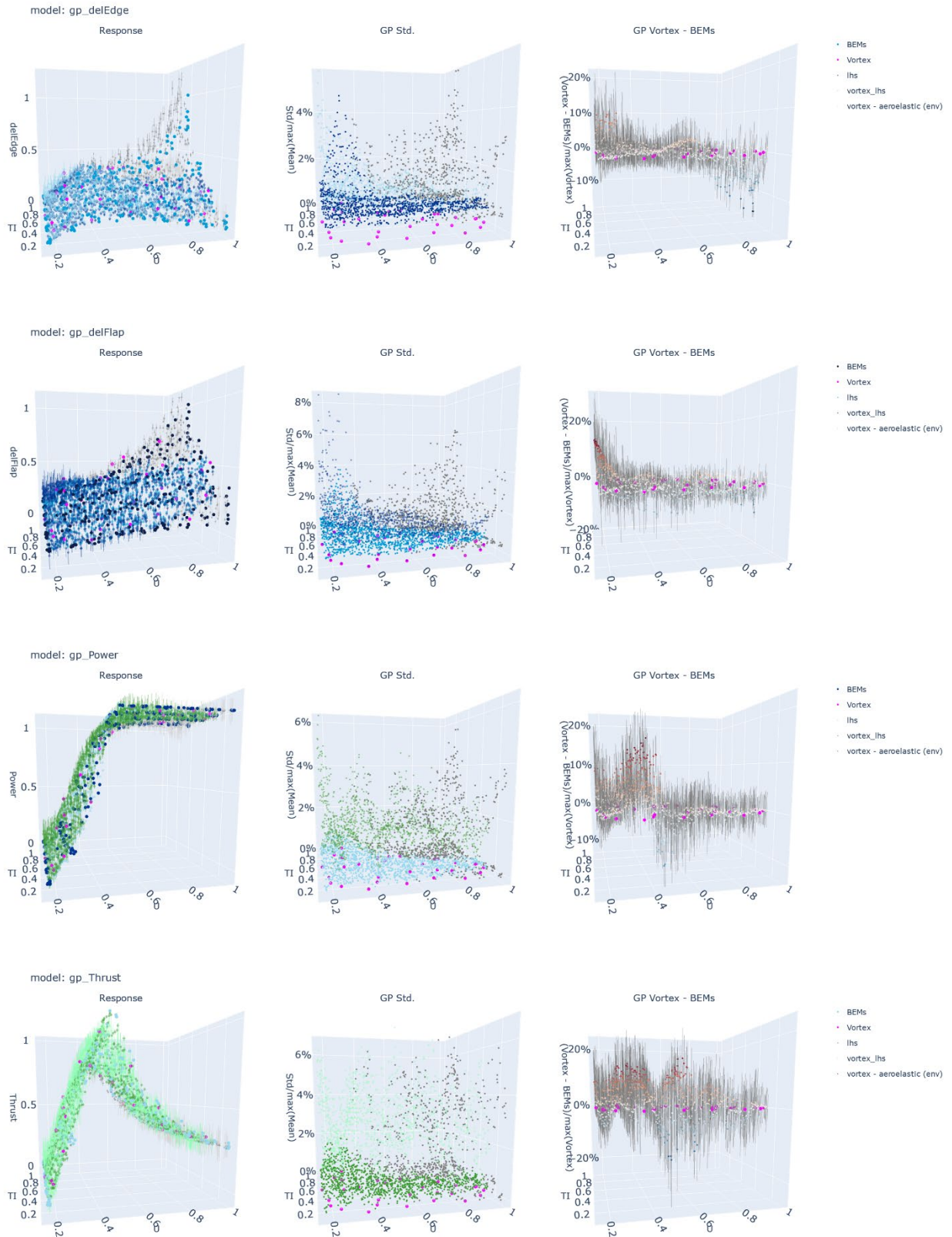
model: gp_delEdge

model: gp_delFlap

model: gp_Power

model: gp_Thrust

Figure 75 : Prediction and model discrepancy for each of the quantities of interest: (left) plotted against windspeed U and turbulence intensity TI: plot of the BEMs and Vortex simulated response (circles) and the GP prediction for the LHS (dots) – samples outside the defined environmental contour is plotted in grey, (middle): relative GP std – color scale from white to dark blue corresponds to the GP std based on the BEMs while Reds corresponds to the GP std based on the Vortex, (right): relative differences between Vortex and BEM GP prediction for the LHS.

5.3.4.3. Exploiting the metamodels

5.3.4.3.1   BEM results

5.3.4.3.1.1   Power

For a deeper analysis, the time-averaged electrical power has been estimated with the metamodels calibrated from BEM simulations (Figure 76). On the left, the power is plotted for a representative TI and a Yaw=0°. Good agreements can be observed for the different software, with a thin confidence interval (CI). On the right, the power is given for a chosen wind speed (rated condition), and θ_{yaw}=0°. It illustrates the decrease of mean power due to the increase of turbulence at rated wind speed, because of the concavity of the power curve in this area. As the software use different corrections models, some of them seem to be slightly more sensitive than the others. The confidence interval becomes wider when TI is larger than 0.6 : this is due to the definition of the domain of interest Ω which implies that this area is not well explored for this wind speed (see Figure 68).
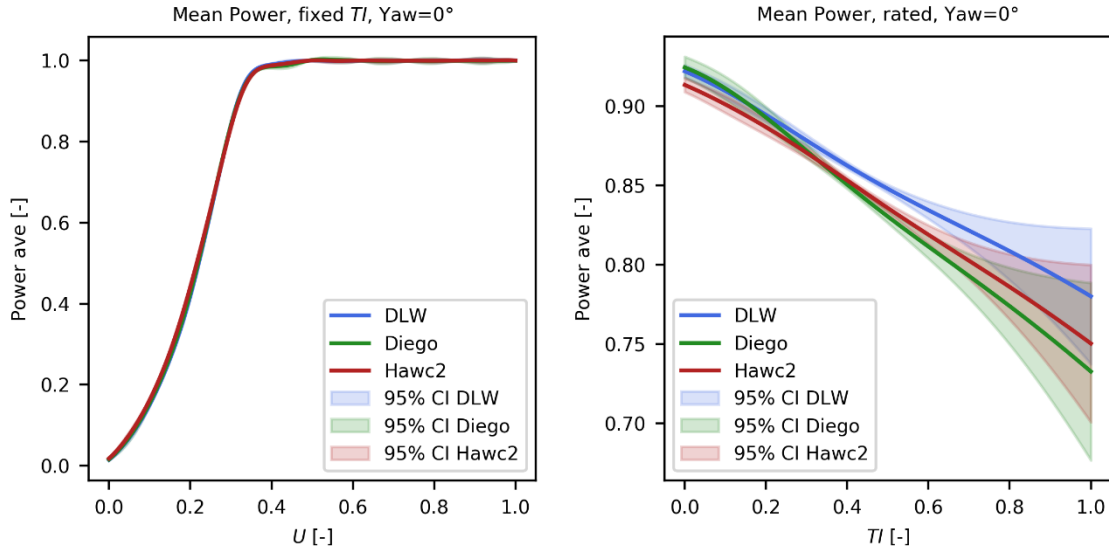

Figure 76 Power curves estimated with the metamodels calibrated from BEM simulations

5.3.4.3.1.2   Thrust

For a deeper understanding, the aerodynamic thrust has been estimated with the metamodels calibrated from BEM simulations. Some curves are given in Figure 77. On the top left, the thrust is plotted for a representative TI=0.23 (normalized value) and θ_{yaw}=0°. The different software fit fairly well, with a thin CI, despite a slight deviation of Diego for high wind speeds. On the top right, the thrust is given for a chosen wind speed (rated condition), and θ_{yaw}=0°. As for the power, it illustrates the decrease of mean thrust due to the increase of turbulence at rated wind speed, because of the concavity of the thrust curve in this area. In the bottom part, two plots showing the behavior of the averaged thrust for different values of yaw are given. The TI is the same for both of them, but the one on the left considers under-rated conditions, while the one on the right above-rated conditions. Two opposite behaviors can be observed, depending on the operating condition of the wind turbine. A slight asymmetric shape due to yaw conditions can be seen. Diego slightly deviates from the other software. It might be explained by the skewed wake correction model used. Diego has been improved for this concern during the project but the results have not been updated for this report.
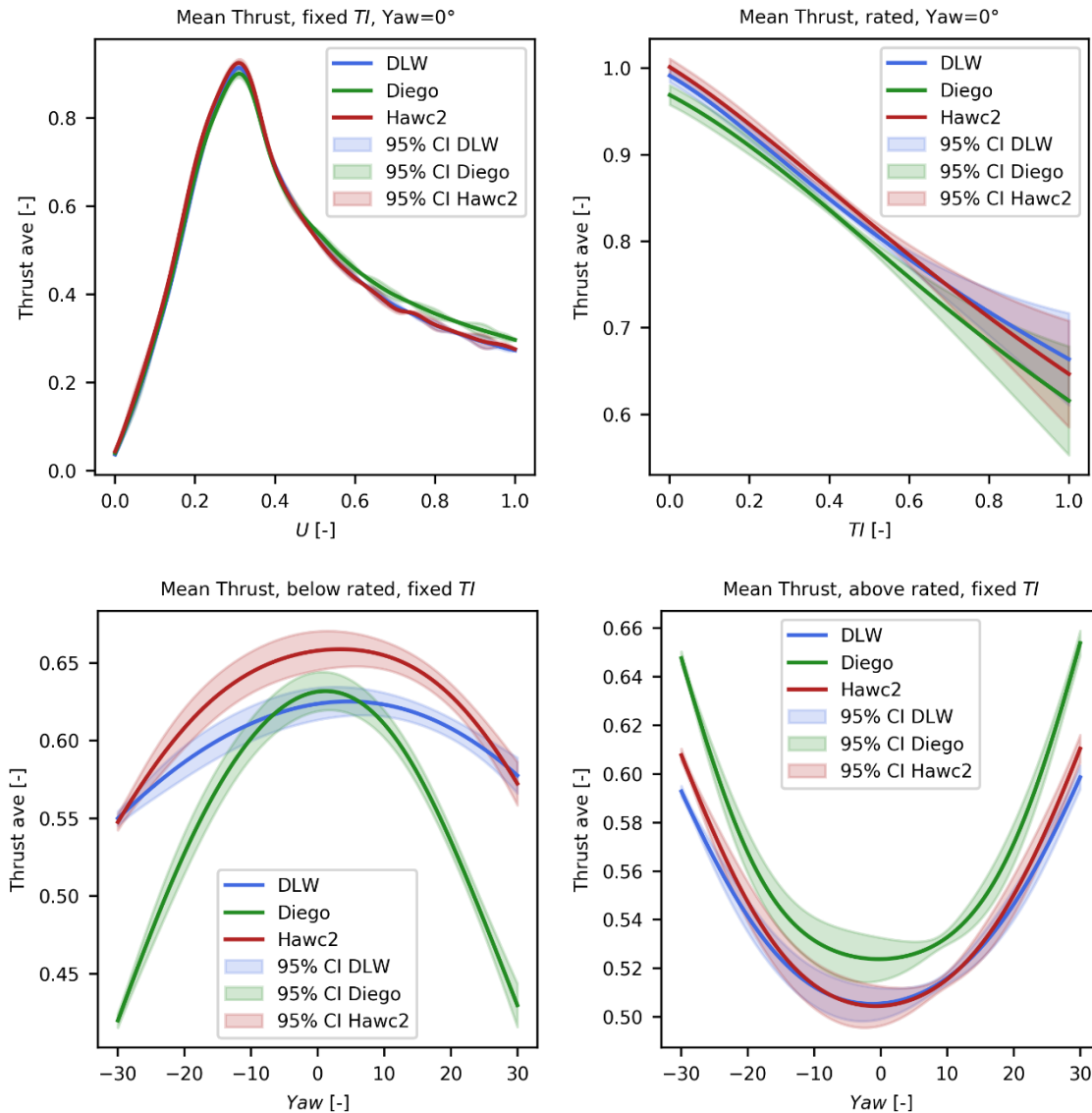

Figure 77. Thrust curves estimated with the metamodels calibrated from BEM simulations

5.3.4.3.1.3   Torque

Again, the aerodynamic torque has been estimated with the metamodels calibrated from BEM simulations for a deeper understanding. The torque curve is given in Figure 78, plotted for a usual TI=0.23 (normalized value) and θ_{yaw} set to 0°. Here, one can notice an overestimation of Diego for the above-rated conditions. It might indicate some deviations in the wind turbine controller numerical implementation: the controller is supposed to reach the rated power and does it well (as shown in Figure 76), but as the torque is different, the rotation speed is different. In the end, it leads to different pitch angles imposed by the controller between the software.
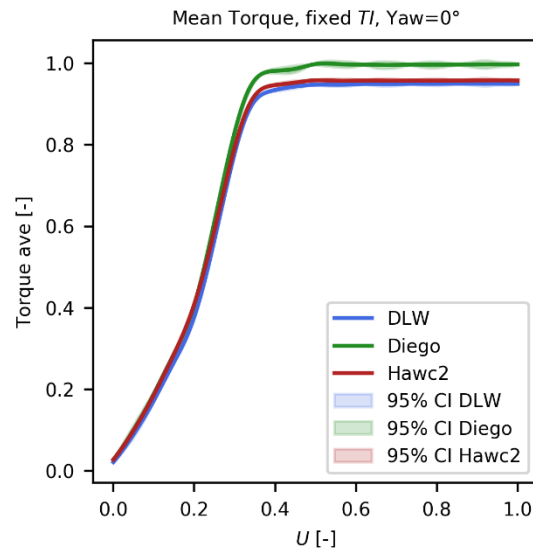

Figure 78. Torque curve estimated with the metamodels calibrated from BEM simulations

5.3.4.3.1.4   Blade root DEL

For every point of the DoE, the flapwise DEL is computed for each blade root. To study only one quantity, the maxima of the DEL with respect to the 3 blades are considered here. Figure 78 shows several curves of this flapwise DEL estimated with the metamodels calibrated from BEM simulations. A good agreement between the three codes is observed even though the Hawc2 metamodel predicts smaller DELs than the others. The uncertainties of the metamodels increase when TI is larger than 0.6 since the exploration of the DoE is focused on smaller values of TI (see section 5.3.1.2 for the definition of the domain of interest Ω). For every code, the flapwise DEL increases with respect to U and TI but is not strongly correlated with the θ_{yaw} (except for extreme values of θ_{yaw}).
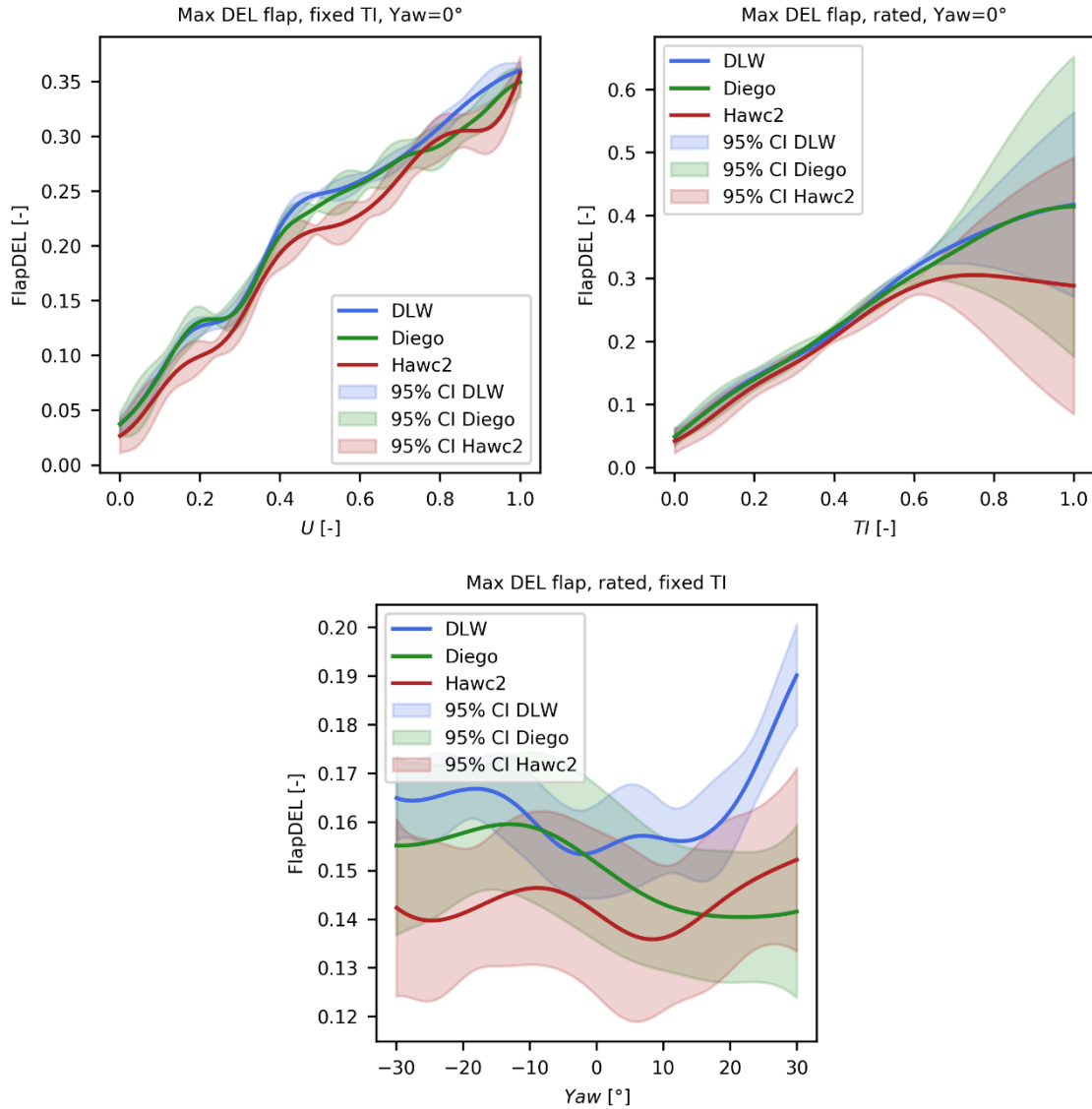
Figure 79. DEL flap curves estimated with the metamodels calibrated from BEM simulations

5.3.4.3.2   BEM vs Vortex

It is also possible to consider the average results given by BEM methodology (estimated with the metamodels calibrated from BEM simulations of Diego, Hawc2, and DLW), and compare it to vortex simulations (estimated with the metamodels calibrated from vortex simulations). The power, thrust, torque, and flapwise DEL curve for a fixed TI and θ_{yaw}=0° can be seen in Figure 80. The 95% CI envelop is wider for Vortex results, as the data set is sparse. A general good agreement can be observed between the two methodologies. The power productions fit well but discrepancies are noticed for the thrust, torque and DEL, especially between rate and above-rated conditions. A part of these differences should however come from the non optimal setting of the controller for the Vortex based model.
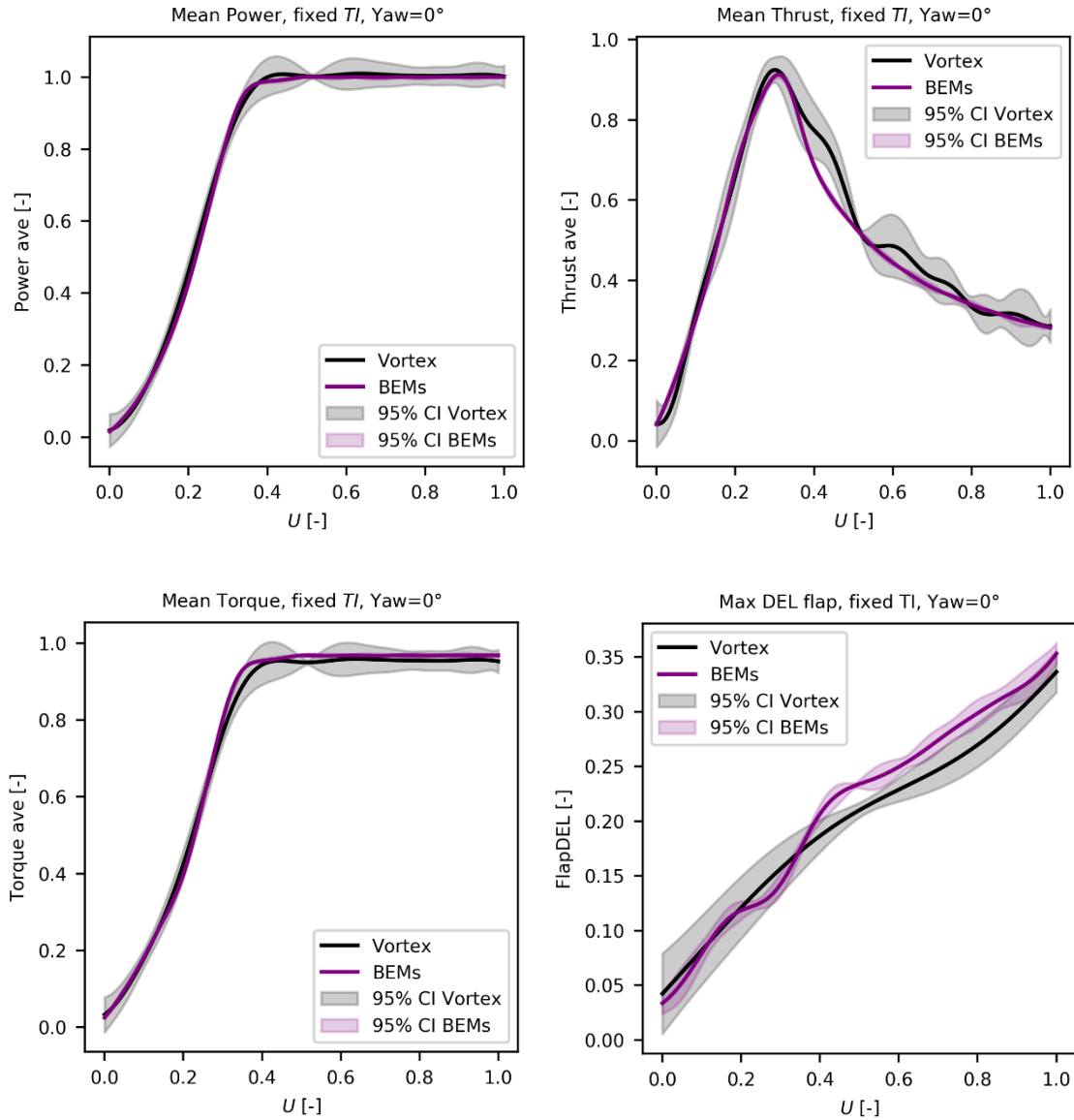
Figure 80: Power, Thrust, Torque, and DEL flap curves estimated with the metamodels calibrated from BEM simulations and Vortex simulations for a fixed wind turbine

5.4. Floating case: a turbine of South Brittany farm

5.4.1. Simulation setup

As South Britany has floating wind turbines, environmental conditions related to the wind field and the state of the sea were considered. Therefore, the case study is adapted from the turbulent winds and irregular waves case developed during HIPERWIND WP1 and WP2 based on ANEMOC data [29.]. The OWT models are based on the IEA15MW NREL OWT on UMaine semi-submersible floater which has been

modified (tower and mooring) to be adapted to the South Brittany conditions (see section 3). Each simulation was forced by one of the 700 wind files produced with HiperSim, according to the wind speeds and turbulent intensities defined for each case while building the DoE. More details about wind generation can be found in Appendix A.

General simulations inputs parameters have been introduced in 5.2.2.2. The wind turbine includes a controller (ROSCO of NREL), which imposes a time step of Δt = 0.01s. The simulation length and the wind file length are about 3900s, including a wind ramp (0-100% over 100s) and an initial torque (over 10s).

While the environmental conditions related to the wind field are considered in the wind file, the irregular waves, related to the state of the sea, are created by the software DLW. For each case, the irregular waves are produced using the JONSWAP wave spectrum and respecting the significant height (H_s), the propagation direction (θ_{wave}) and the Peak period (T_p), defined in the DoE. A JONSWAP spectrum shape coefficient (γ), and a ratio of the maximum wave height to the significant height equal to 2.2 and 1.86, respectively, are used.

For this wind turbine floating case, as the floater and mooring lines are not radially symmetric, it is intended to consider not only the propagation direction of the waves but also the wind flow direction. Therefore, the wind file is yawed to consider the wind flow direction (θ_{wind}) and, as wind turbine misalignment is not desired, the wind turbine is yawed in the different setups to be facing the wind in each case.

5.4.2. DoE generation for BEM simulations

5.4.2.1. Goal of the Design of Experiments

For the floating case, the relevant input space Ω is defined as a set of variables ($H_s, T_p, \theta_{wave}, U, \theta_{wind}, TI$) which refer respectively to the significant wave height, the wave peak period, the wave direction, the wind speed at hub height, the wind direction, and the turbulence intensity. The convention for θ_{wave} and θ_{wind} respect the one illustrated in Figure 7 of [32.] (rotation around z-axis) with the 0° aligned with the x-axis.

To define the relevant set of variables ($H_s, T_p, \theta_{wave}, U, \theta_{wind}, TI$), the ANEMOC (Digital Atlas of Ocean and Coastal Sea States [29.]) database was used. This database gathers 30 years of sea state and wind simulation conditions obtained along the French coasts (but does not provide information for the TI). Hence, we first defined a domain Ω_{5D}, which is a subdomain of the 5D hypercube defined by the extreme values of each variable, such that 99% of the ANEMOC data are contained in Ω_{5D}.

The domain Ω is defined as the set of variables ($H_s, T_p, \theta_{wave}, U, \theta_{wind}, TI$) such that:

- ($H_s, T_p, \theta_{wave}, U, \theta_{wind}$)$\in \Omega_{5D}$ and $U \in [3m/s, 25m/s]$ to account for the cut-in and the cut-out of the wind turbine
- $ql_{TI|U} < TI < qu_{TI|U}$ where $ql_{TI|U}$ and $qu_{TI|U}$ are respectively the 1% and 99% of the $TI|U$ distribution. The variable σ_u denotes the standard deviation of the wind speed at hub height such that $TI|U = \frac{\sigma_u|U}{U}$. Following the recommendations of [30.] for a turbine IEC-Class IB, a lognormal

distribution for $\sigma_u|U$ whose expectation depends on U was used. The quantiles of $TI|U$ can then be computed.

The method described in section 5.2.1.1 is used to obtain a DoE of 700 points that covers properly the domain Ω.

5.4.2.2. Figures of the resulting DoE

After 3 million iterations, the 2D and 3D projection plots of the resulting DoE are displayed in the following figures:
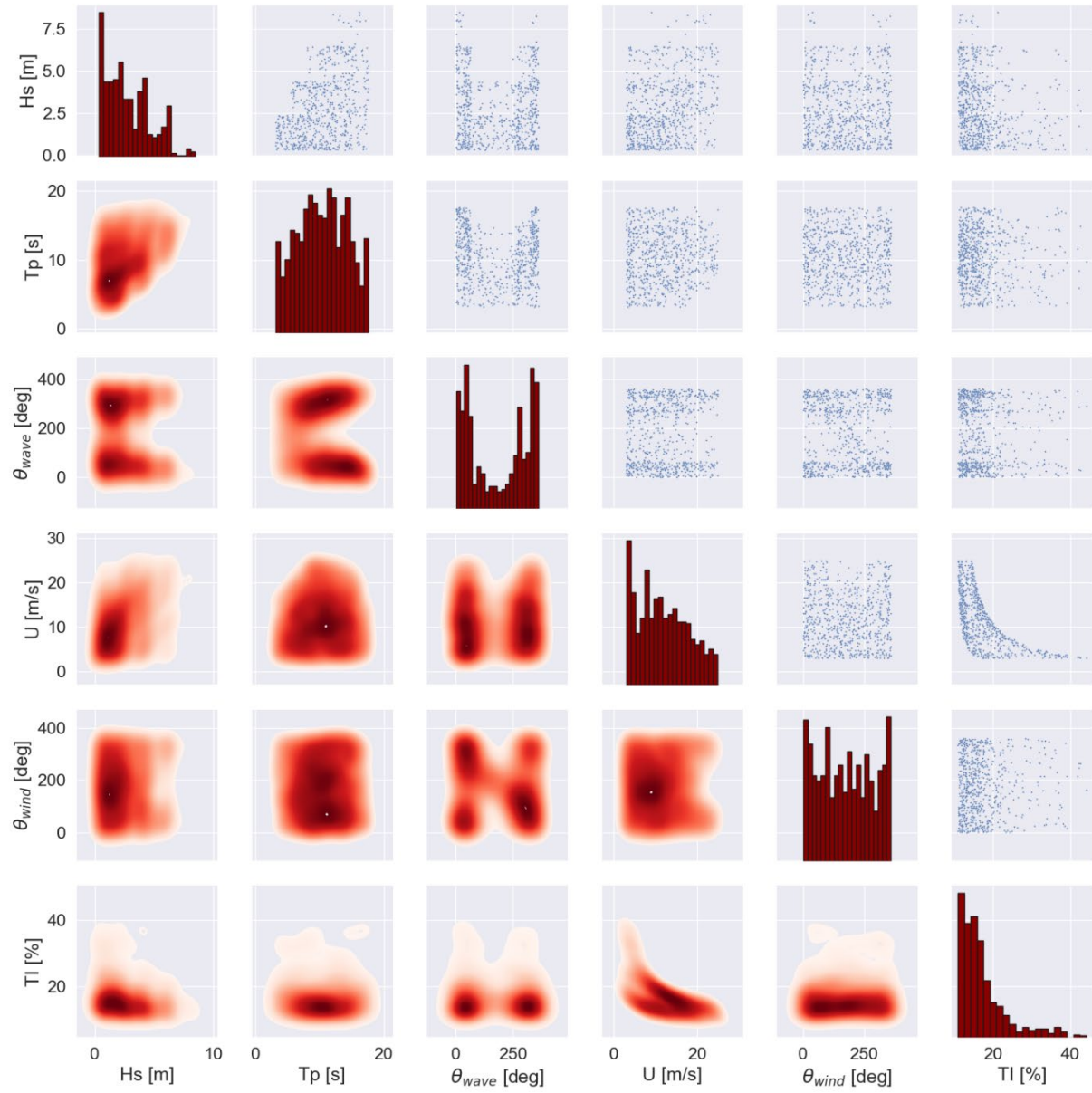
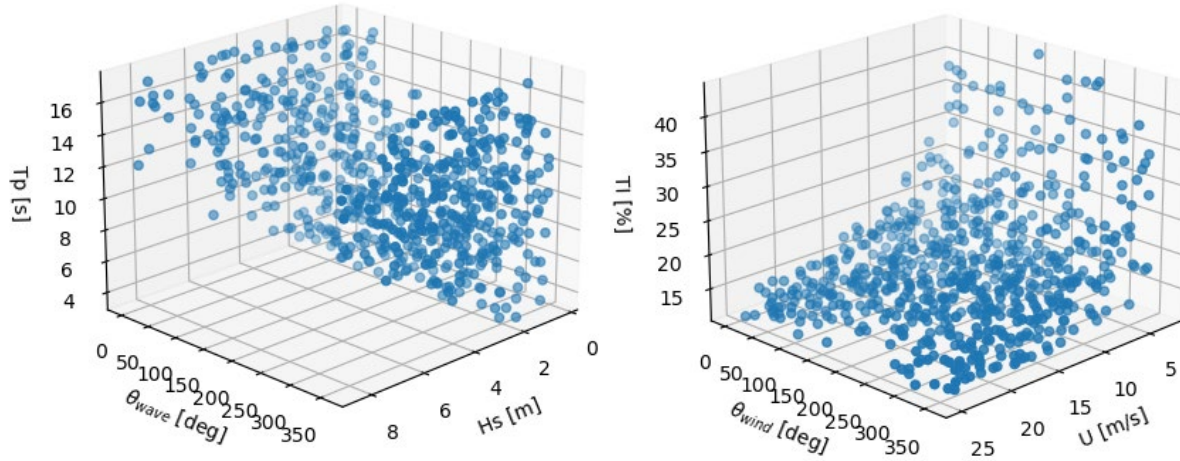*Figure 81. scatter matrix of the DoE for the BEM simulations*

Figure 82: 3D projections of the DoE for the BEM simulations for South Brittany

In Figure 81, the 2D projections of the DoE points are displayed in the upper diagonal subplots and the level sets of the corresponding distributions are in the lower diagonal subplots. The diagonal plots indicate the histogram of the points of the DoE for each dimension. Note that the goal of the algorithm used to obtain these points is not to reproduce the distribution of the environmental parameters but to cover properly the domain Ω.

Figure 82 shows the projections of the points of the DoE in the space of the wave parameters (left plot) and in the space of the wind parameters (right plot). These plots enable us to observe that the DoE points are well spread.

5.4.3. Overview of BEM results

According to the DoE, 700 DLW BEM simulations were performed. Figure 83 illustrates the results in terms of electrical power production. The left plot shows the time-averaged power against TI and U, while the right one shows the time averaged power against Hs and U. This representation makes it possible to identify the borders of the domain of interest Ω (see Figure 81). It is especially the case for (U, TI) resulting from the most frequent wind flow conditions, where high TIs (more than 30 %) are observed only for wind speeds lower than 5m/s. The expected power curve can be identified, with a nominal power of 15MW reached at a wind speed of around 11 m/s.
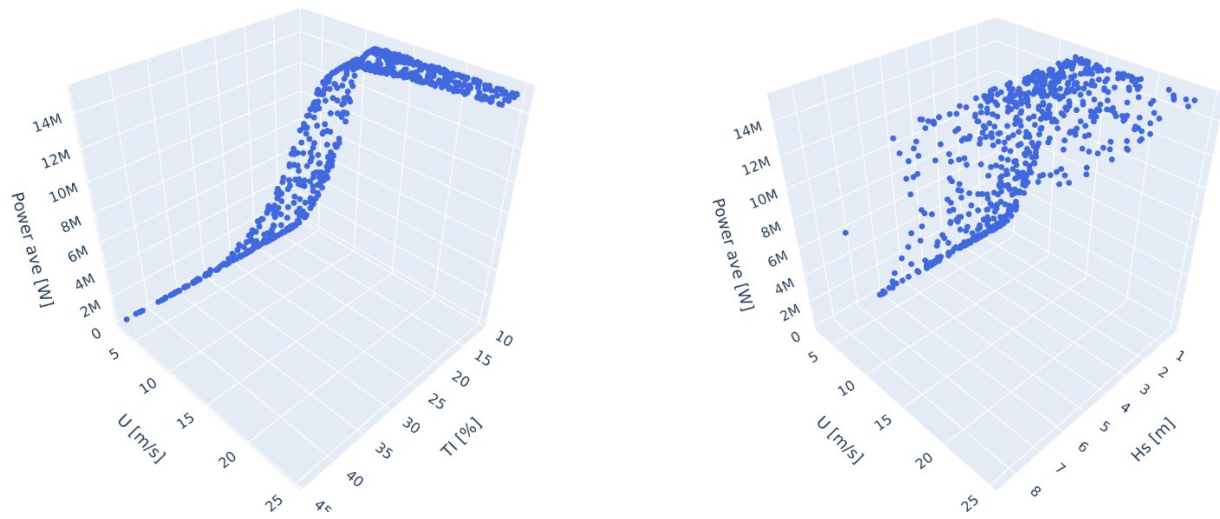
Figure 83. DLW BEM results for mean power for South Brittany floating case.

Figure 84. DLW BEM results for mean thrust (left) and mean torque (right) for South Brittany floating case

The 3D plots of mean thrust or mean torque against (U, TI) displayed in Figure 84 present the expected curves for these variables. On the thrust (left) a local maximum can be observed at rated conditions while the mean Torque (right) at these conditions and above them is constant.
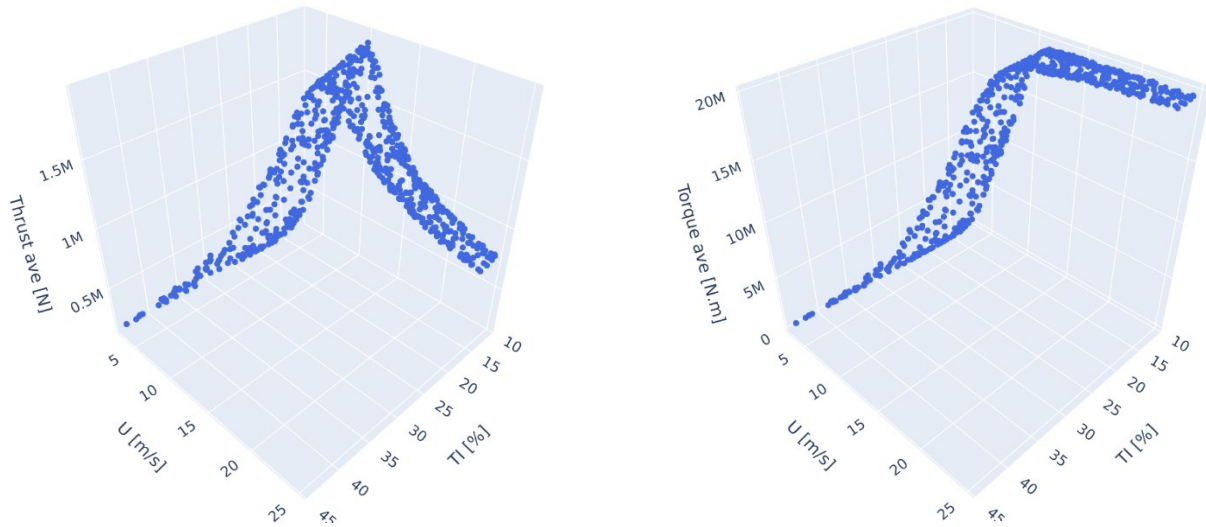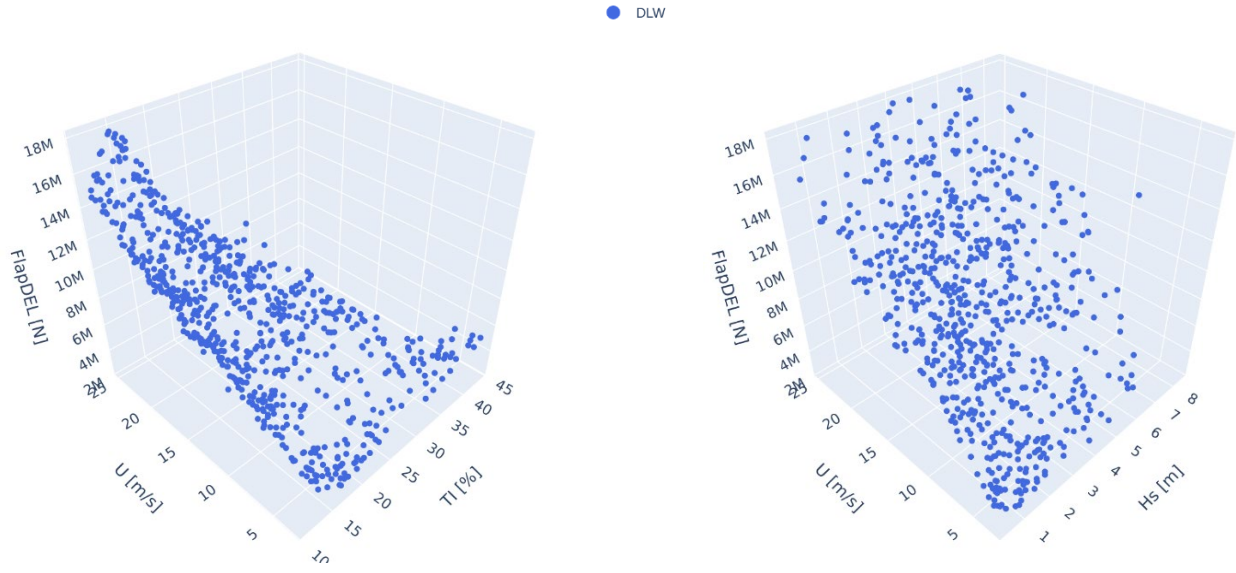
Figure 85: DLW BEM results for flapwise for South Brittany floating case

Figure 85 shows the BEM's results for the flapwise DEL against (U, TI) and against (U, Hs). It appears that the DEL increases with respect to TI and U and that the variations of this output are mainly due to the variations of U and TI. The floater motion does not change the main tendency of flapwise DEL with (U, TI) that was obtained and explained for the Teesside use case (see section 5.3.3).

5.4.4. Uncertainty evaluation

5.4.4.1. Validation of Gaussian process models

We used the method described in section 5.2.1.2.1 to obtain an initial DoE of 20 points for the Vortex simulations that covers properly the domain Ω defined in section 5.4.2.1. Then two iterations have been run where new points have been selected based on the LHS method described in section 5.2.1.2.2, where the 10 clusters with the highest predictive uncertainty from the GP based on the delFlap and the Power response are used as new scenario candidates. Once 60 scenarios are run, the goodness of fit of the GPs has been evaluated in the same manner as described in section 5.3.4.1. The RMSE and r2-score of the four GPs fitted to the BEM results and the Vortex results are presented in Table 21, while the qq-plot, the distribution of residuals, and the observed vs. predicted estimates of the CV is plotted in Figure 86. The results of the South Brittany simulations have a slightly higher RMSE and lower r2-score compared to the GPs fitted to the Teesside simulations. This is expected since, for Teesside, a DoE of 300 points is used for the BEM simulations (30 points for the Vortex simulations) in a 3D input space, while a DoE of 700 points is used for the BEM simulations for South Brittany (60 points for the Vortex simulations) in a 6D input space. Therefore, the latter input space is much more sparsely explored. Note however that the power is still accurately predicted.

Table 21 Regression metrics for the accuracy of fit – South Britany

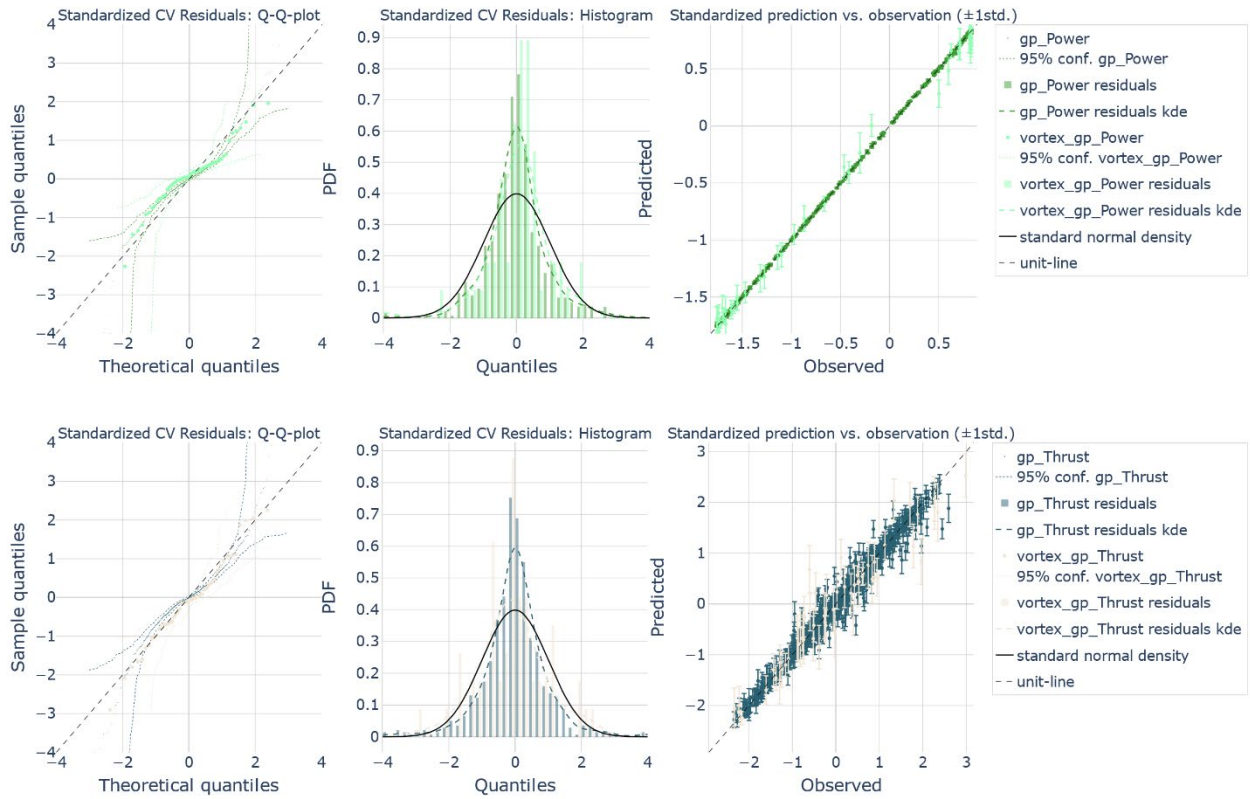|	delFlap BEM / Vortex	delEdge BEM / Vortex	Power BEM / Vortex	Thrust BEM / Vortex
RMSE	0.175 / 0.194	0.133 / 0.302	0.007 / 0.052	0.168 / 0.383
r2-score	0.969 / 0.978	0.982 / 0.917	0.9999 / 0.998	0.972 / 0.904
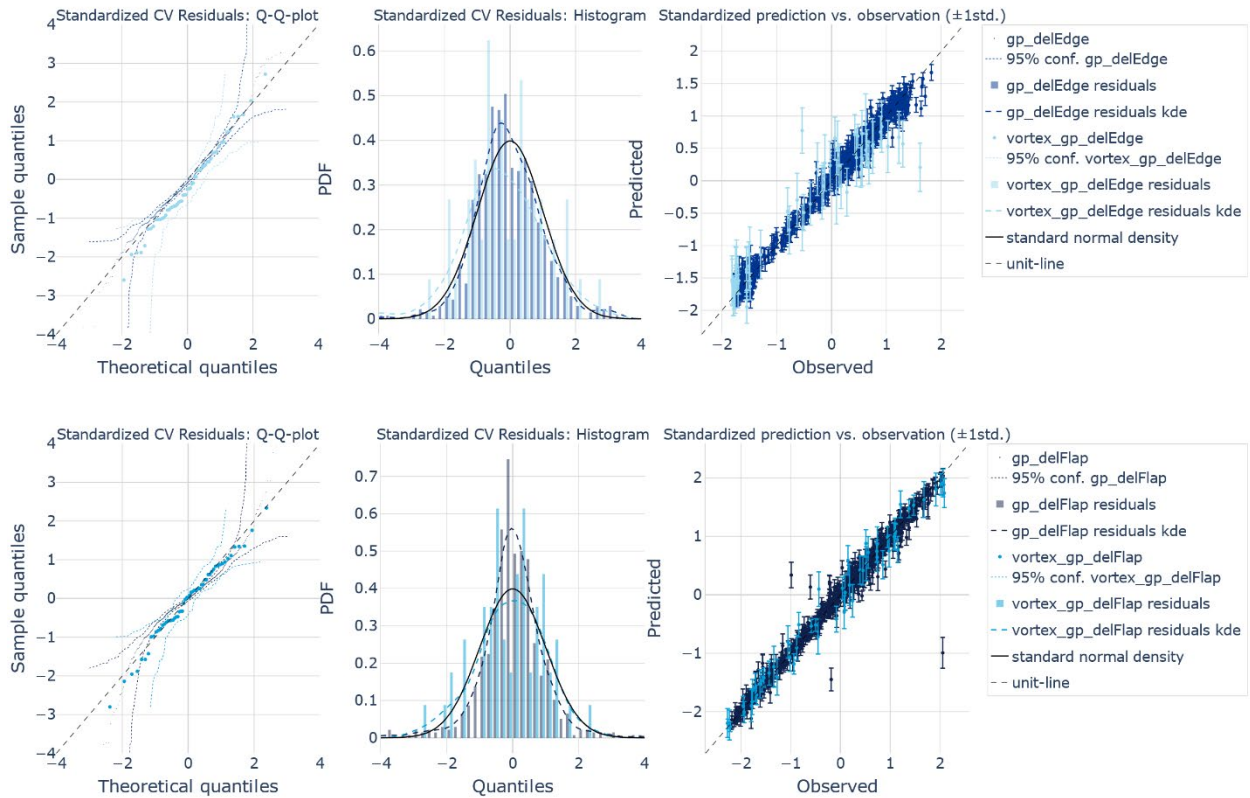
Figure 86 For each of the standardized quantities of interest: (left): plot of the Theoretical vs. Sample quantiles of the CV residuals, (middle): corresponding distribution of CV residuals, (right): CV prediction vs true observation including 1 standard deviation. From top to bottom the plots represent the distribution of Edge DEL, Flap DEL, Power, and Thrust.

5.4.4.2. Uncertainty evaluation

Figure 87 shows one projection of the predictions of the LHS (dots) for each of the selected quantities of interest (left) as well as the standard deviation of the GP predictions (middle). On the right, the relative difference between the GPs based on the Vortex simulation and those based on the BEM simulations are plotted. The large circles indicate the BEM simulations, while the magenta circles indicate the location (and response) of the Vortex simulations.

A larger variation in discrepancies between the Vortex and BEM GPs for the South Brittany case compared to that of Teesside can be seen (see metrics in section 5.5). This general result is expected as the South Brittany case has a 6D input space compared to the 3D input space of Teesside, and thus the relevant input space Ω is much less explored for the South Brittany case compared to that of Teesside.
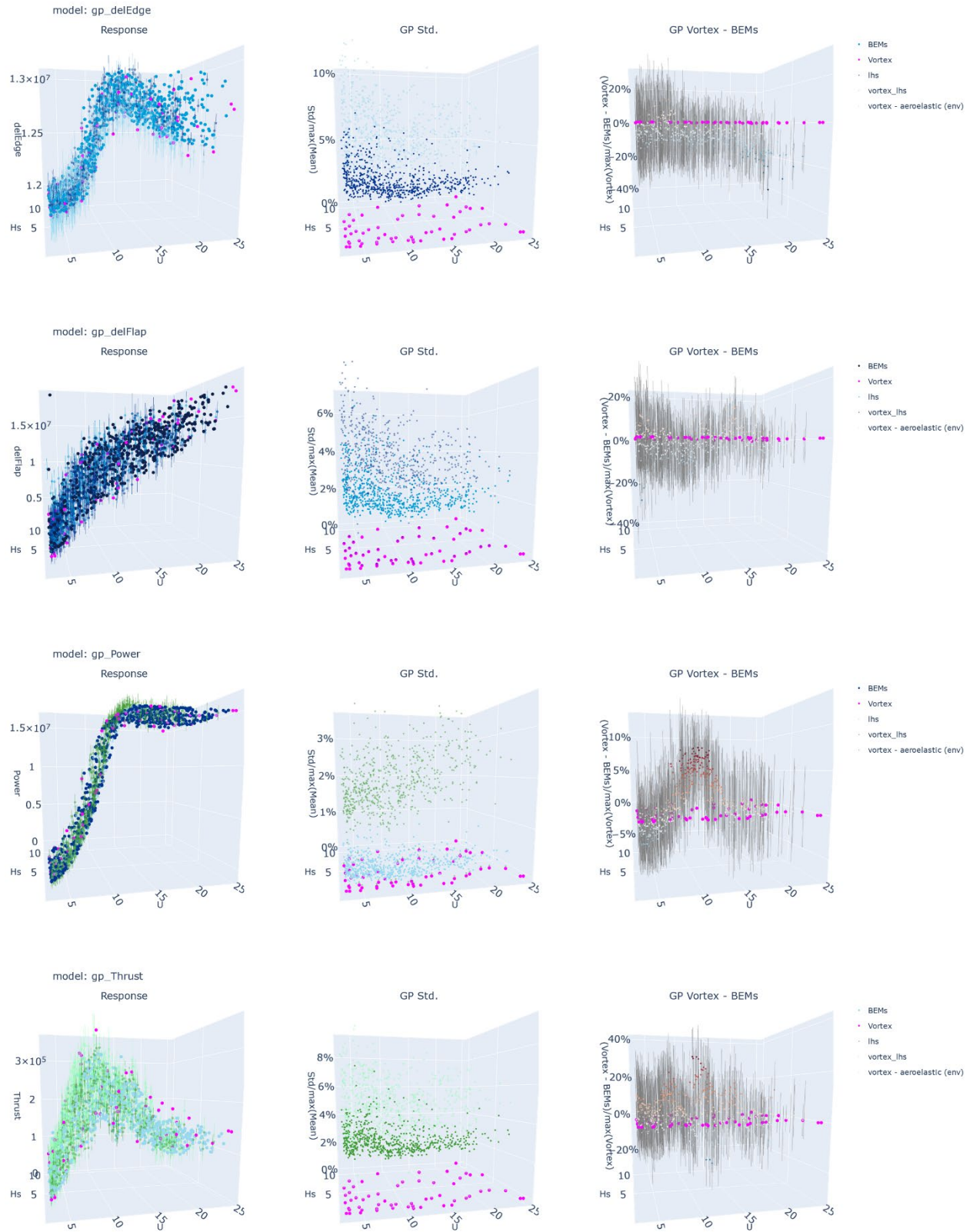
Figure 87 Prediction and model discrepancy for each of the quantities of interest plotted against windspeed U and significant wave height H_s: (left): plot of the BEMs and Vortex simulated response (circles) and the GP prediction for the LHS (dots) – samples outside the defined environmental contour is plotted in grey, (middle): relative GP std – color scale from white to dark blue corresponds to the GP std based on the BEMs while Reds corresponds to the GP std based on the Vortex, (right): relative differences between Vortex and BEM GP prediction for the LHS.

5.4.4.3. Exploiting the metamodels

5.4.4.3.1 BEM vs Vortex
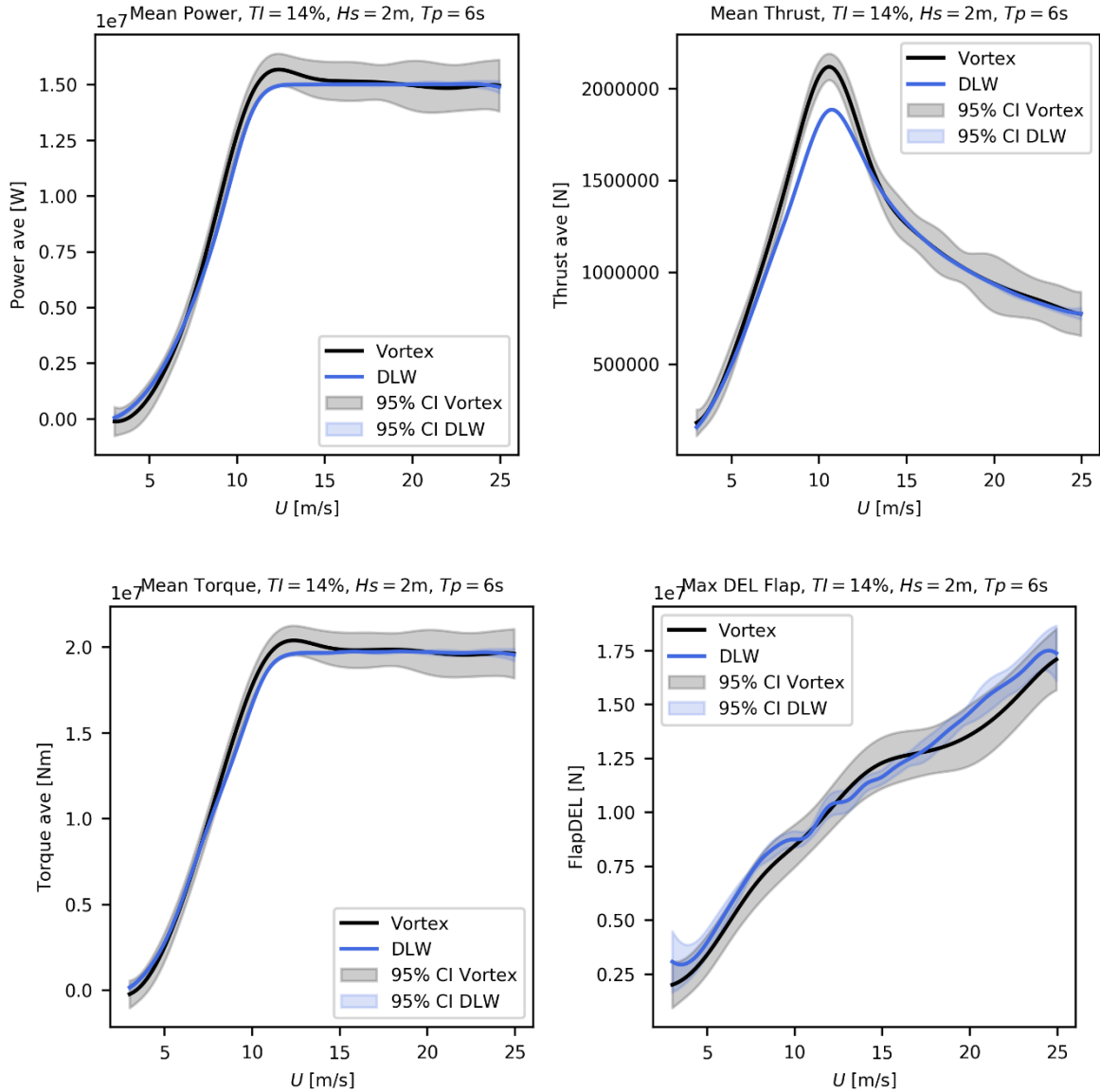
Figure 88: Power, Thrust, Torque, and DEL flap curves estimated with the metamodels calibrated from BEM simulations and Vortex simulations for a floating wind turbine for a $TI = 14\%$, $Hs = 2m$, $Tp = 6s$, $\theta_{wind} = 195°$, $\theta_{waves} = 165°$.

117

As done in 5.3.4.3 for the fixed wind turbine, it is possible to estimate, for the floating wind turbine, some continuous curves from the metamodels calibrated with the BEM results (only from DLW here) and vortex (also from DLW). The power, thrust, torque, and flapwise DEL curves for a $TI = 14\%$, $Hs = 2m$, $Tp = 6s$, $\theta_{wind} = 195°$, and $\theta_{wave} = 165°$ are provided in Figure 88. This specific set of environmental conditions corresponds to the one with a maximal probability of occurrence. The 95% CI is much wider for vortex results as for the fixed case, as the data set is sparse considering the important number of environmental conditions. If a good agreement can be observed between the two methodologies (BEM and Vortex), more discrepancies are noticed. Especially for the thrust at rated conditions, where the thrust obtained with the Vortex is higher than for the BEM. . The power and the torque show noticeable deviations for near cut-in and near-rated wind speed values, but the 95% CI contours overlap BEM results. Simarly, the flapwise DEL of BEM seems higher than that of Vortex for low and high U but the Vortex uncertainty encompasses the BEM CI. As seen during Teesside study, the confidence interval becomes wider when the metamodel tries to predict beyond the border of the DoE (see Figure 81 for the definition of the domain of interest Ω).
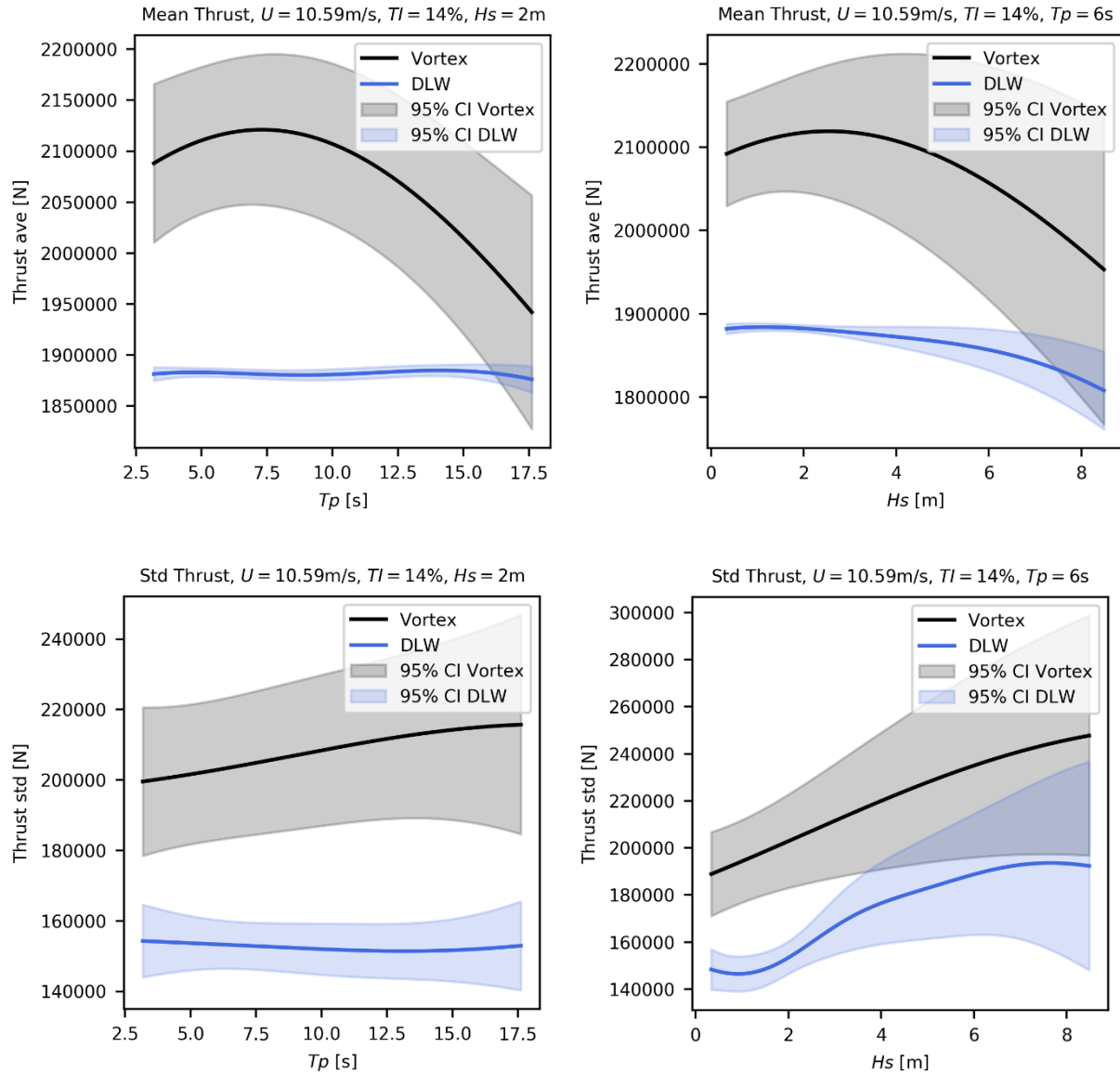
Figure 89: Time averaged thrust (top) and Std thrust (bottom) curves estimated with the metamodels calibrated from BEM simulations and Vortex simulations for a floating wind turbine for U=10,59m/s, TI=14% θ_{wind}=195°, θ_{waves}=165°, Hs=2m (left) and Tp=6s (right)

To analyse the effect of the waves on the wind turbine, the averaged and standard deviation of the thrust for different waves periods (Tp) and waves heights (Hs) values have been estimated with the metamodels at rated conditions and plotted in Figure 89. An underestimation of BEM is observable in each plot for the averaged thrust (as mentioned in the previous paragraph) or its standard deviation. But it is hard to conclude about the tendencies related to waves parameters, as the uncertainties of the metamodels themselves are important (95% CI). It seems that the BEM is less sensitive to wave conditions, showing an almost flat curve for the averaged thrust and underestimating the fluctuations related to the sea state.

As for Teesside, but emphasized for this large OWT, a large part of these differences may come from the use of the same controller setting, tuned for the BEM simulations, in the Vortex simulations. This setting

is non optimal for the Vortex and thus can explain part of the bump in the power and the higher thrust at rated conditions. The results of this study motivate a future work with another controller setting tuned with Vortex simulations.

In addition, a more complete DoE of Vortex simulations should help to reduce the metamodel uncertainty and clarify the comparison.

5.5. Synthesis of aerodynamic uncertainty design simulations using BEM

This section summarizes the results of the uncertainty study between BEM and Vortex simulations for the fixed and the floating wind turbine cases. Some simulation outputs have been considered to quantify the discrepancies between these two approaches namely the fatigues at blade root (flapwise and edgewise directions), the electrical power, and the aerodynamic thrust. For each of these outputs, a metamodel has been calibrated using a dedicated GP from the same DoE. Some metrics of the relative discrepancy between the BEM and Vortex GPs (metamodels) were then calculated.

Even though this analysis was carried out for both wind turbines, it is worth mentioning that both cases are very different. For the Teesside fixed wind turbine, the influence of 3 environmental parameters on the wind turbine was studied (wind speed, turbulent intensity, and yaw misalignment), and for the South Brittany floating wind turbine, six environmental variables were considered (wind speed, turbulent intensity, wind direction, wave height, wave period, and wave direction). Besides, the methodology in both cases is not the same. For Teesside, 3 BEMs codes were investigated, whereas for South Brittany only one was used. All this makes it difficult to provide a general conclusion about the uncertainty trends for aerodynamic models on fixed and floating wind turbines. However, some key indicators for the selected outputs of each case are presented below.

For Teesside, Table 22 summarizes the minimum, maximum, mean, and standard deviation of the relative discrepancy between BEM and Vortex across 1166 samples of a filtered LHS for the four selected outputs. The mean of the relative discrepancy for the *delFlap* and *delEdge* is 0.2%, while the standard deviations of these discrepancies are 3.0% and 2.4%. For the Power and Thrust, the mean relative discrepancy is 2.0.% and 2.3%, respectively, with a standard deviation of 3.3% and 4.2%.

Table 22 Relative difference of predicted responses by the GPs based on Vortex and BEMs simulations for Teesside (Vortex-BEM).

	delFlap	delEdge	Power	Thrust
min()	-9.8%	-15.2%	-8.3%	-12.6%
max()	13.4%	9.7%	14.6%	13.9%
mean()	0.2%	0.2%	2.0%	2.3%
std()	3.0%	2.4%	3.3%	4.2%

Similarly, Table 23 lists the minimum, maximum, and mean relative discrepancy between the BEM and Vortex GPs for the South Brittany case. In this case, the mean of the relative discrepancy for the *delFlap* and *delEdge* is -1.8% and -5.2% respectively, while the standard deviations of these discrepancies are 4.2% and 4.6%. For the Power and Thrust, the mean relative discrepancy is 1.3% and 4.4%, with a standard deviation of 2.4% and 5.9%, respectively.

Table 23 Relative difference of predicted responses by the GPs based on Vortex and BEMs simulations for South Brittany (Vortex-BEM)

	delFlap	delEdge	Power	Thrust
min()	-34.0%	-33.5%	-3.3%	-18.6%
max()	9.3%	9.2%	7.2.%	27.7%
mean()	-1.8%	-5.2%	1.3%	4.4%
std()	4.2%	4.6%	2.4%	5.9%

As can be seen, when comparing these tables, there is a larger discrepancy between the Vortex and BEM GPs for the South Brittany case compared to that of Teesside. This is expected since the South Brittany case has a 6D input space compared to the 3D input space of Teesside, and thus the relevant input space Ω is much less explored for the South Brittany case compared to that of Teesside.

It is important to note that these statistics are only indicating how well the GPs based on the Vortex and the BEM simulations match across the entire relevant input space. Depending on the intended use, these overall numbers, as well as the GP models, can be used to establish reasonable conservative assumptions e.g. for structural reliability analysis. For detailed assessments, the full GPs should be used to quantify the discrepancy for each relevant scenario.

As already explained, the controller setting has an influence on the results of this study. Consequently, the uncertainties quantities should be seen as a first upper-bound estimate of the aerodynamic "engineering" model uncertainty. They could be improved, and maybe reduced, by comparing in a future work the BEM and the Vortex simulations with another controller tuned with Vortex simulations.

References of Section 5

[1.] Glauert, H. (1935). Airplane propellers. In Aerodynamic theory (pp. 169-360). Springer, Berlin, Heidelberg.
[2.] Sebastian, T., & Lackner, M. A. (2013). Characterization of the unsteady aerodynamics of offshore floating wind turbines. Wind Energy, 16(3), 339-352.
[3.] Allen, C., Viselli, A., Dagher, H., Groupee, A., Gaertner, E., Abbas, N., Hall, M., Barter, G. "Definition of the UMaine VolturnUS-S Reference Platform Developed for the IEA Wind 15-Megawatt Offshore Reference Wind Turbine," Technical Report, NREL/TP-5000-76773, July 2020.
[4.] Burton, T., Jenkins, N., Sharpe, D., & Bossanyi, E. (2011). Wind energy handbook. John Wiley & Sons.
[5.] Manwell, J. F., McGowan, J. G., & Rogers, A. L. (2010). Wind energy explained: theory, design and application. John Wiley & Sons.
[6.] Øye, S. (1996). FLEX4. Simulation of wind turbine dynamics.
[7.] Jonkman, J. M., Hayman, G. J., Jonkman, B. J., Damiani, R. R., & Murray, R. E. (2015). AeroDyn v15 user's guide and theory manual. NREL Draft Report.
[8.] Bossanyi, E. A., & Quarton, D. (2003). GH bladed. Garrad Hassan.
[9.] Shaler, K., Anderson, B., Martinez-Tossas, L. A., Branlard, E., & Johnson, N. (2022). Comparison of Free Vortex Wake and BEM Structural Results Against Large Eddy Simulations Results for Highly Flexible Turbines Under Challenging Inflow Conditions. Wind Energy Science Discussions, 1-22.
[10.] Madsen, H. A., Larsen, T. J., Pirrung, G. R., Li, A., & Zahle, F. (2020). Implementation of the blade element momentum model on a polar grid and its aeroelastic load impact. Wind Energy Science, 5(1), 1-27.

[11.] Cottet, G. H., & Koumoutsakos, P. D. (2000). Vortex methods: theory and practice (Vol. 8). Cambridge: Cambridge university press.

[12.] Schepers, J. G., Lutz, T., Boorsma, K., Gomez-Iradi, S., Herraez, I., Oggiano, L., ... & Weihing, P. (2018). Final report of iea wind task 29 mexnext (phase 3).

[13.] Auffray, Y., Barbillon, P., & Marin, J. M. (2012). Maximin design on non hypercube domains and kernel interpolation. Statistics and Computing, 22(3), 703-712.

[14.] McKay, M. D., Beckman, R. J., & Conover, W. J. (2000). A comparison of three methods for selecting values of input variables in the analysis of output from a computer code. Technometrics, 42(1), 55-61.

[15.] Lloyd, S. (1982). Least squares quantization in PCM. IEEE transactions on information theory, 28(2), 129-137.

[16.] Williams, C. K., & Rasmussen, C. E. (2006). Gaussian processes for machine learning (Vol. 2, No. 3, p. 4). Cambridge, MA: MIT press.

[17.] Cohn, D. A. (1996). Neural network exploration using optimal experiment design. Neural networks, 9(6), 1071-1083.

[18.] Ranjan, P., Bingham, D., & Michailidis, G. (2008). Sequential experiment design for contour estimation from complex computer codes. Technometrics, 50(4), 527-541.

[19.] Hipersim - PyPI project: https://pypi.org/project/hipersim/

[20.] Hansen, M. (2015). Aerodynamics of wind turbines. Routledge.

[21.] Øye, S. (1991, January). Dynamic stall simulated as time lag of separation. In Proceedings of the 4th IEA Symposium on the Aerodynamics of Wind Turbines (Vol. 27, p. 28). Rome, Italy.

[22.] Leishman, J.G, and Beddoes, T.S. (1986). A generalized model for airfoils unsteady aerodynamic behavior and dynamic stall using the inidical method. In Proceedings of the 42nd Annual forum of the American Helicoper Society.

[23.] Glauert, H. (1926). A general theory of the autogyro. HM Stationery Office.

[24.] Prandtl, L. (1919). Appendix to Betz's article: Schraubenpropeller mit geringstem energieverlust-mit einem zusatz von L. Prandtl. Göttinger Klassiker der Strömungsmechanik Bd, 3, 89-92.

[25.] Pitt D.M. & Petters D.A. (1981), Theoritical prediction of dynamic inflow derivatives. Vertica 5, 21-34

[26.] Moriarty, P. J., & Hansen, A. C. (2005). AeroDyn theory manual (No. NREL/TP-500-36881). National Renewable Energy Lab., Golden, CO (US).

[27.] Leishman, G. J. (2006). Principles of helicopter aerodynamics with CD extra. Cambridge university press.

[28.] Snel, H., Houwink, R., & Bosschers, J. (1994). Sectional prediction of lift coefficients on rotating wind turbine blades in stall.

[29.] ANEMOC. (Digital Atlas of Ocean And Coastal Sea States). http://anemoc.cetmef.developpement-durable.gouv.fr/

[30.] Part, W. T. (2005). 1; Design Requirements; IEC 61400-1. International Electrotechnical Committee: Geneva, Switzerland.

[31.] Kelly, M., Vanem, E. (2002). Environmental joint probability distributions and uncertainties. Deliverable report D2.3 of HIPERWIND H2020 project, Grant agreement No. 101006689.

[32.] Capaldo M., Guiton, M., Huwart, G., Julan, E., Kramisirov Dimitrov, N., Kim, T., Lovera, A., & Peyrard, C. (2021). Design brief of HIPERWIND offshore wind turbine cases: bottom fixed 10MW and floating 15MW. https://www.hiperwind.eu/publications.

[33.] Python package GPyTorch documentation: https://docs.gpytorch.ai/en/stable/

[34.] Python package PyTorch documentation: https://pytorch.org/docs/stable/index.html

6. Conclusions

On the hydrodynamic side, both bottom fixed and floating foundations have been studied, on specific points:

- Bottom fixed : the main objective was to estimate a level of uncertainty of the hydrodynamic DEL, which is a significant contributor to the fatigue of monopiles. As base case, the Teesside metocean conditions have been used and the full *Hs-Tp* scatter diagram has been covered. Two monopiles were considered, the Teesside original 2.3MW and a larger monopile supporting the DTU 10 MW turbine. From this starting point, several hydrodynamic models have been investigated: an "engineering" model based on the strip theory and the MacCamy-Fuchs correction ; a linear Potential Flow model providing a better description of the monopile geometry and a second-order Potential Flow model able to capture high-frequency loads in a consistent way. The level of uncertainties of the engineering model has been characterized, leading to the identification of over conservatism in some conditions, usually for short waves or when large TP cross the free surface. However, for some conditions the engineering model is not conservative enough, in particular for long and high waves or when the TP is fully submerged. DEL maps have been extracted from the study, giving the DEL uncertainty for any [Hs;Tp] couple and could be used for the WP4 analysis, more general values, easier to implement, have also been extracted from the study to feed WP4.

- Floating : the focus was made on the drag coefficients estimation, for the specific case of UMaine the floater used within HIPERWIND. A significant work has been performed using 2 CFD solvers, namely the open source OpenFOAM® and the EDF R&D neptune_cfd code. These solvers have first been compared to experimental data on simple shapes : submerged 2D rectangular and surface piercing 3D column. This preliminary work allowed for an estimation of the dispersion one can expect from CFD and experimental models. Then the full UMaine floater geometry was studied with the objective to extract drag coefficients on several area of the structure, for various Keulegan-Carpenter numbers. Here, several sources of uncertainties were characterized:
  - o fluid-structure interaction: fixed floater in waves and moving floater in still water have been investigated
  - o drag coefficient extraction : several method have been tested, in particular due to phase shift observed between the kinematics and the loads when analysing the time series.
  - o Solver : even if the results of the 2 codes were close, the drag coefficients extracted from the simulations were different

  The main outputs of the floating section are range of drag coefficient to be used by WP4, depending on the area considered on the floater and the sea conditions (through KC number).

On the aerodynamic side, the present work conducted a comparison between BEM and Vortex models for two different offshore technologies: an existing 2.3 MW fixed wind turbine from Teesside EDF wind farm in UK, and a generic future generation 15MW floating one from the IEA15MW wind turbine on a modified version of the UMaine semi-submersible floater. Through multiple simulations of BEM models, using different ASHE tools (Diego, Hawc2, and DLW), the uncertainties against high fidelity Vortex models have been studied.

A substantial benchmark between the three tools has been performed on the first wind turbine, for different environmental variables, such as wind speed, turbulent intensity, and yaw misalignment. An overall good agreement can be seen, despite the different ways to parametrize the simulations (the aim was to use the software following its own best practices). Some slight deviations between the models have been observed, highlighting the dependence of BEM methods on the calibration of its correction models. To evaluate the uncertainty of ASHE software using BEM, simulations with higher fidelity Free Vortex Wake method have been conducted. Such simulations are much more expensive. To have enough data for the uncertainty evaluation, both the CPU cost of the simulation and the number of points have been optimized: the parallel computation over GPUs has been exploited and the number of vortex filaments has been reduced (shed merging and trail merging), while the DoE has been optimized iteratively using kriging approach.

In the end, it enables obtaining a metamodel of uncertainty for ASHE using BEM methods, according to the FVW method, for two different wind turbines. The established GPs and the resulting GP of the discrepancy between the Vortex and BEM simulations can be used in two different ways: either to select a conservative response with a specified confidence level for all relevant input scenarios, or to fully quantify the uncertainties between both approaches. In the latter case, close to the points where the Vortex simulations have been run the uncertainty in the difference between the BEM and Vortex is relatively small. This uncertainty will increase as one gets outside the input space explored, i.e. extrapolation. As a result, it is found that the uncertainties for the existing wind turbine are relatively reasonable, with about 2% on power production and aerodynamic thrust, and less than 1% on fatigue on average. However, for highly flexible floating IEA15MW, while the uncertainty of the power production remains stable (controller behavior), the mean uncertainties of the thrust and the fatigue rise up to 4.4% and 5.2% respectively. A large part of these differences can be explained by the setting of the controller based on BEM simulations. The abovementioned uncertainties should then be considered as first upper bounds of the aerodynamic "engineering" model uncertainty. These values could be reduced in a future work with another controller tuned with Vortex simulations. The remaining differences should then only result from the higher fidelity aerodynamic representation of the Vortex, including the aero-elastic coupling for the new generation of large OWT. It can also be noted that FVW models can be optimized to reduce the computational cost. They thus become operational for the industry, in complement to monitoring data fitting, to either improve the BEM corrections, or directly simulate the aerodynamic forces on the future OWTs.

Appendix A.   Wind generation using HiperSim

Teesside cases

Methodology

The wind input files were generated using HiperSim. According the 300 cases proposed in the DoE, 300 wind files were produced. This document provides and explains the generic HiperSim inputs to generate them (domain, time step, power law exponent, etc…). Then, for each case the values of wind speed at hub height (U_h) and Turbulence Intensity (**TI**) had been set according to the DoE.

Below are presented some of the specifications proposed.

Specifications proposed

Grid domain and length of the simulation

The proposed grid domain pursued take into account the recommendations for wind file generation described in [1.].

- **Ly** (length in **y**) = 140 m   # should be at least 110% of the rotor diameter
- **Lz** (length in **z**) = 140 m   # should be at least $zhub + d/2$

As the goal was to analyze the results of the last hour of the simulation, the time length of the wind file was 3900 s in order to consider 300 s for convergency:

- **Lt** = 3900 s

Resolution in time and space

To be coherent and able to have the same wind file resolution for BEM and vortex simulations, high resolution simulations were proposed.

- **dy** and **dz** = 5 m   # resolution in y and z, to have almost 10 elements per blade
- **dt** = 0.1 s   # resolution in time ($dx = U_h\ dt$)

Turbulence Intensity

The value in the mean wind direction (TI_u) was the one defined in each case of the 300 cases and the values in the transverse (TI_v) and vertical (TI_w) directions were related to TI_u by two factors defined for the Kaimal model [1.].

- $TI_v = 0.8 * TI_u$
- $TI_w = 0.5 * TI_u$

Mann Parameters

In order to have the same Mann parameters in all the simulations, the values used were:

- L = 29.4   # default value (Mann spectrum similar to the Kaimal spectrum)
- $Gamma$ = 3.9   # default value (Mann spectrum similar to the Kaimal spectrum)
- $Alphaepsilon$ = 0.1
- $SeedNo$ = 10
- $HighFreqComp$ = 0

Other parameters

These are other parameters necessary for the script, not detailed for confidentiality reasons.

- $zhub$ # hub height in meters
- yaw # the wind hadn't been yawed, the wind turbine had be.
- $alpha$ # power law exponent. Mean value obtained from the measurements.

South Brittany cases

Methodology

The wind input files were generated using HiperSim. According the seven hundred cases proposed in the DOE, 700 wind files were produced. This document provides and explains the generic HiperSim inputs to generate them (domain, time step, power law exponent, etc…). Then, for each case the values of wind speed at hub height (U_h) and Turbulence Intensity (TI) had been set according to the DOE.

Below are presented some of the specifications proposed.

Specifications proposed

Grid domain and length of the simulation

The proposed grid domain pursued take into account the recommendations for wind file generation described in [1.]

- Ly (length in y) = 300 m   # should be at least 110% of the rotor diameter, i.e. Ly > 266 m.
- Lz (length in z) = 300 m   # should be at least $zhub + d/2 = 150 + 118/2 = 209$

As the goal was to analyze the results of the last hour of the simulation, the time length of the wind file was 3900 s in order to consider 300 s for convergency:

- Lt = 3900 s

Resolution in time and space

To be coherent and able to have the same wind file resolution for BEM and Vortex simulations, high resolution simulations were proposed.

- dy and dz = 12 m   # resolution in y and z, in order to have almost 10 elements per blade

- dt = 0.1 s   # resolution in time ($dx = U_h\ dt$)

Turbulence Intensity

The value in the mean wind direction (TI_u) was the one defined in each case of the 300 cases and the values in the transverse (TI_v) and vertical (TI_w) directions were related to TI_u by two factors defined for the Kaimal model [1.].

- $TI_v\ = 0.8 * TI_u$
- $TI_w = 0.5 * TI_u$

Mann Parameters

In order to have the same Mann parameters in all the simulations, the values used were:

- L = 29.4   # default value (Mann spectrum similar to the Kaimal spectrum)
- $Gamma$ = 3.9   # default value (Mann spectrum similar to the Kaimal spectrum)
- $Alphaepsilon$ = 0.1
- $SeedNo$ = 10
- $HighFreqComp$ = 0

Other parameters

These are other parameters needed, not detailed for confidentiality reasons.

- $zhub$ # hub height in meters
- yaw # the wind is yawed in the ASHE simulations set up.
- $alpha$ # power law exponent.

References of Appendix A

[1.] Jonkman, B. J., & Buhl Jr, M. L. (2006). *TurbSim user's guide* (No. NREL/TP-500-39797). National Renewable Energy Lab.(NREL), Golden, CO (United States).

Appendix B -

Lorem ipsum dolor sit amet, consectetur adipiscing elit, sed do eiusmod tempor incididunt ut labore et dolore magna aliqua.

Appendix C –

Lorem ipsum dolor sit amet, consectetur adipiscing elit, sed do eiusmod tempor incididunt ut labore et dolore magna aliqua.